VILNIUS UNIVERSITY

CENTER FOR PHYSICAL SCIENCES AND TECHNOLOGY

INSTITUTE OF CHEMISTRY

Simas Šakirzanovas

NOVEL Sm$^{2+/3+}$ PHOSPHORS AS LUMINESCENCE CONVERTER FOR NEAR UV RADIATION

Doctoral Dissertation

Physical Sciences, Chemistry (03 P)

Vilnius, 2011

The dissertation was carried out in Vilnius University in the period of 2007-2010.

Scientific supervisor:

Prof. Habil. Dr. Aivaras Kareiva

(Vilnius University, Physical Sciences, Chemistry 03P)

Scientific consultant:

Prof. Dr. Thomas Jüstel

(Muenster University of Applied Sciences, Physical Sciences, Chemistry 03P)

CONTENTS

Chapter 1.

1.1. Introduction

Rare earth (RE) ions play an important role in modern optical technologies as the active constituents in many novel materials. There are an increasing number of applications for these RE-activated materials and much of today's cutting-edge optical technology and future innovations are expected to rely on their unique properties. The rare earth elements have had and still have a unique and important impact on our lives. The unfilled 4f electronic structure of the rare earth elements makes them to possess special properties in luminescence, magnetism and electronics, which could be used to develop many new materials for various applications such as phosphors, magnetic materials, hydrogen storage materials and catalysts [1].

The luminescence of rare earth ions has a large technological importance in a variety of materials like phosphor lamps, displays, lasers, and optical amplifiers. Usually, the best hosts for these lanthanide ions are inorganic materials like crystals and glasses, because those ions generally show high quantum yields in these hosts. There is a considerable research activity in the field of luminescent materials for lighting and displays to improve the chemical stability and to adopt the materials to the production technology. On the one hand ongoing miniaturization, lifetime improvement and spectral stability of light sources and on the other hand brightness and contrast improvement in imaging systems demand luminescent materials with very high stability that is invariable to operating conditions.

The significant part of the today's efficient lighting sources is based on indirect light emission, which can be organized by the excitation source. Luminescent materials in plasma display panels (PDPs) and field emission displays (FEDs) use the high energy side of UV spectrum, i.e. vacuum ultraviolet (VUV) and even low voltage electrons, respectively [2, 3]. Phosphors are excited by near UV or blue light, which are coated on light emitting diodes (LEDs) and to some extent in fluorescent lamps for special

applications. The major application of rare-earth-doped luminescent materials (i.e. phosphors) is for radiation conversion in order to get emission at distinct and different wavelengths in the electromagnetic spectrum. This feature have been widely used in color cathode ray tubes (CRT), tri-phosphor fluorescent lamps, X-ray intensifying screens and newly developed vacuum mercury-free lamps, as well as various types of displays such as plasma display panels, field emission displays and projection TVs [4]. In particular, the invention of high-efficiency blue-emitting InGaN-based LEDs makes realization of efficient, full-spectrum white-light LEDs for general illumination possible by using conversion phosphors [5]. Unfortunately, very few existing phosphor materials can efficiently convert the UV-blue emission from the LED into green, and in particular, red light. In addition, red-emitting phosphors that can be efficiently pumped by UV-blue LEDs are very scare. Consequently, as an explorative research, creating and designing novel luminescent materials by various ways is a major motivation.

The most common oxidation state of RE ions is usually a trivalent one. The 4f – 4f transitions of trivalent RE-doped materials brings out inherent optical properties. On the other hand, some RE ions such as Sm, Eu and Yb can be present in a divalent oxidation state as well. In contrast to the trivalent RE ions, the divalent RE ions in solids manifest unique characteristics. Firstly, the valence change can be induced by high-energy radiation, such as ultraviolet (UV), X-ray or γ-ray. Secondly, the 4f – 5d transition appears in the visible region for divalent RE ions, while for trivalent RE ions it lays in the ultraviolet region. The 4f – 5d transition is parity-allowed, and therefore, the probability is much higher than for parity-forbidden 4f – 4f transition. Furthermore, the energy levels of 5d orbitals are largely influenced by the ligand field compared with those of 4f orbitals. Such features of divalent RE ions give rise to the possibility of inducing novel and striking optical effects. A typical example of utilizing the change of the valence state of divalent RE ions is persistent spectral hole burning due to photoionization. This phenomenon occurs when a frequency-selected subset of optical absorption band is modified by the

photoionization removal of RE ions, as was first shown in CaF_2:Sm^{2+} [6] and subsequently in $BaClF$:Sm^{2+} [7]. In order to design materials with suitable quality for room-temperature persistent spectral hole burning many studies have been extensively performed for Sm^{2+}-doped mixed crystals and glasses [8-14].

The motivation to perform such investigation was limited available data in scientific literature on $Sm^{2+/3+}$ luminescence properties. The discussion is divided into chapters describing the main information gained from separate investigation of the different inorganic materials doped with samarium. Thus, these aspects provide the novelty and originality for the doctoral dissertation.

The main aim of this work was to synthesize and investigate new $Sm^{2+/3+}$ phosphors. The additional aim was better understand the nature and properties of the inorganic crystalline materials doped with $Sm^{2+/3+}$ ions searching of suitable inorganic hosts for successful divalent samarium incorporation as well. For this reason, there were formulated tasks as follows:

1. Synthesis and investigation of photoluminescence properties of Sm^{2+} substituted SrB_4O_7.

2. Synthesis and investigation of photoluminescence properties of Sm^{3+} substituted $LnMgB_5O_{10}$ (Ln = La, Gd).

3. Synthesis and investigation of photoluminescence properties of Sm^{3+} substituted $SrAl_{12}O_{19}$ and $LaMgAl_{11}O_{19}$.

4. Synthesis and investigation of photoluminescence properties of $Sm^{2+}/^{3+}$ substituted $Sr_4Al_{14}O_{25}$.

Statements for defense:

1) Samarium substituted $Sr_{1-x}Sm_xB_4O_7$ and different aluminate matrixes ($SrAl_{12}O_{19}$, $LaMgAl_{11}O_{19}$ and $Sr_4Al_{14}O_{25}$) could be synthesized using advanced preparation routes. The results obtained indicate that the synthesis route and synthesis temperature make significant influence on the stability of crystalline phases and luminescent properties.

2) Samarium substituted $Sr_{1-x}Sm_xB_4O_7$ samples could be prepared by solid-state synthesis route. The preparation gives Sm^{3+} reduction to divalent state even after annealing in air at high temperature. The d–f transitions of Sm^{2+} in SrB_4O_7 appear at slightly higher than room temperature due to the low enough energy position of the $4f^55d^1$ level and the small energy difference between $4f^55d^1$ and $^5D_0$ levels. The study on the temperature dependence of samarium luminescence in strontium tetraborate shows that the variation of Sm^{2+} fluorescence is most probably governed by the lowest lying $4f^55d^1$ states. Moreover, the shape of emission spectra pointed out that Sm^{2+} occupies the C_{2v} or lower symmetry site in SrB_4O_7.

3) Orange-red emitting $La_{1-x}Sm_xMgB_5O_{10}$ and $Gd_{1-x}Sm_xMgB_5O_{10}$ photoluminescent materials could be synthesized by a solid state reaction method at 1020 °C for 8 h. Four emission bands corresponding to the $^4G_{5/2} \rightarrow {}^6H_{5/2}$, $^6H_{7/2}$, $^6H_{9/2}$ and $^6H_{11/2}$ transitions peaking at 560, 600, 650 and 710 nm, respectively, upon excitation at $^6H_{5/2} \rightarrow {}^4L_{13/2} + {}^6P_{3/2} + {}^4F_{7/2}$ (402 nm) have been observed. The decay lifetimes for Sm^{3+} emission upon direct excitation of Gd^{3+} is around 0.1 ms longer, confirming the energy transfer phenomena.

4) It was found that the best suitable synthesis technique to get phase pure $SrAl_{12}O_{19}$ is combustion with EDTA as fuel. The same structure $LaMgAl_{11}O_{19}$ pure phase can be synthesized via same method regardless the fuel used. No obvious conclusion about Sm^{3+} occupied site symmetry could be made due to insufficient clarity of the shape and intensity of observed transitions. Annealing under highly reducing conditions at high temperature revealed that examined magnetoplumbite hosts are not suitable for samarium reduction to divalent state. The measured emission decay values fall into the range of 2.1 – 2.7 ms for $LaMgAl_{11}O_{19}:Sm^{3+}$ and 2.5 – 3.0 ms for $SrAl_{12}O_{19}:Sm^{3+}$.

5) Complete and partial samarium reduction was achieved under strong reducing atmosphere by solid-state and combustion synthesis of $Sr_{3.96}Sm_{0.04}Al_{14}O_{25}$. Dependence of different fluxing agents on the formation of various strontium aluminates was examined. Excitation with UV radiation resulted in sharp and well resolved emission lines of samarium ions. Distinct temperature behaviour for Sm^{2+} and Sm^{3+} were detected in the range of 100-500 K. Estimated emission thermal quenching values ($TQ_{1/2}$) for divalent samarium were approximately 270 K while for trivalent state around 660 K. Measured luminescence decay values of Sm^{2+} are substantially lower than for Sm^{3+}, ≈ 1.7 and ≈ 2.7 ms, respectively. The spectral feature of Sm^{2+} emission spectrum indicates that dopant occupies low symmetry site in $Sr_4Al_{14}O_{25}$ compound.

Chapter 2.

2.1. Fundamentals of Lanthanide Doped Inorganic Materials

It is well known that free atoms or ions generally exhibit discrete energy level scheme. However, of primary technological interest are not the optical properties of the free RE atoms but rather those of the RE ions embedded into a solid. It has been found that when introduced into a solid the electronic configuration of RE ion usually acquires the trivalent charge state $[Xe]4f^{n-1}$ (i.e., the two $6s^2$ electrons and one 4f electron is removed). This is because it takes relatively little energy to remove one electron from the 4f shell (the two 6s electrons are loosely bound anyway). For energies from IR up to the UV range, the transitions in trivalent RE ions only involve the energy levels of the 4f shell, i.e. the ground configuration of the ion [15]. As the 4f shell of RE ion is still shielded by the $5s^2 5p^6$ electrons, the free-ion energy levels are only weakly perturbed by the surrounding environment and the 4f intraconfigurational transitions retain their atomic-like characteristics, e.g. spectral sharpness (of the order of 10 cm^{-1} in good crystalline host) and long lifetime (of the order of 1 ms). From the scientific as well as the technological point of view one is mostly interested in the spectrally narrow highly efficient emission of the RE ions. Such narrow lines provide sensitive probes of weak perturbations. For example, the Stark splitting of the emission lines in a crystal field and the relative intensity of different transitions are indicators of the site symmetry of the emission center. Technologically the phosphors emitting spectrally narrow lines are favorable in e.g. display devices, where they can provide very pure primary colors (the red emission of Eu^{3+} at 620 nm being the most well known) [3].

This chapter will introduce the basic theoretical background for the experiments presented in this work. A generalized look on the field of rare-earth spectroscopy can be found in the book of Blasse [4]. Following chapter starts with an introduction to the energy level structure of lanthanide ions and describes the changes introduced when the ion is placed in a crystalline

environment. Later the role of lattice vibrations in the lanthanide spectra and the energy transfer processes occurring in the examined crystal systems is discussed. The special properties of the samarium ion will be presented in the Chapter 3.

2.2. Rare-Earth Elements

As defined by IUPAC, rare-earth elements or rare-earth metals are a collection of seventeen chemical elements in the periodic table, namely scandium, yttrium, and the lanthanoids. Fifteen elements La – Lu are lanthanoids and fourteen elements Ce – Lu, without lanthanum, are lanthanides (meaning the elements similar to lanthanum). The lanthanoid series comprise the fifteen elements with atomic numbers 57 through 71, from lanthanum to lutetium. Lanthanoids are strongly paramagnetic for all configurations from $4f^1$ to $4f^{13}$; hence, the compounds have been quite extensively applied in superconductors, magnetic refrigeration, permanent magnets, etc. Scandium and yttrium are considered rare-earths since they tend to occur in the same ore deposits as the lanthanoids and exhibit similar chemical properties. **Ln** abbreviation often is used as a general symbol for the lanthanide elements. The partially filled 4f-shell also gives rise to unique optical properties that provide the basis for the optical applications of lanthanides. Most importantly, the 4f electrons remain highly localized to the atom and the optical transitions within the 4f manifold maintain much of an atomic-like character even when the lanthanide ion is embedded into a solid, therefore exhibit intense narrow-band luminescence across much of the visible and near infra-red portions of the spectrum.

Neutral lanthanides (Ln) possess the electron configuration $4f^n5s^25p^66s^2$ where the number of 4f electrons **n** ranges from 2 for cerium to 14 for ytterbium. Lanthanides are most stable in the +3-oxidation state, leading to high coherent behavior and hence making them difficult to separate and purify. The preference for the trivalent oxidation state is due in part to the energy of the 4f electrons being below those of the 5d and 6s electrons (except in the

cases of La and Ce). When forming ions, electrons from the 6s and 5d orbitals are lost first, so that all Ln^{3+} ions have $[Xe]4f^n$ electronic configurations. This, coupled to the high enthalpies of hydration for trivalent lanthanides, results in the stability of the +3-oxidation state. In reducing conditions, europium, samarium and ytterbium can be stable in the divalent form; cerium has also been known to adopt a +4-oxidation state. This is in contrast to the actinide series where oxidation numbers up to +8 are known. The fact that the oxidation state in some cases tends to +2 can be understood by looking at the reduction potentials for the $Ln^{3+} + e^- \rightarrow Ln^{2+}$ process (*Figure 2.1*). It makes clear why Ln^{2+} ions are commonly seen only for a few lanthanides: the majority of the Ln^{3+} ions have reduction potentials of – 2.3 V or greater [16, 17]. It is clearly visible why only few suitable compounds for Sm^{2+} incorporation exist.
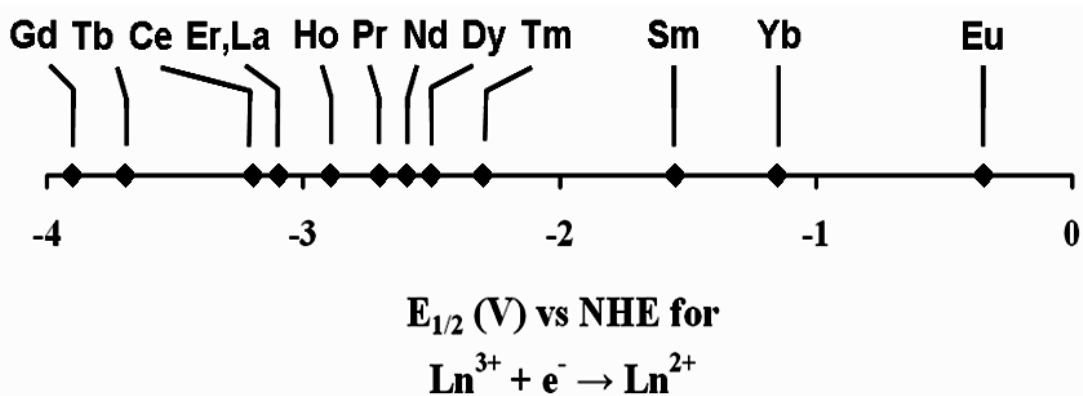
Figure 2.1 Reduction potentials for $Ln^{3+} + e^- \rightarrow Ln^{2+}$ process.

An interesting property of the lanthanide series is, with a few exceptions, the decrease in both the ionic and the covalent radii and the increase in Pauling's electronegativity with increasing nuclear charge Z. This can be attributed to the poor shielding abilities of the 4f electrons thus leading to a diminution of the radial integrals of the outer 5s and 5p electrons with increasing nuclear charge Z. This effect is the main reason for differences found in compounds throughout the lanthanide series, e.g. a slightly different chemistry, but it may also have an influence on the symmetry in ion-implanted systems.

Another general property of the ionized lanthanides is the large number of possible coordination numbers found in compounds, leading to a larger number

of possible symmetries [18, 19]. Coordination numbers up to 8 and 9 are frequently found, but higher coordination numbers often exist as well [19, 20]. This is in contrast to the limited number of coordination numbers found for transition metals. The reason for this can be seen in the more ionic character of the bonding between lanthanides and surrounding ligands, contrary to an emphatic covalent character of the bonding in the case of the transition metals. Lanthanide ions possess relatively high charge densities and have a strong electrostatic nature in their bonding, as the ions are polarizing and can be classified as hard Lewis acids. The 4f orbitals in Ln^{3+} ions are well shielded by the 5s and 5p orbitals, and therefore do not participate directly in bonding (*Figure 2.2*).
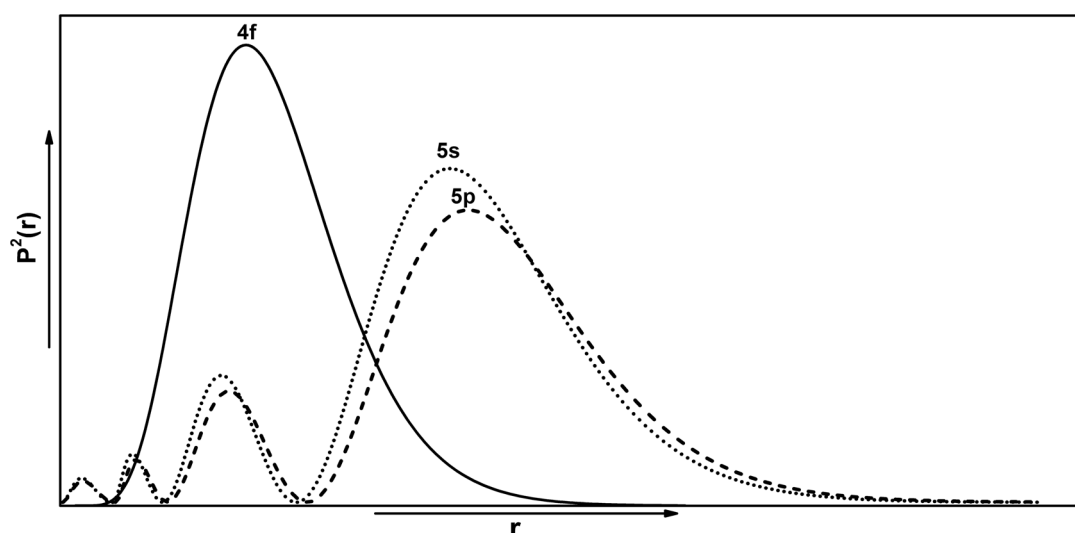
Figure 2.2 Typical radial electron distribution for trivalent lanthanide ions. The square of the radial wavefunction multiplied by the square radius for 4f, 5s and 5p electrons is plotted against the radius (adapted from [21]).

2.3. Introduction to Luminescence

A phosphor or luminescent material is by definition a solid that "converts certain types of energy into electromagnetic radiation over and above thermal radiation" [4]. Phosphors can take a number of forms usually consisting of a host material/matrix doped with activator atoms. Many efficiently fluorescing materials are those that originate from a deliberately added impurity [15]. The added activator atoms are usually rare-earth (lanthanides) ions or transition metals. Other luminescence centers include actinides, heavy metals, electron-

14

hole centers and ZnS-type semiconductors. Such solids can be found among the transition metal compounds and the rare earth compounds of different types. A large variety of phosphors for diverse technological applications is known. The scientific models can explain the optical properties of the phosphors.

The term luminescence comes from the Latin (*lumen* = light) and was first introduced as *luminescenz* by the physicist and historian of science, Eilhardt Wiedemann in 1888 for "all those phenomena of light which are not solely conditioned by the rise in temperature", as opposed to incandescence [22]. Luminescence is *cold light* whereas incandescence is *hot light*. Luminescence induced by light energy is termed photoluminescence and is formally divided into two categories: fluorescence and phosphorescence. Fluorescence is defined as the process of allowed radiative emission that occurs from a singlet-excited state to a singlet-ground state. In excited singlet states, the electron in the excited orbital is paired (of opposite spin) to the second electron in the ground-state orbital. Consequently, return to the ground state is spin-allowed and occurs rapidly by emission of a photon. The emission rates of fluorescence are typically 10^{-8} s, so that a typical fluorescence lifetime is near 10 ns. Phosphorescence is emission of light from triplet-excited states, in which the electron in the excited orbital has the same spin orientation as the ground-state electron. Transitions to the ground state are forbidden and the emission rates are slow ($10^{-3} - 10^{0}$ s), so that phosphorescence lifetimes are typically milliseconds to seconds. The two terms are still open for discussion. Earlier literature refers to phosphorescence for emissions with lifetime > 10^{-3} s, whereas recent literature suggests lifetime > 10^{-8} s. Luminescence is an all-encompassing term that refers to emission of light from any substance and occurs from electronically excited states. Therefore, luminescence will be used to describe any radiative transition that cannot be defined as either fluorescence or phosphorescence, such as samarium luminescence.

2.4. Principles of Lanthanide Luminescence

As the 4f electrons of the lanthanides are well shielded from the environment, the spectroscopic and magnetic properties of these ions (e.g., electronic spectra and crystal-field splitting) are largely independent of environment (solvent, coordinated ligands, etc.). The number (N) of configurations for n electrons rapidly increases with the number of 4f electrons:

$$N = \frac{14!}{n!\,(14-n)!}, \qquad 1 \le n \le 13$$

The lowest energy term for each ion consistent with the predictions of Hund's first and second rules [23, 24]. Since all configurations have different energies, the lanthanides tend to exhibit rich and complex energy level structure. Due to the insignificant dependence of the Ln emission wavelength on the host material one can compile quite universal energy level scheme for the description of the essential absorption and emission bands of such ions, the so called "Dieke diagram" (*Figure 2.3*) [25].
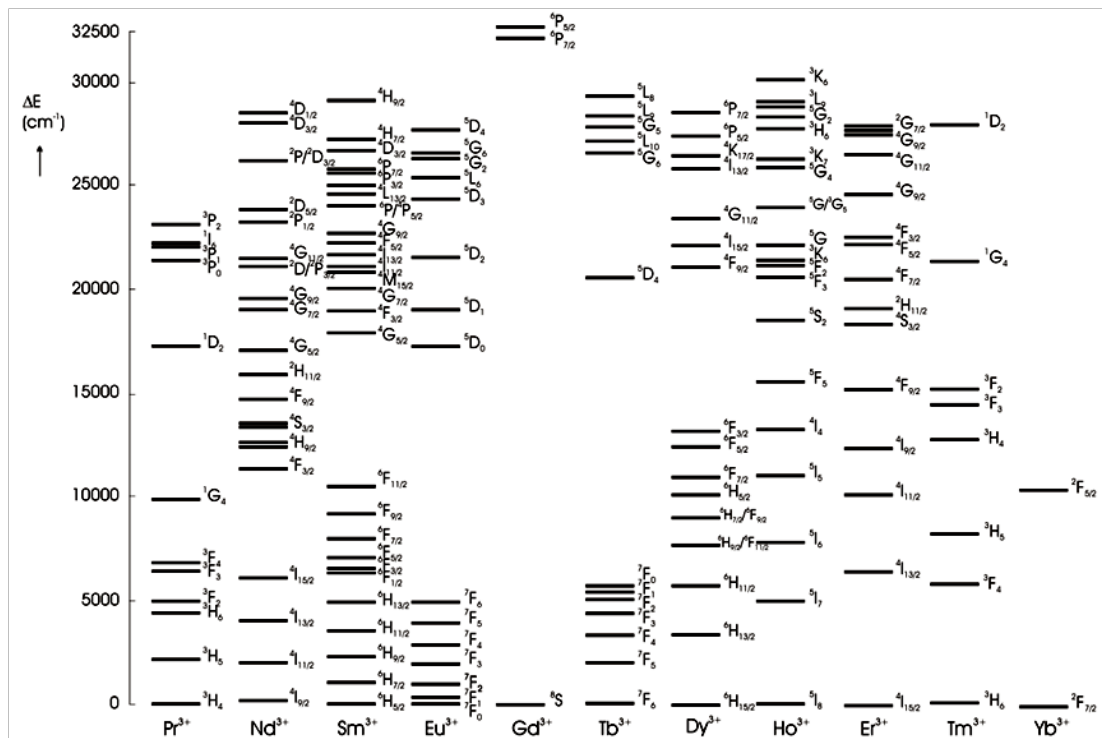
Figure 2.3 Energy level diagrams of the lanthanide ions.

16

The energies of the terms are determined by a combination of interelectronic repulsion, spin-orbit coupling and, in a coordination environment, the ligand field. The interactions that split up the levels belonging to the [Ln]$4f^n$ configuration are clarified in *Figure 2.4*, where the Sm^{2+} ion is taken as an example.

The first perturbation is the *electron repulsion* within the 4f orbitals. This Columbic interaction yields terms with a separation in the order of 10^4 cm^{-1} [26]. These terms are in turn split into several *J*-levels by a second perturbation, the spin-orbital coupling, which is relatively large (10^3 cm^{-1}) because of the heavy lanthanide nucleus [27]. These levels, in turn, can be split again into what are termed Stark sublevels due to ligand field effects from the coordination sphere around the lanthanide; Stark sublevel splitting is on the order of 10^2 cm^{-1} (*Figure 2.4*) [28].
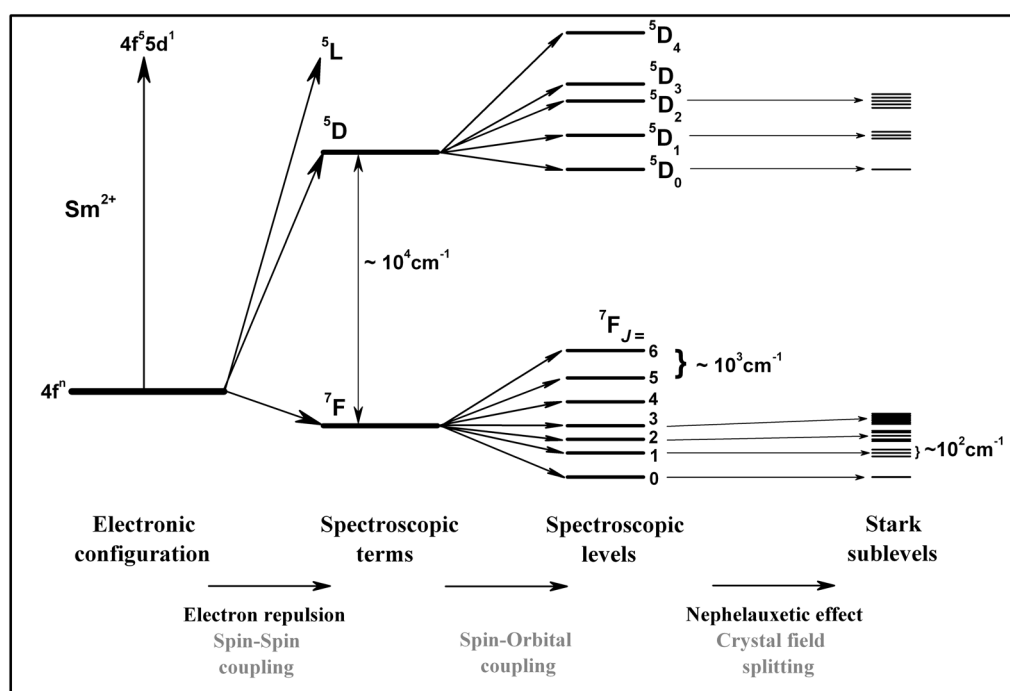
Figure 2.4 Splitting of the energy levels belonging to the [Ln]$4f^6 5d^0$ configuration (example given for Sm^{2+}).

In the *Russell-Saunders coupling scheme*, the electron repulsion is considered to be much larger than the spin-orbital coupling. The individual orbital angular momentum and electron spin angular momentum of all the electrons combine into a total atomic orbital angular momentum *L* and a total

spin angular momentum **S**. The total angular moment **J** is given by the coupling of **L** and **S**. This scheme is not correct for the lanthanides but neither is the *j-j coupling scheme* where the spin-orbital coupling is larger than the electron repulsion. It has been found that the LS-coupling describes the lighter elements, where the electrostatic interaction is relatively strong, whereas in the heavier atoms the *j-j* coupling is more appropriate. The lanthanide atoms lie somewhere between and neither coupling scheme is wholly appropriate. More accurately, the quantum states of lanthanide atoms and ions can be described as intermediate coupling states, which can be considered as mixed states (linear combinations) of several **LS** states [29]. In the *intermediate coupling scheme,* the Coulombic and spin-orbital interactions are simultaneously introduced. Terms with the same **J** but different **L** and **S** can mix. **L** and **S** are no longer valid quantum numbers, but **J** is. Consequently *free ion levels* are described by the term symbols $^{(2S+1)}L_J$. The **LS** notation is most appropriate for the states near to the ground state. The effect of mixing is relatively small on the energy of the levels but can be significant on the optical transition probabilities between the states.

When a lanthanide is surrounded by a coordinating environment, with inorganic or organic ligands, all the electrons of the system, other than those of the lanthanide ion itself, destroy the spherical symmetry of the "free ion". Usually, this effect is called the *crystal-field perturbation*. It is a good approximation to consider only the first coordination sphere, because of the good shielding of the f electrons. When individual **J**-levels are split up further by the crystal field, **J** mixing is allowed. Thus, **L, S** and **J** are no longer valid quantum numbers but for convenience, the name of the mixed term is derived from the largest contributing term. As mentioned earlier the average energy gap introduced between the levels by this perturbation is 10^2 cm^{-1}. When the lanthanide is placed in a magnetic field, there is an additional perturbation: the *Zeeman perturbation*. All remaining degeneracy is destroyed. This results in the overall emission peak position remaining largely unchanged as the f-electrons remain shielded, but the emission profile of a lanthanide (defined as

the relative intensity and degree of splitting of emission peaks) can vary greatly depending on modulation of these influences [30, 31]. The number of Stark sublevels depends on the site symmetry of the lanthanide ion, and these can be thermally populated at room temperature, yielding emission spectra that are more complex.

Ions with an odd number of 4f electrons, after forming **Ln** ions, have electronic doublet levels, so-called Kramer's doublets, with magnetic moments of the order of a Bohr magneton. For non-Kramer's ions, with an even number of electrons, the levels are electronic singlets and the electronic angular momentum is quenched by the crystal field, except if the ions are located in a site with axial or higher symmetry, in which case so called non-Kramer's doublets occur [32, 33]. Ions with a non-quenched electronic angular momentum experience large first-order Zeeman and hyperfine interactions. According to Kramer's theorem, the maximum number of states arising from a *J*-manifold of an electronic configuration with odd number of electrons is $(2J + 1)/2$; each level remains at least doubly degenerated. Such two-fold degeneracy can be removed, in principle, by applying external magnetic field. For electronic configurations with even number of equivalent electrons, the *J*-state degeneracy can be removed completely and the number of the states is $2J + 1$. Based on this it is expected that the luminescence spectra of **Ln** ions can be used as probes for local crystal field symmetry at the impurity centre.

Due to spin-orbit coupling, the excited states of the lanthanides are well separated from the ground state manifold. Thus, the excited states are thermally inaccessible and ideal for electronic transitions. With the exceptions of the $4f^0$ and $4f^{14}$ species (La^{3+} and Lu^{3+}), all lanthanide ions absorb electromagnetic radiation, primarily in the visible region, which is manifested in f-electrons from the partially filled 4f subshell being excited from the ground state to an excited state.

4f-4f transitions are forbidden by the Laporte selection, which means transition cannot occur between the same shells ($\Delta L \neq 0$). In other words, the parity of final and initial state should be changed to obtain the allowed

transition. However observation of these transitions is explained through simple configuration mixing caused by a non-centrosymmetric crystal field, allowing opposite–parity excited configuration to become slightly mixed into $4f^n$ by the Judd [34] and Ofelt [35] theory. Thus, when the ion is located at a site without inversion symmetry, the electric dipole transition may become allowed by the admixture of states from opposite-parity configuration (like 5d) into 4f wave functions, due to the odd-parity crystal field [36]. The transitions are derived, in most cases, due to forced electrical dipole transitions. In some cases, considerable contribution can also be made by magnetic dipole transitions. However, electric dipole transitions are much weaker in lanthanides [21]. Electronic transitions must involve promotion of an electron without a change in its spin ($\Delta S = 0$) and with a variation of either the total angular momentum and the total angular quantum number of one unit at most ($\Delta L = 0, \pm 1$; $\Delta J = 0, \pm 1$). Though absorption of radiation can in theory promote the lanthanide ion to any energetically accessible state, emission normally occurs only from the lowest lying spectroscopic level of the first excited term due to rapid internal conversion [4]. In cases of low symmetry or vibronic coupling, the f-f transitions can gain intensity through f- and d-state mixing with higher electronic states of opposite parity [37]. Broad $4f^n \rightarrow 4f^{n-1}5d^1$ transitions can also be seen in the infrared region for some lanthanides. These transitions can be attributed to another class of important spectroscopic features emerging from lanthanide ions. The 5d states differ from 4f states by their remarkably stronger coupling to crystal lattice vibrations and less localized nature. Furthermore, inter-configurational transitions from $4f^{n-1}5d^1$ state are parity allowed resulting in 10^4 times higher absorption cross section compared to f-f transitions. Due to the latter and relatively high energy needed for the excitation, these transitions are becoming popular in UV lasers and scintillator applications [38].

2.5. Intraconfigurational f-f Transitions Selection Rules

Electronic transitions occur through the interaction of atoms or molecules with the electric or the magnetic component of electromagnetic radiation. Since the start- and end-state of these transitions have the same parity, electric-dipole transitions are forbidden by the Laporte selection rule and only magnetic dipole transitions can occur [39]. Magnetic dipole transitions are generally weaker than electric dipole transitions by a factor of 10^5. In non-centrosymmetric systems, electric dipole transitions can be induced by mixing of configurations of opposite parity (e.g. $4f^{n-1}5d^1$) in the $4f^n$ configuration by the crystal-field potential (this is the perturbation of the lanthanide energy states caused by the interaction of the f-electrons with the crystal field) [34, 35] or by vibronic interactions. These *induced electric dipole transitions* have a small intensity. The molar absorption for 4f-4f transitions typically are around 10 %Lmol^{-1}cm^{-1}. In the case of crystallographic sites with inversion symmetry, the Laporte selection rule can be weakened by non-centric distortions like lattice defects. In general, the weakening for sites with inversion symmetry is still considerably smaller than the weakening for non-inversion sites. Magnetic dipole transitions have different selection rules than the electric dipole transitions [40]. Finally, the atomic spectra have to obey the following selection rules:

– $\Delta \mathbf{S} = 0$, the overall spin is not allowed to change, because light does not affect the spin.
– $\Delta \mathbf{L} = 0, \pm 1$, with $\Delta \mathbf{l} = \pm 1$, the orbital angular momentum of an individual electron must change.
– $\Delta \mathbf{J} = 0, \pm 1$, but $\mathbf{J} = 0 \leftrightarrow \mathbf{J} = 0$ is forbidden.
– Laporte selection rule, which forbids electric dipole transitions between levels with the same parity, examples are electronic transitions within the d-shell, within the f-shell, and between d and s shells.

In the case of lanthanide ions with an even number of electrons some additional selection rules apply: (1) $J = 0 \leftrightarrow J' = 2, 4, 6$ should be strong and (2) $J = 0 \leftrightarrow J' = 1, 3, 5$ should be weak.

Magnetic dipole transitions within the $4f^n$ configuration, which obey the selection rule $\Delta J = 0, \pm 1$ are allowed (except for $J = 0$ to $J = 0$), but have low strengths. The electric dipole intra-4f transitions are in principle parity forbidden, and those transitions that do not occur within the ground multiplet may also be spin-forbidden ($\Delta S \neq 0$). However, in an asymmetric environment, the electric dipole f-f transitions become weakly allowed by mixing of opposite parity wave functions (primarily the 5d wave functions) into the 4f wave functions. In other words the parity forbidden intra-4f-transitions gain some intensity from the allowed 4f-5d transitions [37].

The spin selection rule is relaxed by the fact that heavy atoms have large spin-orbit couplings. Because the strengths of these induced electric dipole transitions are in the same order of magnitude as those of magnetic dipole transitions, both transitions can be observed in lanthanide absorption and emission spectra. The forbidden character of intra-4f transitions causes them to have low intensities and relatively long luminescence lifetimes (in the range of µs to ms).

As mentioned before, f-electrons are not much influenced by local changes in the environment, because of the efficient shielding by filled 5s and 5p orbitals. As a result, the intensities of the transitions are, in general, not much affected by the environment. Some transitions are however very sensitive to small changes of crystal field. These transitions are called *hypersensitive transitions* and obey to the selection rules $\left| \Delta S \right| = 0$, $\left| \Delta L \right| \leq 2$ and $\left| \Delta J \right| \leq 2$ [41]. The intensities of these transitions may be up to 200 times larger than the corresponding transition while the other transitions are generally approximately the same. The hypersensitive transitions are useful tools in the analysis of lanthanide spectroscopic data.

2.6. Configurational Coordinate Diagram

The energy level diagram of lanthanide metal ions forms a starting point for the analyses of their luminescence properties. The configurational coordinate model is often used to explain optical properties of a localized center, particularly the effect of lattice vibrations. In this model, a luminescent ion and the ions at its nearest neighbor sites are selected for simplicity. In most cases, one can regard these ions as an isolated active center by neglecting the effects of other distant ions. In this way, the huge number of actual vibrational modes of the lattice can by approximated by a small number or a combination of specific normal coordinates. These normal coordinates are called the configurational coordinates. The configurational coordinate model explains optical properties of a localized center on the basis of potential curves, each of which represents the total energy (E) of the ion in its ground or excited state as a function of the configurational coordinate (*Figure 2.5*). Here, the total energy means the sum of the electron energy and ion energy. To understand how the configurational coordinate model is built, one is first reminded of the adiabatic potential of a metal-ligand dimer, in which the variable on the abscissa is simply the inter-atomic distance. This simple model can explain a number of facts qualitatively, such as:

– Stokes' law; i.e., the fact that the energy of absorption is higher than that of emission in most cases. The energy difference between the two is called the Stokes' shift;

– widths of absorption or emission bands and their temperature dependence;

– thermal quenching of luminescence.

In *Figure 2.5* R_0 is the interatomic distance at the equilibrium of the ground state, and E_0 is the total energy at $R = R_0$. The spatial distribution of an electron orbital is different between the ground and excited states, giving rise to a difference in the electron wavefunction overlap with neighboring ions. This difference further induces a change in the equilibrium position and the

force constant of the ground and excited states, and is the origin of Stokes' shift. In the excited state, the orbital is more spread out, so that the energy of such an electron orbital depends less on the configuration coordinate; in other words, the potential curve has less curvature. The nucleus of an emitting ion stays approximately at the same position throughout the optical processes. This is called the Franck-Condon principle. Consequently, electronic state transition times are much shorter than vibrational relaxation of nucleus and therefore assumed to occur in static conditions (vertical lines for transitions). This approximation is quite reasonable since an atomic nucleus is heavier than an electron by 10^3 to 10^5 times. The optical absorption proceeds from the equilibrium position of the ground state. The probability for an excited electron to lose energy by generating lattice vibration is from 10^{12} to 10^{13} s^{-1}, while the probability for light emission is at most 10^9 s^{-1}. Consequently, state **B** relaxes to the equilibrium position **C,** because relaxation from excited vibrational states is much faster than emission [42]. This is followed by the emission process **C→D** and the relaxation process **D→A**, completing the cycle. The excitation (absorption) and emission spectra contains one sharp line at the same position, corresponding to the transition from the lowest level of ground and excited states. This transition is called the zero-vibrational or zero-phonon transition, since no vibrations are involved.

At temperatures above 0 K, electrons are distributed over different vibrational levels according to the Boltzmann's law. The amplitude of this oscillation causes the spectral width of the absorption transition. If the temperature is high enough, electrons in the excited state can intersect the ground state curve (point **Q** in *Figure 2.5b*) allowing vibrational relaxation (via phonon release) to the ground state without any radiative emission [43]. It can be described as the absorption of thermal energy (phonon) from point **C**, which excites the electrons to the intersection point **Q**. Since non-radiative processes now can take place, the observed luminescence intensity from a large quantity of excited ions will diminish, explaining the thermal quenching behavior that is observed for most phosphors. When the temperature is

elevated, electrons are spread over a number of vibrational levels in the excited state. Since radiative transitions can take place between any of the vibrational states in the excited and ground states, a broadening of the emission lines is expected [43].
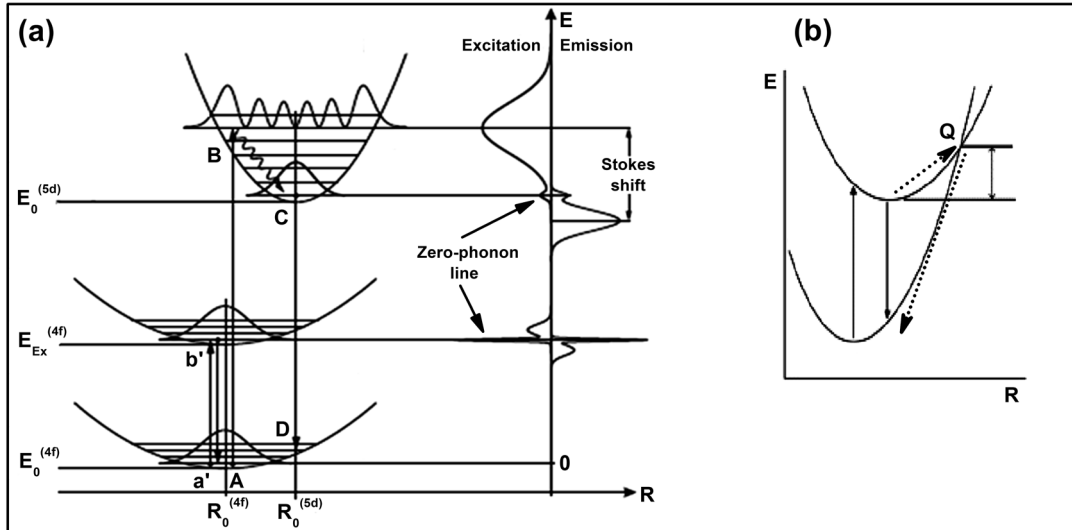
Figure 2.5 General scheme for explanation of luminescence transition according to the Franck-Condon principle in a configurational coordinate diagram, showing the parameters energy (E) and configurational coordinate (R).

2.7. Quenching Processes

There are mainly two different mechanisms which can inhibit emission of photons by excited luminescent centers. This is known as luminescence quenching and in turn may be classified as a) multiphonon relaxation; b) cross-relaxations and energy migration.

2.7.1. Multi-phonon Relaxation

A phonon is a quantized vibration mode occurring in a crystal lattice. Another description for a phonon is quantized thermal energy. Phonon relaxations correspond to the collisional decay of an excited energy level, due to the crystalline lattice vibrations or, in other words, to the rapid short-range movement of the closely spaced atoms. The process when the excited state is depopulated by the surroundings in the form of vibrational energy, often referred to as phonon emission. Hereby, the energy difference between the

excited states is transferred to one or more phonons. This relaxation is normally described as a leakage process. The effectiveness of this process depends on the availability of high-energy vibrations in the surroundings and the energy difference between the energy levels of the lanthanide ion. Multiphonon relaxations between two energy states occur by the simultaneous emission of several phonons that are sufficient to conserve the energy of the transition. *Table 2.1* reports typical phonon energies of different matrices; the probability of multiphonon relaxation may be assessed by using a simple energy gap model [44]. To reach luminescence from an ion with high radiative emission efficiencies the non-radiative relaxation caused by multiphonon relaxation has to be minimized. For this case large energy-gaps, in the region of $10^3 - 10^4$ cm^{-1}, between the excited states and the next lowest levels are useful. Additionally minimizing the highest-phonon-energy of the hosts leads to an increase of the number of required phonons for the multiphonon relaxation to bridge this energy gab. The more phonons are needed to bridge the gap, the higher the efficiency of the radiative depopulation. The intensity of the vibronic transition is dependent on the square overlap integral (Franck-Condon factor) of the initial and final vibrational states and this overlap decreases rapidly as the number of vibrational quanta increases [45]. This is summarized in the theory of the energy gap law [46]. It is common to assume that non-radiative relaxation is inefficient if more than $5 - 7$ phonons are necessary to bridge the gap.

Table 2.1 The maximum of phonon energy of the various hosts.

Material	Phonon energy (cm^{-1})
Borate	≈ 1400
Phosphate	$\approx 1100 - 1200$
Silicate	≈ 1100
Germanate	≈ 900
Tellurite	≈ 700
Aluminate	≈ 700
Fluorozirconate	≈ 500
Sulfide (Ga, La)	≈ 450

2.7.2. Cross-relaxation and Energy Migration

Cross-relaxation and on the other hand cooperative up-conversion processes leads to fluorescence quenching, i.e. to the decrease of fluorescence intensity when the lanthanide concentration is increased. Cross-relaxation is the full or partial transfer of excitation energy to an acceptor in a lower level. This process can be very efficient, if the energy differences in the participating donor and acceptor levels are resonant or the energy needed to excite the acceptor is slightly smaller than the energy provided by the donor. With increasing concentration of lanthanide ions, the ion spacing decreases and may be small enough to allow them to interact and transfer energy. Cross-relaxation may occur between lanthanide ions if they have two pairs of energy levels characterized by the same energy gap ΔE. An excited ion **D** (donor) transfers half of its energy to a ground-state ion **A** (acceptor), so that both ions move to a same intermediate level, from which they decay non-radiatively to the ground level. Example of Sm^{3+} cross-relaxation pathway is given in *Figure 2.6*. Cooperative up-conversion process occurs between two excited ions **D** and **A**: **D** gives its energy to **A**, so that **D** relaxes to ground state, while **A** goes to a higher energy level. From this higher level **A** can relax either emitting a photon with higher energy (i.e. higher frequency and lower wavelength) than the exciting photon or via phonons and a lower-energy photon. In any case, at least one exciting photon is lost for the amplifying process. Cross-relaxation is often used to sensitize ions with small absorption cross section by co-doping with ions with strong absorption to achieve a more efficient excitation.

Energy migration is another form of cross-relaxation between two ions of the same sort. If the excited state energy levels of two identical ions are resonant, then the energy can be transferred to the neighboring ion by cross-relaxation and travel through the material hopping from one ion to the other. This can be very useful if energy transfer is desired as in sensitized systems or can be harmful if the excitation energy is transferred away from the active ion to unwanted impurities. Resonant ions are those, which can transfer energy when they have similar separations between the energy levels. The small

mismatch in energy can be compensated by the emission or uptake of a phonon. An increase in the doping concentration leads to a faster energy migration through the material, making the chance of meeting a quenching site higher. For reasons of cross-relaxation and energy migration, high doping concentrations often lead to a decrease in luminescence intensity and luminescence lifetime [47].
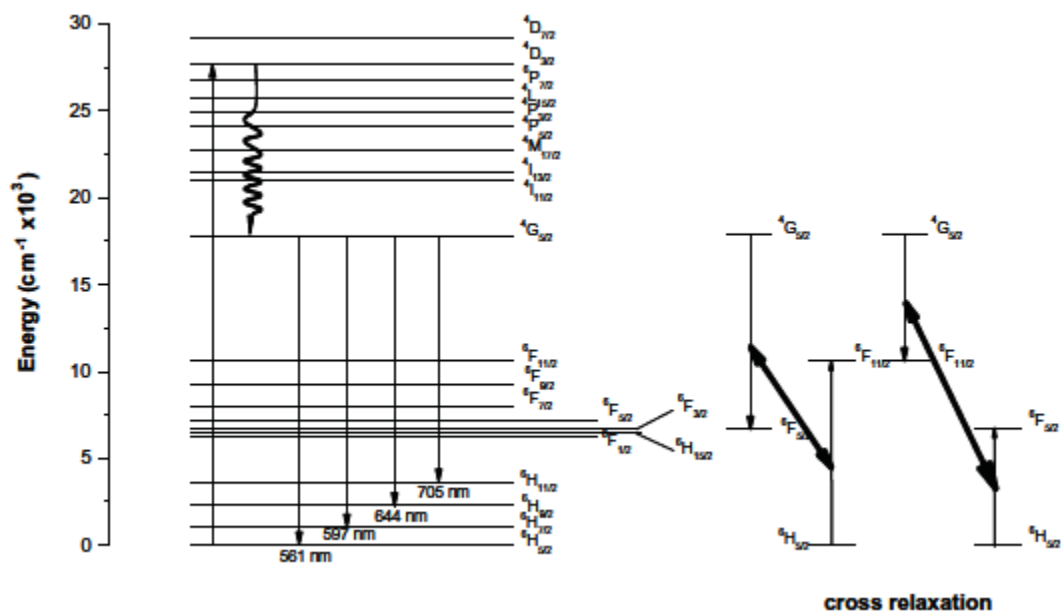

Figure 2.6 Energy level diagram showing cross-relaxation channel for Sm^{3+}-doped PKFBASm glasses [48].

Chapter 3. Characteristics of Samarium

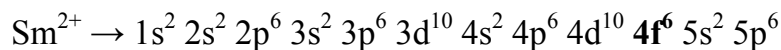## 3.1. The Ground State of Samarium Ion

Energy levels of free rare-earth ions are derived starting from classical Russell-Sounders approximation. Electrons in a free atom reside inside a shell and are characterized by a particular value of n, the principal quantum number. Within each shell electron can reside on $l = n - 1$ sub shells. These sub shells are sometimes referred to s, p, d, f etc. orbitals, depending on the value of the orbital quantum number l (l = 0, 1, 2, 3 for the s, p, d, f orbitals). A quantum mechanics approach to determine the energy of electrons in an atom or ion is based on the results obtained by solving the Schrödinger wave equation for the hydrogen atom. The various solutions for the different energy states are characterized by the three quantum numbers: n, l and m_l. A fourth quantum number, which is denoted as m_s and describes the electron spin states, is also added to the final set of quantum numbers, uniquely describing a particular state.

The electronic configuration of Sm atom is, for example:

$$Sm^0 \rightarrow 1s^2\, 2s^2\, 2p^6\, 3s^2\, 3p^6\, 3d^{10}\, 4s^2\, 4p^6\, 4d^{10}\, \mathbf{4f^6}\, 5s^2\, 5p^6\, 6s^2$$
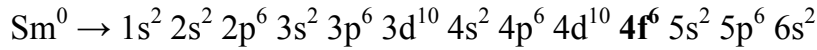
In short form – $[Xe]4f^5 5d^1 6s^2$ for idealized and $[Xe]4f^6 6s^2$ for observed configuration. The discrepancy arises because of comparable energy of the 5d and 4f orbitals, so that is why the distinction between the two is not easy.

When samarium is incorporated into materials it become triply or doubly ionized, e.g. to Sm^{3+} or Sm^{2+}. Therefore, the electronic configuration must be changed as below.

$$Sm^{3+} \rightarrow 1s^2\, 2s^2\, 2p^6\, 3s^2\, 3p^6\, 3d^{10}\, 4s^2\, 4p^6\, 4d^{10}\, \mathbf{4f^5}\, 5s^2\, 5p^6$$
$$Sm^{2+} \rightarrow 1s^2\, 2s^2\, 2p^6\, 3s^2\, 3p^6\, 3d^{10}\, 4s^2\, 4p^6\, 4d^{10}\, \mathbf{4f^6}\, 5s^2\, 5p^6$$
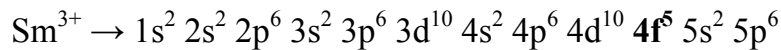
The electrons that lie inside of the $4f^6$ shell are shielded by the $5s^2 5p^6$ closed subshells. The ground electronic configuration, with taking the angular momentum and the total spin into account, amounts to 2002 for Sm^{3+} and 3003

for Sm^{2+} for the perfectly isolated samarium ions [30]. The degeneracy is removed by applying the spin-spin, orbital-orbital and spin-orbital interaction. Finally, it is possible to determine which electronic levels are going to be allowed by the selection rules. Below, the fundamental electronic spectroscopic notation of $Sm^{2+/3+}$ is introduced.

The ground state can be assigned by Hund's rules. These rules can be summarized as follows. The notation **S** and **L** indicate the spin angular momentum and orbital angular momentum, respectively.

1. For a given electron configuration, the term with maximum multiplicity has the lowest energy. Since multiplicity is equal to $(2\mathbf{S} + 1)$, this is also the term with maximum **S.**

   → *Spin – Spin Interaction*
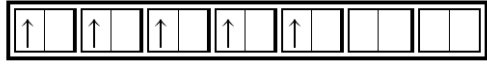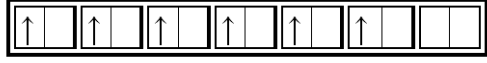
2. For a given multiplicity, the term with the largest value of **L**, has the lowest energy.

3. For a given term, in an atom with outermost subshell half-filled or less, the level with the lowest value of **J**, lies lowest in energy. If the outermost shell is more than half-filled, the level with highest value of **J**, is lowest in energy. **J** is the total angular momentum, $\mathbf{J} = \mathbf{L} + \mathbf{S}.$

   → *Spin – Orbital Interaction*

4. The wave function (product of angular and spin wave function) should be anti-symmetric.

The spectroscopic notation of splitting energy levels under spin-spin interaction is $^{(2S+1)}\mathbf{\Gamma}$, where $\mathbf{\Gamma} = \mathbf{S}$, $\mathbf{P}$, $\mathbf{D}$, $\mathbf{F}$, $\mathbf{G}$, $\mathbf{H}$, $\mathbf{J}$, $\mathbf{K}$, $\mathbf{L}$… if the angular momentum **L** equals to 0, 1, 2, 3, 4, 5, 6, 7, 8… . Under the spin-orbital interaction it is necessary to consider the total angular momentum **J**, where $\mathbf{J} = \mathbf{L} + \mathbf{S}$ ($|\mathbf{L} - \mathbf{S}| \leq \mathbf{J} \leq \mathbf{L} + \mathbf{S}$). This interaction will split $^{(2S+1)}\mathbf{\Gamma}$ into $^{(2S+1)}\mathbf{\Gamma}_{\mathbf{J}}$.

Table 3.1 Russell-Saunders notation of Sm^{2+}/Sm^{3+} ground state.

	m_l	3	2	1	0	-1	-2	-3	S^a	L^b	J^c	$^{2S+1}L_J{}^d$
Sm^{3+} $4f^5$	$S_{max} = \frac{1}{2}+\frac{1}{2}+\frac{1}{2}+\frac{1}{2}+\frac{1}{2}$ ↑ ↑ ↑ ↑ ↑ $L_{max} = 3 + 2 + 1 + 0 - 1$								5/2	5	5/2	$^6H_{5/2}$
Sm^{2+} $4f^6$	$S_{max} = \frac{1}{2}+\frac{1}{2}+\frac{1}{2}+\frac{1}{2}+\frac{1}{2}+\frac{1}{2}$ ↑ ↑ ↑ ↑ ↑ ↑ $L_{max} = 3 + 2 + 1 + 0 - 1 - 2$								3	3	0	$^7F_0$

[a] $S = |\Sigma m_s| \rightarrow m_s = +\frac{1}{2}$ (↑) or $m_s = -\frac{1}{2}$ (↓)
[b] $L = |\Sigma m_l|$
[c] $J = |L - S|$ (less than half-filled shell)
[d] Predicted ground state according to Hund's rules

The 4f shell of Sm^{2+} has 6 and Sm^{3+} – 5 electrons. The maximum multiplicity for spin momentum is obtained when electrons are in spin up states. For Sm^{2+} the S_{max} is 3 and maximum multiplicity $(2S + 1)$ is 7. With all spin up states, the wave function of spin part becomes symmetric, which means that the symmetry of the angular part of wave function should be odd. The quantum number of angular momentum of 4f state is 3, which means there is degeneracy of 7 (m_l = 3, 2, 1, 0, -1, -2, -3). In *Table 3.1* is given the configuration of 4f shell electrons presenting the maximum spin multiplicity and the highest degeneracy of angular momentum. Thus, the maximum spin multiplicity is 3 and L_{max} is 3 (F state). Therefore, the lowest energy can be assigned as the ^7F state level. The ground state becomes $^7F_0$ because the 4f sub-shell is less than half filled. Accordingly the ground state for Sm^{3+} is $^6H_{5/2}$ with $L_{max} = 5$ (H state) and $S_{max} = 5/2$.

3.2. Host Dependant Samarium Luminescence

For a number of lanthanides multiple oxidation states are possible, the final oxidation state depending on the choice of raw materials, the method of synthesis and the type of matrix they are incorporated in. Such is the case for samarium, which can be both stable in the trivalent and the divalent state.

31

Although samarium is much more stable in the trivalent state than divalent, consequently only several compounds with Sm^{2+} are known. In that respect, the oxidation state of the samarium in the different lattices could well differ depending on the synthesis temperature and atmosphere used. The luminescence properties of samarium in divalent state are different from the trivalent state. Characteristic Sm^{3+} ($4f^5$) and Sm^{2+} ($4f^6$) transitions can be found in the red part of the visible spectrum (550 – 850 nm). Since the valence change is interconnected to measured optical properties, samarium luminescent and chemical properties are discussed together.

The spectroscopic properties of triply ionized samarium ion doped into a variety of host matrices have been extensively studied [49-52]. It was observed the strong fluorescence in the visible region and discovered that the radiative property of the dopant depends on the chemical environment and the host materials into which it is doped.

The Sm^{3+} ion has a $4f^5$ electron configuration, which is characterized by 198 $^{2S+1}L_J$ free-ion levels. In the presence of a low-symmetric crystal field, these free-ion manifolds split into a total of 1001 crystal-field levels (non-Kramer's degeneracy). Usually the crystal-field fine structure is not resolved due to inhomogeneous line broadening and only emission bands between $^{2S+1}L_J$ manifolds are observed. Only a limited number of the 198 $^{2S+1}L_J$ manifolds can be observed experimentally. Moreover, many of the manifolds are lying so close to each other that is why it is not possible to determine their exact maximum.

The initial level for all the transitions is the $^6H_{5/2}$ ground state of Sm^{3+} (*Figure 3.1*). The first excited state $^6H_{7/2}$ is only ≈ 1100 cm^{-1} above the ground state, but no transitions starting from this level could be detected [53]. The observed emission is due to transitions from the $^4G_{5/2}$ level to the various excited ^6H_J and ^6F_J levels. When Sm^{3+} is excited by blue, violet or ultraviolet light, an intense orange luminescence is observed. When any of the energy levels above $^4G_{5/2}$ is excited, there is a fast non-radiative relaxation to this emitting level. Consequently, the same luminescence spectrum is obtained

regardless the excitation wavelength (same relative intensities). However, the absolute intensities are dependent on the excitation wavelength. The most intense luminescence is observed by exciting the samples at 400 – 405 nm ($\approx$ 25000 cm^{-1}). This is excitation to the $^6P_{3/2}$ level. The orange luminescence color is due to the intense $^4G_{5/2} \rightarrow {}^6H_{7/2}$ transition at around 600 nm ($\approx$ 16700 cm^{-1}).
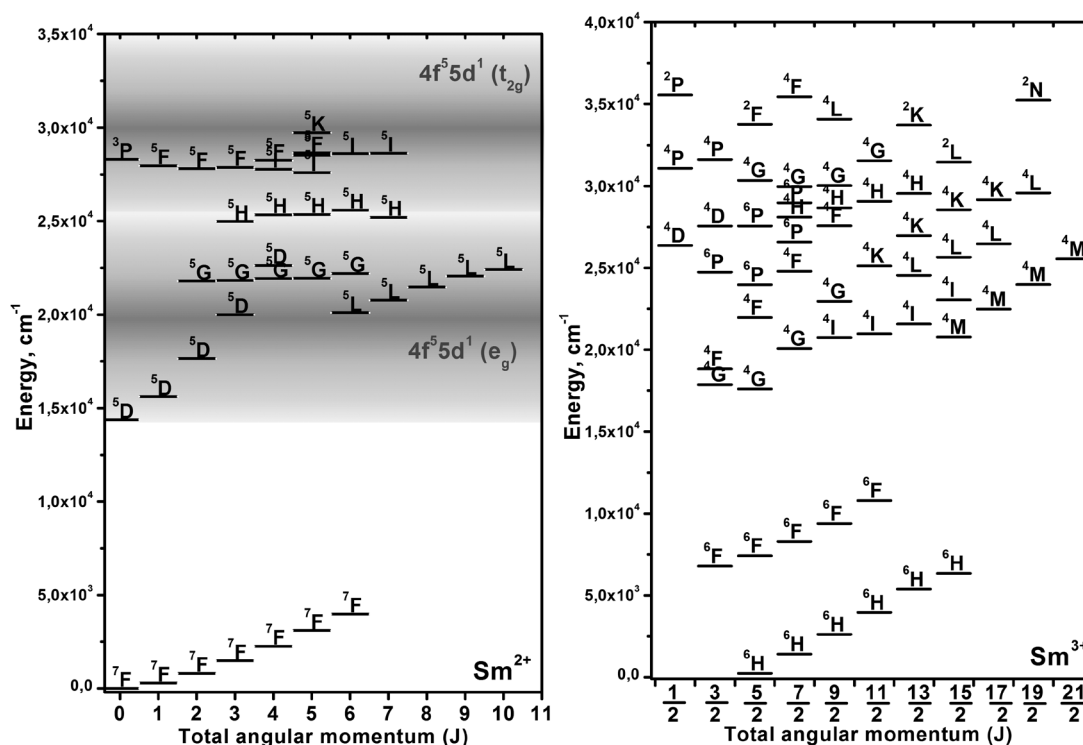
Figure 3.1 Calculated energy level of Sm^{2+} (left) and Sm^{3+} (right) ions by considering spin-spin and spin-orbital interaction.

The degeneracy of the 4f^6 electronic configuration of the divalent samarium ion is 3003. The degeneracy of the 4f^6 configuration is removed by several perturbations acting on the lanthanide ion: electron repulsion, spin-orbit coupling and the crystal field perturbation. After introduction of electron repulsion, the 4f^6 configuration is characterized by 119 $^{2S+1}L_J$ terms. The degeneracy of each term is $(2S + 1)(L + 1)$. The 4f^6 configuration is split by spin-orbit interaction in 295 $^{2S+1}L_J$ levels. The degeneracy of each spin-orbit level is $2J + 1$ (Kramer's degeneracy). This degeneracy is further removed by the crystal field effect, after which the energy levels are characterized by the irreducible representation of the point group. Divalent Sm^{2+} ions have a ground 4f^6 configuration with the lowest spectral term ^7F and the first excited term ^5D,

33

which split into seven multiplets $^7F_0$ to $^7F_6$ and five – $^5D_0$ to $^5D_4$, respectively, due to the spin-orbit interaction. With these splittings, the luminescence spectrum of Sm^{2+} is expected to resemble closely the isoelectronic situation of Eu^{3+}. However, the first excited $4f^55d^1$ configuration for Sm^{2+}, located in the visible and near UV region, is energetically much lower than for Eu^{3+}. This in turn affects various luminescence features of the Sm^{2+} doped crystals, which are well known to depend on the relative position of the lowest $4f^55d^1$ levels with respect to the excited $^5D_0$ multiplet of $4f^6$. Therefore, the excitation mechanism of Sm^{2+} luminescence is quite different from for trivalent lanthanide ions. The parity-allowed transition $4f^6 \rightarrow 4f^55d^1$ can generate notable luminescence and offers enough intensity for the presented optical measurements.

Divalent samarium is a lanthanide ion capable of exhibiting both sharp line and broadband emission spectra, depending on the choice of the host material and the synthesis conditions. The prevailing type of emission is determined by the location of the lowest (emitting) levels due to $4f^5d^1$ and $4f^5$ electron configurations relative to one another. Sm^{2+} ($4f^6$) has its levels arising within 4f-configuration at low energies ($^5D_0$ at about 700 nm, 14300 cm^{-1}) and exhibits 4f–4f emissions in quite a number of compounds, even at room temperature. The position of the $4f^55d^1$ excited levels depends on several factors, such as the crystal field strength and bond covalence between the luminescence center and the ligands. The $4f^55d^1$ excited levels are split into the lower e_g and higher t_{2g} states (in O_h symmetry), where energy separation depends on crystal field strength (*Figure 3.1*). Because of the large spatial extent of the 5d wavefunction it is vibrationally broadened much more than the forced electric-dipole transitions, which occur within the 4f shell. 5d → 4f emission bands in materials are typically several tens of nanometers in width. The luminescence properties of Sm^{2+} are sensitive to the temperature. At low temperatures, the $4f^6 \rightarrow 4f^6$ sharp transitions were detected, while at high temperatures usually additional allowed broadband transition $4f^55d^1 \rightarrow 4f^6$ appears, owing to the thermal population of the $4f^55d^1$ lower level.
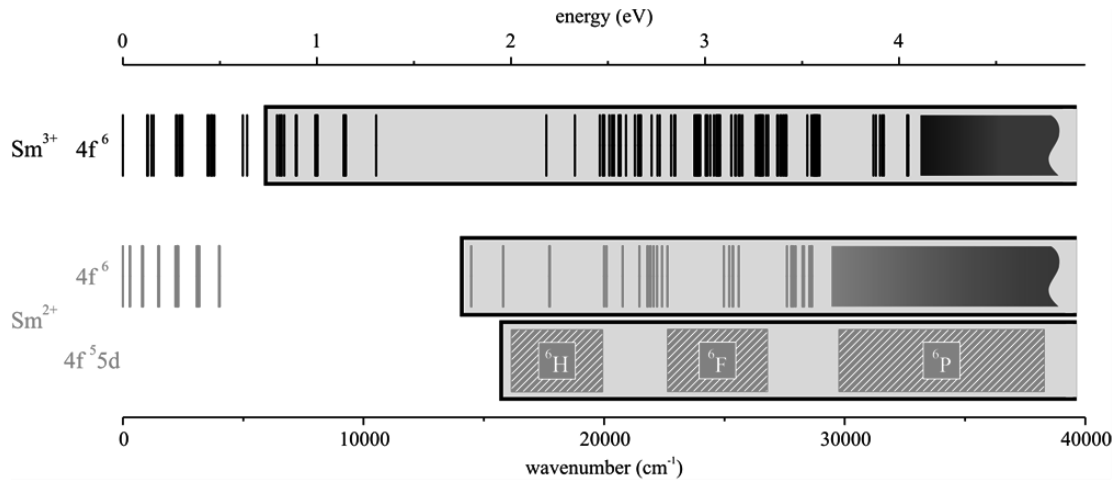
Figure 3.2 Energy level diagram of trivalent (black) and divalent (grey) samarium. The Sm^{2+} energy levels are a combination of the $4f^6$ and the $4f^5 5d^1$ states [36, 54]. The $4f^5 5d^1$ states of Sm^{3+} are in the far VUV (with energies of about 70000 cm^{-1}) [25]. All excited states are highlighted with a grey background. Closely spaced levels are depicted as bands.

Moreover, it can be seen that Sm^{2+} offers some advantages by comparing the trivalent energy level of samarium with the divalent one (*Figure 3.2*). The normal $4f^6$ energy levels are superimposed by the broad energy levels of the $4f^5 5d^1$. For qualitative explanation of excitation data a superposition of the multiplet structure of the $4f^5$ core and the $5d^1$ crystal-field levels is applied [37, 55]. 5d levels, in low symmetry site, can split into maximum five components which can couple with $4f^5(^6H_J)$ and $4f^5(^6F_J)$ core electron substates. These energy levels mainly increase the absorption in the green, blue and UV spectral range.

Usually, there are two kinds of methods for the reduction of Sm^{3+} to Sm^{2+} ions. The first one is heating the Sm^{3+} ions-doped materials in a chemical reducing atmosphere like H_2/N_2 mixture gas, which is effective to reduce Sm^{3+} to Sm^{2+}. The second one is to irradiate the Sm^{3+}-doped samples with high-energy radiation, such as femtosecond laser [56], γ-ray irradiation [57], β-irradiation [58], and X-ray [59]. During the irradiation, free electrons and holes are created. Some electrons can be trapped by Sm^{3+} ions, leading to the formation of Sm^{2+} ions and holes are trapped by other defects. Hence, the luminescence of Sm^{2+} ions is highly dependent on the sample preparation conditions, because of the different defects created by different methods.

The halide compounds are the best-known materials for divalent samarium incorporation. These comprise the alkaline-earth halides MX_2 and halogenofluorides MXF (M = Ca, Sr, Ba; X = Cl, Br), the perovskites ABF_3 (A = Na, K, Rb; B = Ca, Mg) and the alkali halides MX (M = Na, K, Rb; X = Cl, Br, I) [60-63]. In all cases strong reducing conditions were used for samarium reduction. In addition, phosphates ($KSrPO_4$) and borophosphates ($BaBPO_5$) showed suitable characteristics for Sm^{2+} incorporation [64, 65]. Doped $BaSO_4$ also demonstrated samarium reduction [66]. However, there are reports on unusual samarium reduction in high temperature under air. There are only three compounds obtained showing such behavior, e.g. SrB_4O_7, SrB_6O_{10} and BaB_8O_{13} [67, 68]. Following the above mentioned results, few conditions for divalent lanthanide state stabilization in inorganic hosts can be summarized: (1) it is necessary to avoid any oxidizing ions in the structure (NO_3^-, etc.); (2) suitable crystallographic site for Sm^{2+} should be divalent; (3) the substituted cation radius have to be similar; (4) the coordination number (CN) of substituted cation is expected as high as possible [69, 70]. Besides, the tetrahedral anion groups (BO_4, SO_4, PO_4 and SiO_4) in the structure are favorable, due to the lower binding energies.

Sm^{2+}/Sm^{3+}-doped materials, however, are generally observed to be efficient phosphors under ultraviolet or visible excitation and one can reasonably expect that their luminescent properties may be of some interest for industrial applications, in fluorescent lamps for example, where single crystals are not needed. In the framework of an exploration on Sm^{2+}-doped compounds, it have been attempt to work out a simple and reliable method to prepare powder samples containing samarium in the divalent state as impurity.

3.3. Samarium as Structural Probe

The idea of crystal symmetry sensing via lanthanide ion photo-luminescent probes is not new. Lanthanide emission profiles have complex character due to Stark sublevel splitting, which is largely dependent on the site symmetry of the central lanthanide ion. Thus, if the emission (or the absorption) spectrum of a

36

pure lanthanide compound is known, it is in principle possible to determine the point group of the lanthanide site. As described earlier the electric dipole transition $^5D_0$-$^7F_2$ and magnetic dipole transition $^5D_0$-$^7F_1$ of Eu^{3+} have successfully been used to probe the site symmetry changes in low symmetry crystal sites [71, 72]. However, the group theory and resulting crystal-field parameterization of lanthanides is complex and complications such as low site symmetry or the additional degeneracy of odd-electron lanthanides make spectral assignment of crystal-field transitions very difficult. Systems with an odd number of f-electrons (i.e., Sm^{3+}, Gd^{3+}) are nearly impossible to use as probes for the site symmetry around the lanthanide ion due to Kramer's degeneracy [18]. For a crystalline compound with symmetry lower than cubic, every level will be split into maximum crystal-field levels in the absence of an external magnetic field.

The divalent samarium ion has several characteristics useful for probing the site symmetry [73]. First, Sm^{2+} has an even number of electrons ($[Xe]4f^6$), so total degeneracy is removed only in low symmetry cases. Second, the $^7F_0$ ground state of Sm^{2+} is non-degenerate, meaning it will transform as the totally symmetric representation of the point group, which simplifies spectral interpretation significantly. Third, many of the $^{2S+1}L_J$ levels where J is small (and there is a straightforward relationship between crystal-field splitting and crystal-field parameters) are present in the optical region for samarium, meaning crystal field parameters can be measured directly from experimental spectra. Finally, there is very little overlap between the crystal-field levels of different J states, so levels in the ground ^7F_J and excited ^5D_J terms can be easily distinguished in high resolution spectra.

The most interesting and informative transitions in the divalent samarium luminescence spectrum are: $^5D_0 \rightarrow {}^7F_0$ (≈ 685 nm), $^5D_0 \rightarrow {}^7F_1$ ($\approx 690 - 705$ nm), $^5D_0 \rightarrow {}^7F_2$ ($\approx 720 - 730$ nm) and $^5D_0 \rightarrow {}^7F_4$ ($\approx 800 - 820$ nm). All of these are electric dipole transitions with the exception of $^5D_0 \rightarrow {}^7F_1$, which is a magnetic dipole transition [18]. The first peak in the emission spectrum allows for determination of sample purity and significantly narrows down the list of

potential point groups. If the $^5D_0 \rightarrow {}^7F_0$ transition shows any splitting, consequently more than one non-equivalent site is present. This transition is also reported to shift with coordination number, most likely due to an increase in Sm^{2+}-ligand covalency via the nephelauxetic effect [74, 75].

Set of peaks usually found around 690 – 705 nm, allows for further isolation of the correct point group of the compound. If the $^5D_0 \rightarrow {}^7F_1$ transition is split into three peaks, the symmetry must be either orthorhombic (D_2, C_{2v}), monoclinic (C_2, C_s) or triclinic (C_1). If the transition has only two peaks, it leaves the hexagonal, trigonal or tetragonal symmetries (*Figure 3.3*).

If the symmetry is high, more transitions are forbidden by symmetry restrictions; therefore, lanthanides occupying sites of low symmetry will have more peaks within a spin-orbit coupling band than those in site of higher symmetry. This feature is well illustrated by the $^5D_0 \rightarrow {}^7F_2$ ($\approx$ 720 – 730 nm) transition. If the symmetry is found to be orthorhombic, monoclinic or triclinic, the exact point group can be assigned using this transition. If the band at $\approx$ 720 – 730 nm has only three peaks, the point group is D_2, four peaks indicate a point group of C_{2v}, and five peaks leave the remaining point groups (C_2, C_s and C_1) as possibilities. For the hexagonal, trigonal and tetragonal symmetries, further information is required. If polarized spectra can be obtained, distinctions can be made using this and the $^5D_0 \rightarrow {}^7F_4$ transition to clearly identify the point group of the Sm^{2+} coordination sphere (*Figure 3.3*).

The symmetry also has an influence on the radiative lifetime of the $^5D_0$ level. The radiative lifetime is the time for the luminescence to drop to 1/e in intensity in absence of quenching. In the case of a Sm^{2+} ion without inversion symmetry the rate of the forced electric dipole transition is higher than in the case of a Sm^{2+} ion with inversion symmetry. This automatically means that the radiative lifetime of a Sm^{2+} ion in a site with inversion symmetry is longer. Radiative lifetimes of lanthanide ions have been calculated with several methods, of which the Judd-Ofelt theory is the most popular [34, 35]. In this theory, the strength of the electric dipole transitions are calculated from the

absorption spectrum and these strengths can be related to the radiative lifetime.
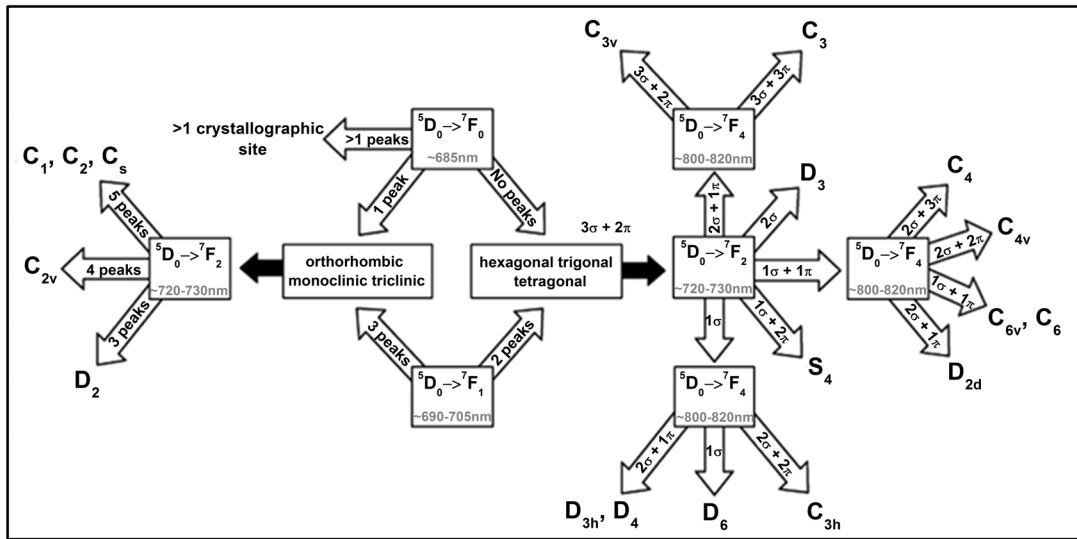
Figure 3.3 Scheme for point group determination based on selected transitions in the Sm²⁺ ion. Modified for luminescence spectrum from references [31, 77].

Such approach is superior to conventional XRD and Raman measurements because of its spatial selectivity and higher efficiency. Compared to Raman the excitation cross-section of luminescence is $\sim 10^4$ times higher allowing much smaller amounts of material to be characterized. As such, the luminescence based detection method in theory could be used even at nano scale, when single atom emitters and fluorescence resonant energy transfer (FRET) microscopy is used [76].

Chapter 4. Properties of the Host Materials

4.1. Crystal Structure of SrB_4O_7

The orthorhombic phase of strontium tetraborate, α-SrB_4O_7 (I), is known for a long time [78]. This compound has attracted attention owing to its interesting physical properties, namely an unprecedented fundamental optical-absorption edge among oxide compounds (~ 130 nm), good luminescent characteristics and an ability to stabilize rare-earth elements in divalent state [79-81]. The compound was reported to be the first example of an anhydrous borate featuring only tedrahedrally coordinated boron in which all the boron and oxygen atoms are involved in the borate network.

SrB_4O_7 (SrTB) falls in a glass-forming range within the SrO-B_2O_3 system and can simply be obtained as a glass. Consequently synthesis of crystalline borate compounds is rather tricky [82, 83]. Several borate compounds appear in crystalline as well as glassy form. The solid-state synthesis using boric acid as the boron source allows the preparation without melting the constituents, which is essential for avoiding glass formation. This necessitates longer reaction times and eventually evaporation of boric acid may cause non-stoichiometry. The process of glass re-crystallization occurs through complex mechanisms with potential formation of other crystalline phases, especially through metastable phases. The phase diagram in *Figure 4.2* reveals five main phases in the SrO-B_2O_3 system: (I) strontium tetraborate (SrB_4O_7), (II) strontium diborate (SrB_2O_4) [84] and its high-pressure form [85], (III) distrontium diborate ($Sr_2B_2O_5$), [86], (IV) tristrontium diborate ($Sr_3B_2O_6$) [87] and (V) strontium hexaborate (SrB_6O_{10}) [88]. However, the phase diagram is not complete, because additional phases are reported: (VI) distrontium hexadecaborate ($Sr_2B_{16}O_{26}$) [89] and (VII) tetrastrontium tetradecaborate ($Sr_4B_{14}O_{25}$) [90]. Two of these phases crystallize in non-centrosymmetric space groups, viz. I - *Pmn*2_1 and VII - *Cmc*2_1. The main feature of all these structures are BO_x units (x = 3, 4). Isolated (IV) or flat pairs (III) of BO_3 triangles, a framework of BO_4 tetrahedra with shared vertices (I, II) and a framework of

triangles and tetrahedra with shared vertices (V, VII) are found in these structures. According to the phase equilibrium diagram SrB_4O_7 congruently melts at 994 ± 10 °C [91]. SrTB crystals were not found to be hygroscopic [92].

SrB_4O_7 crystallizes in the orthorhombic crystal lattice with space group $Pmn2_1$ (31). Its structure consists of an unusual type of borate framework where all boron atoms are tetrahedrally coordinated. Three-dimensional borate network constructs channels parallel to the a- and b-axis with Sr ions located in these channels (*Figure 4.1a*). All the tetrahedra are connected to each other by sharing corners (*Figure 4.1b*) and have the appearance of a layer-like structure because there are comparatively few links in the c-direction. Four independent O atoms can be divided into two groups: O(1), O(2) and O(3) are linked to two B atoms with shorter O–B bonds (0.1416 – 0.1458 nm), while O(4) is linked to three B atoms with longer O–B bonds (0.1536 – 0.1560 nm). Although there are six-membered B–O rings in the borate network parallel to the b-axis, the rings do not belong to the ''conjugated group'' type (*Figure 4.1c*). The unusual feature is the occurrence of an oxygen atom common to three tetrahedra. These triple-coordinated oxygen atoms are located in the second coordination sphere of the Sr atom at a distance of 0.304 – 0.320 nm. The $[BO_4]$ network builds channels parallel to a and b directions and strontium ions fit into these channels. The nine nearest neighbor Sr-O distances are in the range of 0.253 – 0.284 nm (*Figure 4.1d*). The 0.269 nm distance represents only one interaction while the other bonds are repeated by mirror plane building a monocapped square prism polyhedron. The actual coordination is not clearly defined because there are additionally three more oxygen atoms in the range of 0.304 – 0.305 nm. However, the fitted results of $Sm-L_3$ edge EXAFS spectra give coordination number 9 [67]. Nevertheless, the Sr is surrounded by 12 oxygen atoms giving low symmetry site. The shortest Sr-B distance is 0.311 nm and the closest Sr atom is situated in 0.424 nm distance.
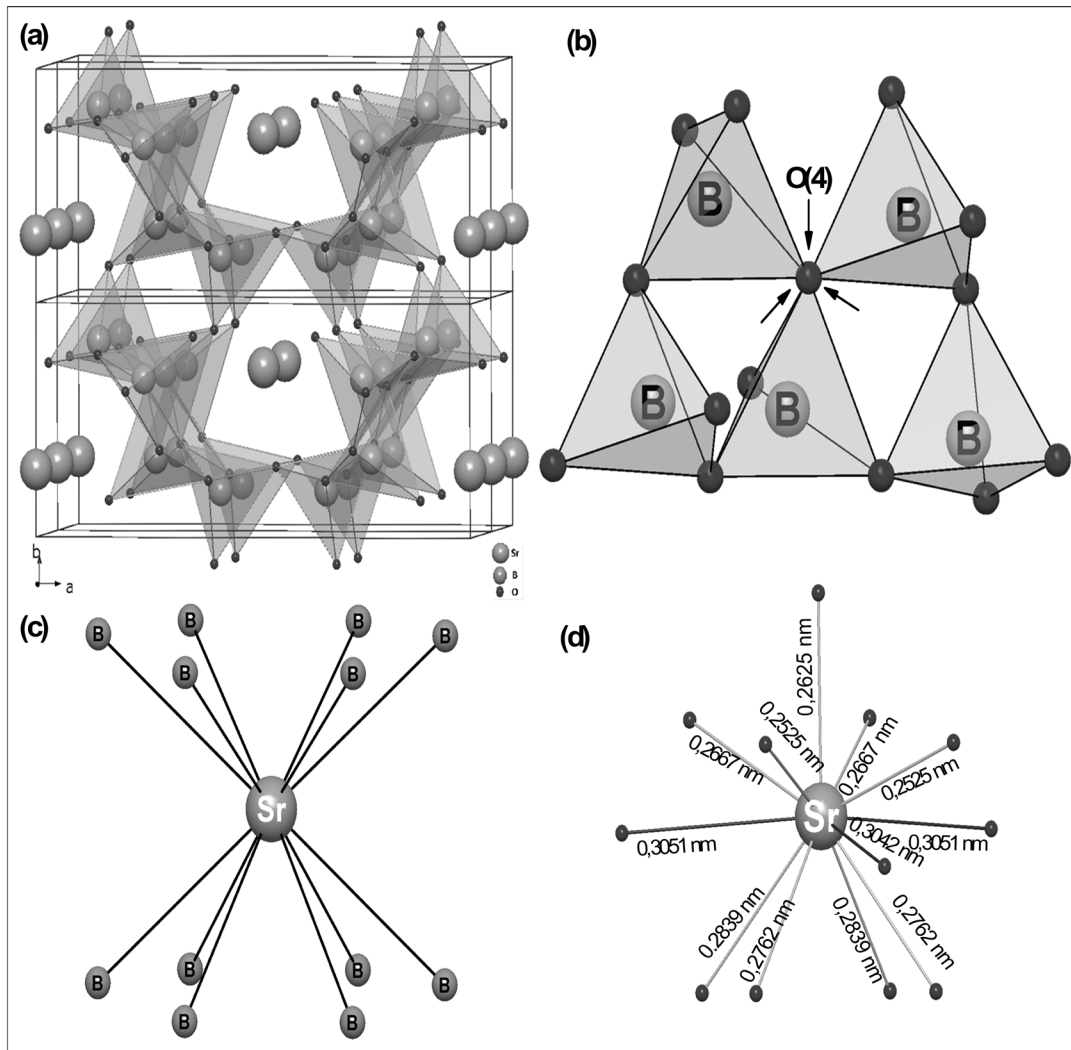
Figure 4.1 (a) Unit cell of SrB_4O_7 along the c – axis; (b) Arrangement of boron tetrahedral around triply coordinated oxygen; (c) Boron circle coordination around Sr ion; (d) Local coordination geometry environment of Sr^{2+} sites.

The size of the divalent lanthanide dopants is much more suitable than the size of these ions in the trivalent state for a substitution of Sr^{2+}. From what is known, it is thought that the lattice of SrB_4O_7 does not provide an evident charge compensation mechanism, which is necessary for a substantial substitution of Sr^{2+} by trivalent lanthanide ions [93].
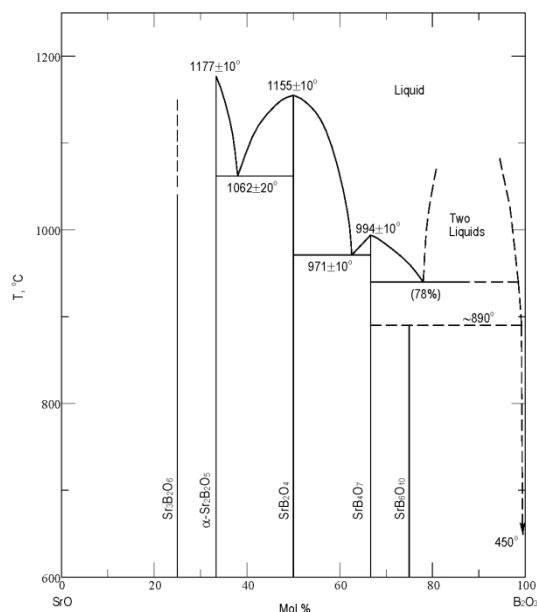
Figure 4.2 SrO-B₂O₃ phase diagram [91]

4.2. Crystal Structure of La(Gd)MgB$_5$O$_{10}$

As proposed by Saubat *et al.* [94] lanthanide (Ln) magnesium meta borates (LnMgB$_5$O$_{10}$) possess interesting features like one dimensional Ln-Ln chains, where intrachain interaction dominate interchain one. The lanthanide magnesium meta borates corresponding to the formula LnMgB$_5$O$_{10}$ can be obtained as an isomorphic series from lanthanum to erbium [94]. According to single crystal X-ray diffraction studies [94, 95] the LnMgB$_5$O$_{10}$ crystallize in the monoclinic crystal system (Z = 4), space group P12$_1$/c1 (14). *Figure 4.3* shows a structure fragment of LaMgB$_5$O$_{10}$. The structure of LnMgB$_5$O$_{10}$ can be easily described as a set of parallel (B$_5$O$_{10}$)$^{5-}$$_n$ layers composed of three BO$_4$ tetrahedra and two BO$_3$ triangles sharing corners. BO$_3$ planar triangles play bridging roles between BO$_4$ tetrahedra. The three boron atoms are found in a tetrahedral coordination, while only two have triangular surroundings. The existence of BO$_3$ and BO$_4$ borate groups in the structure is also supported by infrared spectroscopy [95]. The bonding between boron and oxygen is strongly covalent in the anionic complex species and it has been concluded that the bonding between lanthanide and oxygen should be predominantly of ionic character [96]. Six-fold coordinated magnesium and 10-fold coordinated

lanthanide ions connect anionic sheets parallel to 102 plane direction. Average Ln-O distance is 2.611 Å (shortest – 2.3979 Å, longest – 2.9610 Å) for lanthanum [94] and 2.529 Å (shortest – 2.2994 Å, longest – 2.9260 Å) for gadolinium compounds [95]. Lanthanide ions have only one site with symmetry not higher than C_1 [96]. The Ln atom has 10-fold coordination with eight normal distances, one shorter and one longer distance. It is surrounded by three boron triangles and three boron tetrahedra with which the Ln atom shares either edges or corners, as shown in *Figure 4.3a*. The $(LnO_{10})^{17-}$ polyhedra form zigzag chains along the b axis, where the intrachain Ln-Ln distances are 3.9940 Å for La (3.9583 Å for Gd) whereas the corresponding interchain distances are noticeably longer, i.e. 6.4340 Å and 6.2633 Å for La and Gd, respectively (*Figure 4.3c* and *d*). These distances conclude that Ln-Ln interactions in this type of structure exist substantially inside the chain. Similarly, the Mg atom has six-fold coordination with four normal and two slightly longer distances, and two neighboring Mg atoms form a sort of dimmer, sharing the two oxygen atoms O(2).
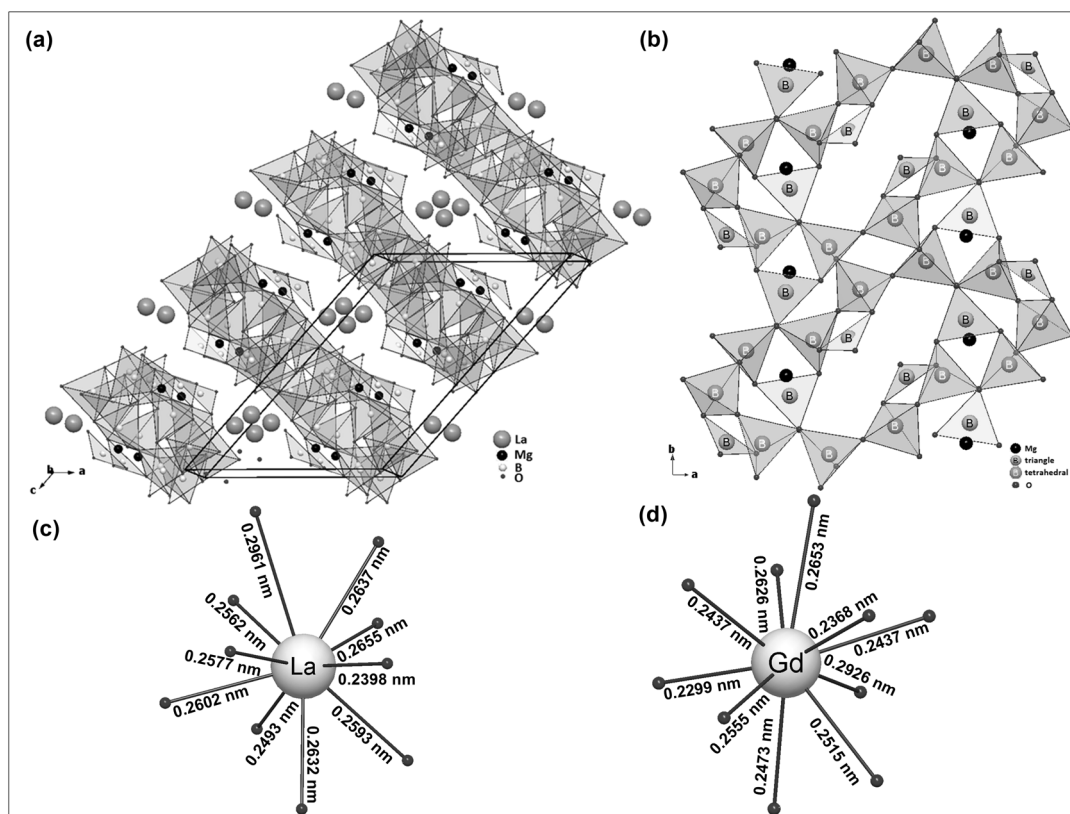
Figure 4.3 (a) Fragment of LaMgB$_5$O$_{10}$ structure along the b – axis (unit cell is indicated); (b) Arrangement of boron tetrahedral and triangles along the c – axis; (c) Local coordination geometry to oxygen of La^{3+} sites; (d) Local coordination geometry to oxygen of Gd^{3+} sites.
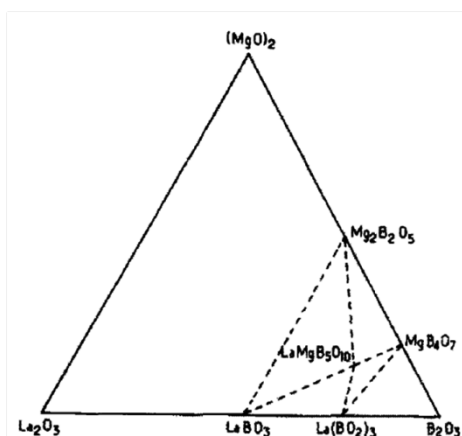
Figure 4.4 Phase diagram for the boron-rich part of the La$_2$O$_3$-(MgO)$_2$-B$_2$0$_3$ system.

A portion of the La$_2$O$_3$-MgO-B$_2$O$_3$ diagram is shown in *Figure 4.4*. Attempts to prepare LnMgB$_5$O$_{10}$ phase with smaller lanthanides by modifying the preparation temperature were unsuccessful. Melting points for some LnMgB$_5$O$_{10}$ phases are: La – 1110, Nd – 1075, Eu – 1055, Er – 1020 °C. The

variation of melting points indicates a decrease in the stability of the structure when the lanthanide ion shrinks [94].

4.3. Crystal Structure of $Sr_4Al_{14}O_{25}$

The crystal structure of $Sr_4Al_{14}O_{25}$ ($4SrO \cdot 7Al_2O_3$ or S4A7) is orthorhombic with space group *Pmma* (51). $Sr_4Al_{14}O_{25}$ consists of layers made up of AlO_6-octahedra separated by a double layer of AlO_4-tetrahedra. The octahedra are connected together by sharing one edge, whereas the tetrahedra are connected by corner sharing, two by two or three by three, resulting in the presence of tricoordinated oxygen atoms and tetrahedra triclusters (*Figure 4.5a*) such as in $CaAl_4O_7$ [97], $SrAl4O7$ [98] and mullite [99]. There are six different crystallographic sites for the aluminum atoms in the structure: three AlO_6 octahedral sites and three AlO_4 tetrahedral sites. According to the structural data, two different strontium sites with coordination numbers 10 and 7 exist in the $Sr_4Al_{14}O_{25}$. The Sr1 site lies in the complicated oxygen-polyhedron with average Sr-O distances ≈ 0.284 nm (*Figure 4.5b*), while for the Sr2 site distances are shorter (≈ 0.258 nm) (*Figure 4.5c*) [100, 101]. Because the radius of Sm^{2+} (CN = 7 → 0.122 nm; CN = 10 → 0.137 nm) is very similar to that of Sr^{2+} (CN = 7 → 0.121 nm; CN = 10 → 0.136 nm), it is assumed that Sm^{2+} replace Sr^{2+}. Considering Sm^{2+} affinity to occupy high CN sites, it can be predicted that Sm^{2+} remains mainly in Sr1 sites (CN = 10). Nevertheless, two types of Sm^{2+} ions in the $Sr_4Al_{14}O_{25}$ crystals could be expected. Moreover, the interactions between oxygen and strontium ions at the 10-fold coordinated site are weaker than at 7-fold coordinated site. One can assume that the covalence and crystal field effects are stronger for 7-fold coordinated site than for the 10-fold site.
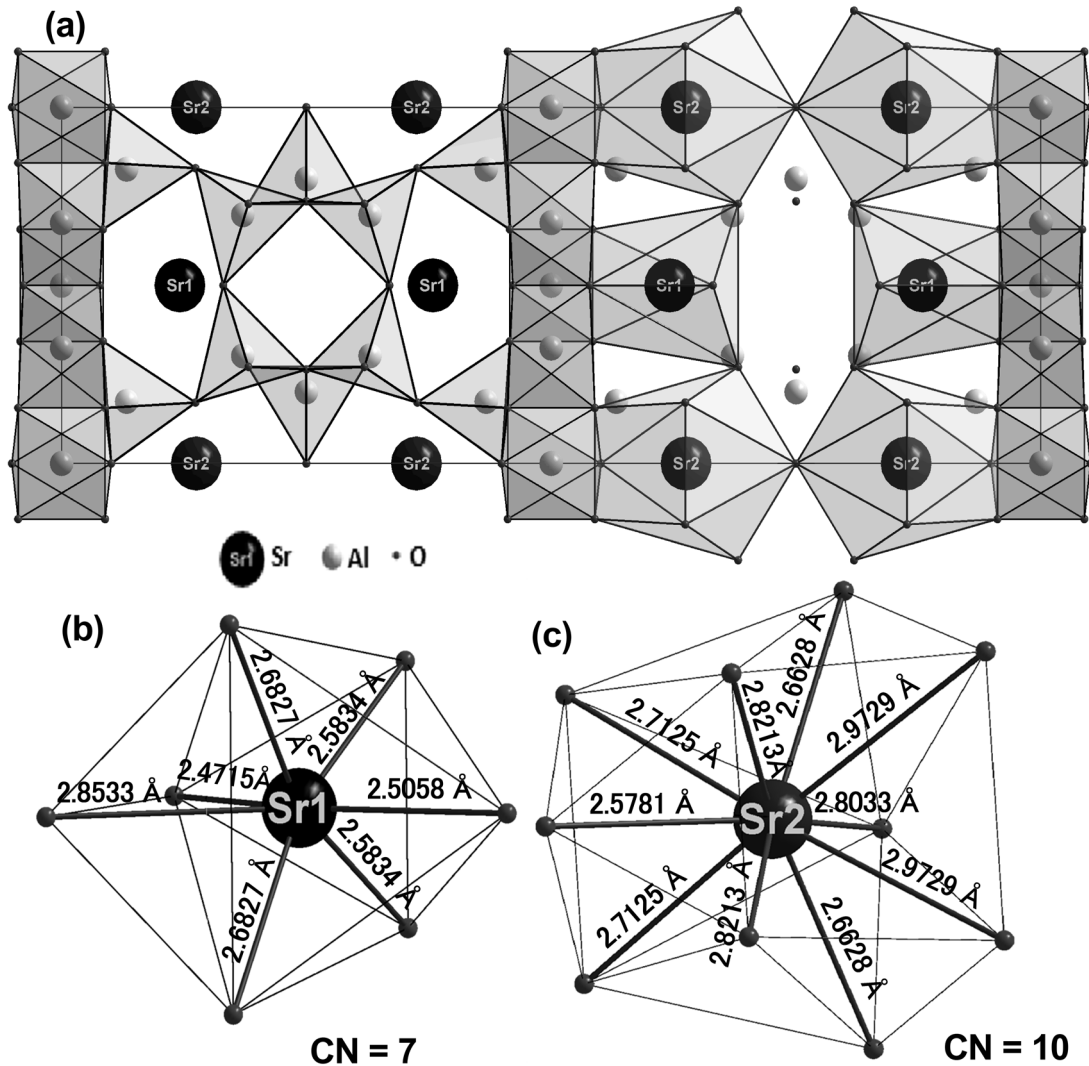
Figure 4.5 (a) Unit cell of $Sr_4Al_{14}O_{25}$ along the c – axis and local coordination geometry environment of nonequivalent Sr^{2+} sites: (b) CN = 7; (c) CN = 10.

Despite large similarities with their calcium counterparts, strontium aluminates have received less attention and many uncertainties concerning the phase diagram still remain [102, 103]. When identifying the crystalline phases present during the synthesis of strontium aluminate, via solid-state method using aluminum hydroxide and strontium carbonate, a secondary phase, referred to as strontium aluminum oxide hydroxide ($SrAl_3O_5(OH)$), was always present. In fact, this compound was $Sr_4Al_{14}O_{25}$ (S4A7), not reported in the phase diagram. It was identified by Wang *et al.* [104, 105], who synthesized it by solid-state reaction at 1300°C. They found that this compound was identical to the sample processed by hydrothermal synthesis [106]. The formation and

crystallization of S4A7 from amorphous precursor is confirmed and studied by differential scanning calorimetry (DSC), X-ray diffraction (XRD) and ^{27}Al nuclear magnetic resonance (NMR) spectroscopy [107]. $Sr_4Al_{14}O_{25}$ was formed through two exothermic peaks. The first one, at 923 °C, corresponded to the crystallization of two metastable solid solutions, γ-Al_2O_3 and hexagonal strontium monoaluminate $SrAl_2O_4$ (SA). The second one, at 1134 °C, induced the reaction between these two metastable phases to yield pure S4A7. This compound was stable up to 1500 °C; after holding at this temperature for 15 h no sign of decomposition was noted. At higher temperatures it decomposed into mono-aluminate (SA) and di-aluminate $SrAl_4O_7$ (SA2), the latter decomposes into SA and $SrAl_{12}O_{19}$ (SA6). Studies have shown that $SrAl_4O_7$ and $Sr_4Al_{14}O_{25}$, having close compositions, should not coexist. Their respective domains of stability exclude each other [108].

In *Figure 4.6(left)* is proposed a modification of a part of the SrO-Al_2O_3 phase diagram after Massazza [1] (*Figure 4.6(right)*). It introduces S4A7 with its domain of stability, closely related to that of SA2. Because of its low kinetics of formation, SA2 may crystallize at 900 – 1000 °C, either directly or via hexagonal SA and γ-Al_2O_3 metastable solid solutions. As the temperature is raised (>1100 °C), SA2 becomes metastable, and only S4A7 will crystallize. This compound is stable up to 1500 °C. At higher temperature, S4A7 decomposes into SA and SA2. The latter compound, being unstable at elevated temperature, also decomposes into SA and SA6. At higher temperature, there is again a narrow stability domain for SA2, close to its melting point. On cooling from the liquid state, if the solidification occurs in that high-temperature stability domain only SA2 will crystallize, while by too rapid quenching, at least a part of the solidification will occur out of this stability domain and it will result in a mixture of phases. The symmetrical behaviors for crystallization from amorphous precursors at low temperature and from liquid at very high temperature should be noted. Low heating or cooling rates produce pure SA2 while too rapid kinetics results in mixtures of phases.
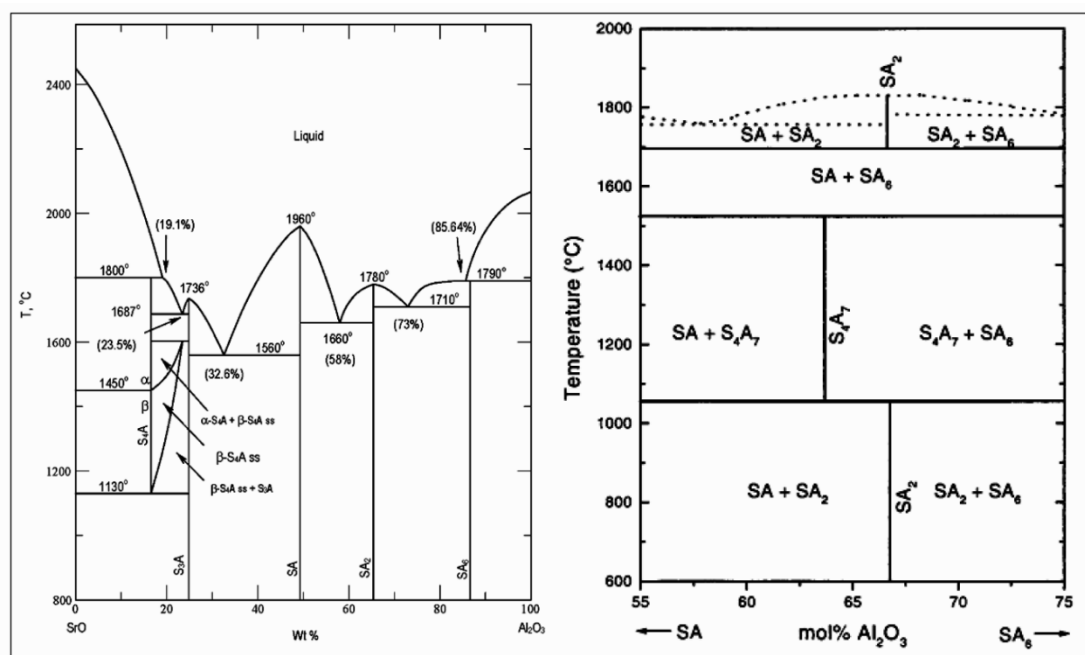
Figure 4.6 SrO-Al$_2$O$_3$ phase diagram (left) and modification of a part of the SrO-Al$_2$O$_3$ phase diagram (right) showing the closely related domains of stability of SA2 and S4A7. Pure SA2 may be obtained by slow crystallization of an amorphous precursor at 900 – 1000 °C or by slow cooling from the liquid state.

Chang et al. investigated boron oxide influence on Sr$_4$Al$_{14}$O$_{25}$ phase formation. TEM images showed that the grain sizes of the both samples, with and without boron oxide, are similar. However B$_2$O$_3$ aided ceramics were fully densified at 1400 °C, while micropores were observed in the microstructure of the ceramics without B$_2$O$_3$ addition. The introduction of B$_2$O$_3$ can form liquid phase at a relatively low temperature. This liquid phase can greatly promote the phase formation and reduces the sintering temperature. With the help of B$_2$O$_3$, single phase Sr$_4$Al$_{14}$O$_{25}$ ceramics were obtained at 1400 °C, while higher temperature is required in the case of ceramics without B$_2$O$_3$ addition. Furthermore, TEM observations indicated another important role of B$_2$O$_3$ of removing the micropores on the grain boundary during the sintering process.

Moreover, there are reports that boron reacts with aluminate and replaces aluminum in the structure. The obtained data showed the presence of substituted BO$_4$ units in strontium aluminates, which retained even after acetic acid washings. BO$_4$ participates in the formation of superstructural units by breaking of O–Al–O and form Al–O–B bonds. B$_2$O$_3$ starts reacting with

49

$SrAl_2O_4$ and facilitate conversion to $Sr_4Al_{14}O_{25}$. Therefore, it can be concluded that B_2O_3 does not act as an inert high temperature solvent medium (flux); it actively participates in reactions and depending upon B_2O_3 concentration, different phases are stabilized of which evidence are the formation of the compounds $SrAl_2O_4$, $Sr_4Al_{14}O_{25}$ and $SrAl_{12}O_{19}$. The final product is dependent on the $SrO/Al_2O_3/B_2O_3$ ratio [109].

4.4. Crystal Structure of $SrAl_{12}O_{19}$ and $LaMgAl_{11}O_{19}$

Hexaaluminates with the magnetoplumbite crystal structure have been receiving considerable attention, because of their diverse applications, in particular, as luminescent and laser host materials.

β-Alumina and magnetoplumbite structures resemble each other. They consist of spinel blocks separated by intermediate layers containing large cations. The main differences between the two exist in the intermediate layer (mirror plane). In the magnetoplumbite structure, the intermediate layer of a single unit cell contains a large cation, an Al ion, and three oxygen ions (*Figure 4.7*); in the β-alumina structure, it contains only a large cation and an oxygen ion. The differences in composition of the intermediate layer result in different overall compositions of β-alumina and magnetoplumbite. The latter has the overall formula $AB_{12}O_{19}$ and β-alumina has the overall formula $CB_{11}O_{19}$ with B = Fe^{3+}, Ga^{3+}, or Al^{3+}. In general A is a large divalent metal ion and C is a large monovalent metal ion with respect to the size of the B ions. It is also possible that A is a large trivalent ion and C is a large divalent ion, resulting in defect type structures.

Dimensional relations between the sizes of A and B ions have to be considered. The larger the ions in the B-sites, the larger must be the ions in the A-sites. In aluminates (B = Al^{3+}, r = 0.0535 nm [110]) the magnetoplumbite type structure appears when A = Ca^{2+}, Sm^{2+}, Eu^{2+}, Sr^{2+} and Pb^{2+} [111]. These dimensional relations are related to the c/a ratio of the unit-cell: the size of the c-axis depends strongly on the size of the A ion and the size of the a-axis depends mainly on the size of the B ion. For the magnetoplumbite type

structure the c/a ratio must be in the range of 3.91 (ideal structure) to 3.97 (strongly distorted structure) [111].

The composition for an ideal magnetoplumbite phase based on alumina is $MAl_{12}O_{19}$ (where M is typically an alkaline earth such as Sr or Ca) which has a hexagonal structure, with space group $P6_3/mmc$ (194). The unit cell parameters are: a = 0.56581, b = 0.56581, c = 2.16676 nm, α = 90, β = 90, γ = 120° [112]. The unit cell is composed of spinel-structured slabs containing Al^{3+} cations separated by mirror planes, which contain one Sr^{2+} and three oxygen ions per unit cell (*Figure 4.7*).
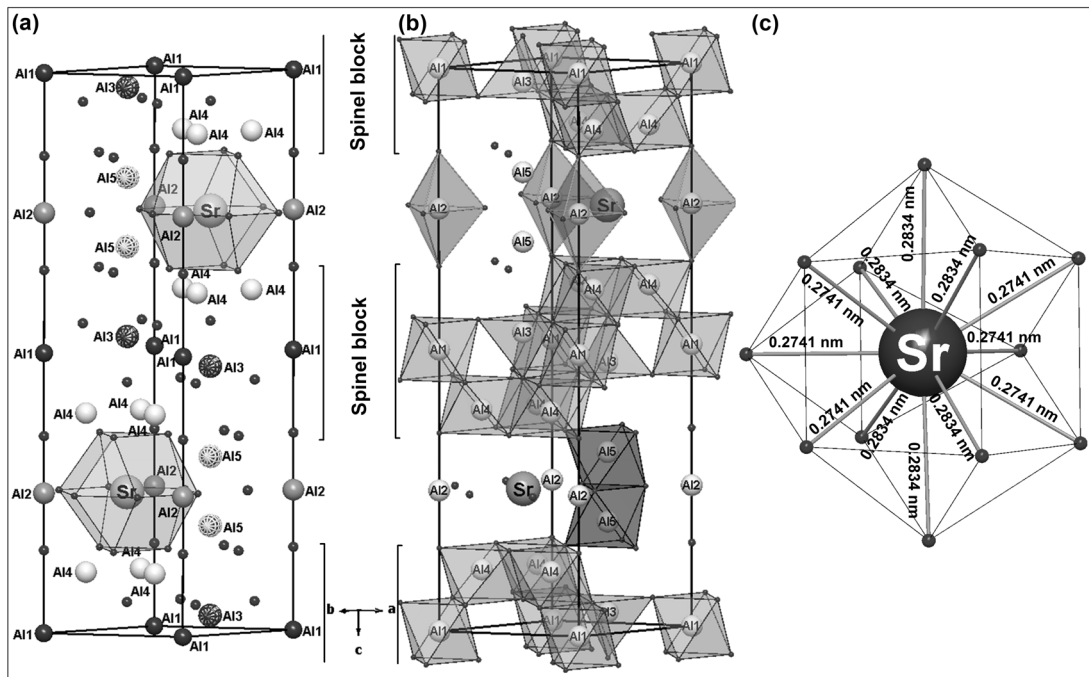
Figure 4.7 (a) Nomenclature of the atomic positions in magnetoplumbite structure, (b) coordination polyhedra of aluminum in the structure, (c) Sr^{2+} coordination polyhedron.

It has been found that alumina-based magnetoplumbites exhibit a nonstoichiometry which origin obviously lies in the defect structure of the material. The large divalent cation can be replaced completely by a trivalent cation such as La^{3+} or other rare-earth species with compensation by a different cation such as Mg^{2+} substitution for Al^{3+} in the spinel blocks. Due to the complexity of the basic crystal structure, however, the knowledge of the intrinsic defect structures available from experiment is quite limited. For instance, the distribution of Mg or other small cations over the possible Al sites

has not been determined conclusively; in fact several different schemes have been proposed [20].

The magnetoplumbite-structured $SrAl_{12}O_{19}$ may be expected to accommodate diverse luminescence properties because of the variety of crystallographic sites within the unit cell. The structure is composed of spinel blocks, which have the usual 4 and 6 coordinated sites for cations, whereas the interspinel layers have rather unusual 5-fold sites for small cations. The interspinel layers also provide 12-fold sites to accommodate large cations, which may be monovalent, divalent, or trivalent. Charge is balanced either in the interspinel layer (i.e., $Na_{0.5} + La_{0.5}$) or in both the interspinel layer and the spinel block (e.g., La and Mg replacing Sr and Al, respectively).

Chapter 5. Experimental

5.1. Methods of Preparation

In general, almost all phosphors are synthesized by solid-state reaction between raw materials at high temperatures. The high purity materials of host crystals, activator and fluxes are mixed and blended to get homogeneous mixture. Then the mixture is fired at high temperature in a container. The fired product is then crushed, milled and then sorted to remove coarse and excessively crushed particles.

For combustion synthesis method, firstly, metal salts are dissolved in distilled water and heated to $65 - 75$ °C; if necessary additionally HNO_3 is added to prevent hydrolysis of metals. Secondly, under continuous stirring, complexing agents and fuels are added and solutions are stirred for an additional 1h at the same temperature. Subsequently, after concentrating the mixtures by slow evaporation, sols are turning into transparent gels. Then the temperature is raised to ≈ 250 °C the self-maintaining gel combustion process starts, which is accompanied with evolution of huge amount of gases. Finally, the resulting products are dried in the oven for several hours at 120 °C and ground to fine powders, which follow preheating and annealing steps. For annealing under reducing atmosphere, high-temperature tube furnaces with continuous gas flow were used. For mild reduction active carbon was used (CO atmosphere), by placing small crucible with sample into bigger vessel with carbon in it and closing with lid.

5.2. Chemicals

The starting materials were Sm_2O_3 (99.9 % Alfa Aesar), La_2O_3 (99.9 % Treibacher), Gd_2O_3 (99.9 % Treibacher), MgO (99.95 % Alfa Aesar), $SrCO_3$ ($\geq$99.9 % Aldrich), nano-scale Al_2O_3 (Evonik Industries), NH_4Cl ($\geq$99.5 % Alfa-Aesar), AlF_3 (reagent grade, Aldrich), H_3BO_3 ($\geq$99.5 % Merck). For combustion synthesis the gels were prepared using $Sm(NO_3)_3 \cdot 6H_2O$ (99.9 % Aldrich), $Sr(NO_3)_2$ (>99 % Aldrich) and $Al(NO_3)_3 \cdot 9H_2O$ ($\geq$98 % Aldrich).

Tris(hydroxymethyl)-aminomethane (tris-amine) or ethylenediaminetetraacetic acid (EDTA) were used as complexing agent and fuel.

5.3. Materials Characterization

5.3.1. Powder X–ray Diffraction

X-ray diffraction (XRD) uses the pattern produced by the diffraction of X-rays through the lattice of atoms in a material to reveal the nature (symmetric) structure of that lattice, which usually leads to an understanding of the structure of the material. The X-ray photons physically interact with the electrons that surround the atoms. X-rays scattered from a crystalline solid can constructively interfere, producing a diffraction pattern. This technique works because in a crystalline material the inter-atomic distances are of the order of the wavelength of X-ray radiation (10^{-9} m). As a result, X-ray radiation is diffracted by the electron clouds in the crystal structure. This gives diffraction maxima, which are dependent on the type of atoms, their spacing and distribution. The X-ray diffraction technique, therefore, is not a technique that produces images. However, the electron density can be reconstructed using the diffraction pattern, which is obtained from a periodic assembly of units in the crystal. A model can be preliminarily created using obtained data. Then calculated diffractions can be compared with observational data, to finally elaborate an accurate unambiguous 3D physical structure of the material.

Powder X-ray diffraction analysis has been carried out employing a Rigaku MiniFlex II diffractometer working in Bragg–Brentano ($\theta/2\theta$) geometry. The data were collected within 2θ angle from $10°$ to $60°$ at a step of $0.02°$ and integration time of 1 s using Ni-filtered Cu K_α line.

5.3.2. Spectroscopic Investigations

It is a very well known fact, that interaction of electromagnetic radiation with matter causes absorption, emission, and scattering of radiation. As a result of this interaction, it is possible to characterize the optical properties of materials by measuring the properties of electromagnetic radiation. The most

classic experiments in spectroscopy are concerned with the determination of the transition energies of the optical center [113]. So called transition "energies" are commonly expressed in terms of energy (eV), frequency ν (s^{-1}) or ω (rad s^{-1}), wavelength λ (nm), or wavenumbers $\tilde{\upsilon}$ (cm^{-1}). Physical magnitude measured is an intensity of electromagnetic radiation as a function of photon energy. A graph that plots the intensity versus photon energy is called a spectrum, and peaks (or dips) in the spectrum reveals the locations of optical transitions.

Four techniques are commonly used for this kind of experiments: absorption spectroscopy, diffuse reflection spectroscopy, luminescent excitation spectroscopy, and emission spectroscopy. In absorption spectroscopy the photon energy of the radiation incident on the sample is selected by a scanning monochromator. Absorption spectroscopy is used to measure the transmitted signal for transparent (non-scattering) samples such as single crystals or solutions. An alternative for strongly scattering materials, such as polycrystalline powders, is diffuse reflection spectroscopy. The difference in set-ups for absorption and reflection spectroscopy is in the detection compartment. When diffuse reflection spectroscopy is used, the backscattered signal is detected and compared to the back-scattered signal from a reference material. Excitation and emission spectroscopy have very low background levels and a much higher sensitivity. It is used in combination with samples containing very small quantities of luminescent species. Absorption and diffuse reflection spectroscopy have much larger background and noise levels and are used for more concentrated samples.

5.3.3. Room Temperature Spectroscopy

In the case of the excitation spectrum the plot is actually an absorption spectrum which is obtained by monitoring the luminescence at a specific wavelength (at the peak of emission). The excitation spectrum is a replica of the absorption spectrum of the same ion but the position of the energy levels in excitation spectrum is determined by monitoring the intensity of emission, not

by the intensity of radiation passed through the sample as in absorption spectrum. The wavelength of excitation is varied by scanning the excitation monochromator for fixed emission wavelengths. By this means the upper energy levels of the luminescent centres (or ions) are revealed, even when these levels are non-radiatively relaxing on to the lower excitation level involved in radiative emission. Consequently, the excitation spectrum is used to locate the energy levels of the excited states. Depending upon the absorption cross section of the excitation bands the intensity of the emission varies. From the excitation spectrum the region of luminescence can be determined, as also the energy levels of the ions in the host lattice. In the monochromator, white light from a xenon lamp is collected by an elliptical mirror and directed to the entrance slit. Then the light is dispersed through the grating and then is directed to the exit slit of the monochromator (for excitation). A specific wavelength is selected by the monochromator from the incoming light. The entrance and exit ports (or silts) of the spectrometer and the monochromator are adjustable. These are computer controlled slits. To be able to detect the lamp profile of the output beam, a photodiode is used. The slits of the monochromator determine the amount of monochromatic light that is used to illuminate the sample. The spectrometer slits, on the other hand, control the intensity and resolution of the fluorescence signal that is detected by the photomultiplier tube (PMT). Eventually the PMT signals are amplified and processed. By monitoring at different fixed emission wavelengths, complete knowledge can be defined about the upper energy levels involved directly or indirectly in the luminescence process.

For the emission spectrum the luminescent centre or the activator ion in a phosphor that has passed to the excited state returns to the ground state through either radiationless transitions or by way of emission transitions. Emission transition is detected as a glow of the materials and registered in the form of a band in the luminescence spectrum. The position of the band in the luminescence spectrum of the ion does not depend on the method of excitation it is only determined by the inter-level spacing. In the diagram of energy

levels, however, there can be several emission levels, and transitions from each one of them can not only be to the ground state, but also onto the intermediate levels. The ground state can be split into sublevels and then transitions from each emission level will be onto the ground state sublevels. This can result in the appearance of complex luminescence spectra consisting of many bands and are characteristics of trivalent lanthanide ions.

Excitation and photoluminescence spectra were measured at room temperature using an Edinburgh Instruments FSL900 fluorescence spectrometer. This spectrometer consists of a light source (a Xe lamp), slits, a monochromator, sample compartment, reference detector (photo diode), a spectrometer and a signal detector (PMT). The main advantages of using a photomultiplier are that the spectra, which are in this case recorded in *photon counting mode*, can be easily corrected for the technical response function of the setup. In addition, time resolved luminescence spectroscopy is fairly easy realized. Photoluminescence describes the process in which energy is emitted, in form of light, from a material at a different wavelength under excitation of a light source at which is absorbed by the sample.

5.3.4. Specific Issues Concerning FSL900

In the measurements of luminescence spectroscopy with Edinburgh Instruments FSL900, the following issues have to be addressed:

a) Second order diffraction interference of the pump wavelength.

The diffraction relation of a grating is known to be:

$$\mathbf{d}\sin\mathbf{\theta} = \boldsymbol{n\lambda},$$

where $\mathbf{d}$ is the spacing of the adjacent ruled grooves of the grating, $\boldsymbol{n}$ – order of the diffraction and $\mathbf{\theta}$ – angular direction of the diffraction.

When the spectrometer is scanning, the $\sin\mathbf{\theta}$ changes until the required wavelength of the signal is sent to the exit slit. It can be noted, that for the first order case, with wavelength λ, the signal will be overlapped with the second

order of wavelength $\lambda/2$. To avoid this problem a cut-off filter is used between the sample and the entrance slit of the spectrometer.

For example, if it is used 360 nm Xe lamp radiation to pump the sample and attempting to measure the emission in the spectral range of 500 – 900 nm, the second order of the pump light (360 nm) will appear at the wavelength 720 nm. Without a cut-off filter, which is blocking the 360 nm pump light, this light will give a huge peak at 720 nm. This will not only make the scan failed, but also gives the risk of damaging the PMT.

b) Interference of the lamp background.

It is known that all the optical devices inside the instrument can produce strong diffuse scattering of the lamp output. Because the lamp illuminates the internal chamber of the monochromator, the light output is always mixed with the background of the lamp. In other words, sample that has a weak emission will have an emission spectrum mixed with a lamp profile in the background. In order to reduce this interference, a UV band-pass filter can be used. This filter only allows the excitation light with selected pump wavelength to reach the sample and rejects the rest of the lamp background, which interferes with the fluorescence measurement.

c) Normalization of excitation spectrum for lamp profile.

The output of the xenon lamp is obviously a function of the wavelength. Therefore, a normalization of the excitation spectrum needs to be made. The relationship of the measured luminescence intensity of the sample [$\mathbf{I}(\lambda)$], the absorption [$\mathbf{A}(\lambda)$], the spectral response of the monochromator [$\mathbf{M}(\lambda)$] and the pump power of the lamp [$\mathbf{L}(\lambda)$] is given by:

$$\mathbf{I}(\lambda) = \mathbf{M}(\lambda)\, \mathbf{A}(\lambda)\, \mathbf{L}(\lambda).$$

From this relation we can obtain the excitation (absorption) spectrum:

$$\mathbf{A}(\lambda) = \frac{\mathbf{I}(\lambda)}{\left(\mathbf{M}(\lambda)\mathbf{L}(\lambda)\right)} = \mathbf{I}(\lambda) \times correction(\lambda) = \frac{\mathbf{I}(\lambda)}{\mathbf{R_c}},$$

were $I(\lambda)$ is the luminescent intensity measured by the PMT of the spectrometer and R_c – corrected lamp signal detected by the photodiode of the monochromator unit.

d) Correction for Instrumentation spectral response.

The instrument (fluorescence) sensitivity varies with wavelength due to the fact that in the spectrometer unit diffraction efficiency of gratings, refractive indexes of lenses and the spectral response of the PMT – all depend on the wavelength. Therefore, the spectrum measured can be distorted. The wavelength dependence of the instrumentation is called the instrumentation spectral response, and has to be corrected. Mathematically it will be

$$S(\lambda) = E(\lambda)R(\lambda),$$

where S is the measured emission signal, E – real emission spectrum and R – instrumentation spectral response. Then the real emission spectrum of the materials is:

$$E(\lambda) = \frac{S(\lambda)}{R(\lambda)} = S(\lambda)C(\lambda).$$

The correction factor of the spectrometer,

$$C(\lambda) = \frac{1}{R(\lambda)},$$

is pre-measured using a standard light source and is stored in a file called the correction function. Before emission spectra analysis the raw data is corrected by correction file.

The steady state luminescence spectra in the ultra-violet (UV), visible (VIS) and near-infrared region have been recorded on Edinburgh Instruments FSL900 fluorescence spectrometer equipped with 450 W Xe arc lamp, mirror optics for powder samples and cooled (-20 °C) single-photon photomultiplier (Hamamatsu R2658P). The photoluminescence emission spectra were corrected by correction file obtained from tungsten incandescent lamp certified

by NPL (National Physics Laboratory, UK) and excitation spectra were corrected by reference detector. Reflection spectra were recorded on the same model spectrometer equipped with integration sphere (150 mm diameter, $BaSO_4$ coating). The integrating sphere is built in the way that the incoming light ray is reflected equal in every direction so that the light intensity is the same in each point of the sphere. $BaSO_4$ (99 % Sigma-Aldrich) was used as a reflectance standard.

5.3.5. Low Temperature Spectroscopy

For temperature dependent measurements a cryostat "MicrostatN" from Oxford Instruments had been applied to the Edinburgh Instruments FSL900 fluorescence spectrometer. The cryostat cooled with liquid nitrogen. The nitrogen is kept in a reservoir near the cryostat. Quartz window give optical access to the central sample chamber in which nitrogen are continuously pumped under the sample. The sample is mounted on a thermally conducting *cold boat*, which is cooled by the nitrogen. Thermocouple inside the sample chamber measures the internal temperature. To prevent condensation of humidity, the chamber were evacuated with vacuum pump. This setup provides the possibility to cool samples to liquid nitrogen temperature (77 K). Additionally, installed heating elements allows to heat sample above room temperature. Measurements were carried out from 100 to 500 K in 50 K steps.

5.3.6. Lifetime Measurements

Excited states of an atom or ion correspond to a higher energy than the ground state. These excited electrons eventually decay to the ground state. In nature, the majority decay processes can be well described by an exponential function:

$$I(t) = I_0 \cdot \exp\left(\frac{-t}{\tau}\right),$$

where I_0 is the initial fluorescence intensity immediately after the excitation pulse. In practice, the fluorescence decay time (τ) is defined as the time in which the fluorescence intensity decays to 1/e of the intensity immediately

after excitation. Fluorescence decay can be multi-exponential, leading to complex decay curves. In general, an exponential growth or decay process is expressed in mathematical terms as follows:

$$R(t) = A + \sum_{i=1}^{4} B_i \, e^{\frac{-t}{\tau_i}},$$

with pre-exponential factors $\mathbf{B_i}$, the characteristic decay times $\boldsymbol{\tau_i}$ and an additional background $\mathbf{A}$. $\mathbf{R}(t)$ is often called the sample decay model. The characteristic lifetimes $\boldsymbol{\tau_i}$ are the most important decay parameters. They are specific for different decay processes and express the time it takes to decay from the beginning of the decay to a level of about 37 % of the original value. It is a theoretical expression for the response of the sample to an infinitely short excitation. The parameters $\mathbf{B}$ and $\boldsymbol{\tau}$ are extracted from the raw data by a numerical fit starting from the top of the decay curve. The expression above contains four exponential terms. Many measurements contain only one or two terms. On the other hand, samples can theoretically contain many more lifetimes and can even be so complex that a lifetime distribution analysis would be justified. However, practically all real lifetime measurements can be approximated with no more than four exponential terms. Often, careful experimental planning and clean practice can reduce the number of exponential terms. Most radiative decay times, determined in this work, contain only one term, however, some are bi-exponential.

The pre-exponential factors $\mathbf{B_i}$ are values, which include technical (instrumental) parameters and sample parameters. Used in relative terms, they are still valuable sample parameters. In a multi-component system, for instance, the concentration ratio of the individual components can be determined. In absolute terms, the $\mathbf{B_i}$ values are also affected by instrumental parameters like efficiency of the system, geometrical conditions of the sample, intensity of the excitation source, etc. These instrumental parameters can increase or decrease the measured sample signal, which effectively will result in an (simultaneous) increase or decrease of the $\mathbf{B_i}$ values.

The numerical procedure behind the search for the best $\mathbf{B_i}$ and $\boldsymbol{\tau_i}$ is the Marquardt-Levenberg algorithm. This is an iteration procedure which searches for the best $\mathbf{B_i}$ and $\boldsymbol{\tau_i}$ by a controlled and directed minimisation of the "goodness of fit", $\boldsymbol{\chi_g^2}$, which is defined as:

$$\chi_g^2 = \sum_k w_k^2 \, (X_k - F_k)^2,$$

where $\mathbf{X_k}$ – fit result data, $\mathbf{k}$ is the index for the individual data points to be fitted, the sum expands over all these data points, the $\mathbf{w_k}$ are the weighting factors for the individual data points. Using the correct weighting factors for a specific set of raw data is important. The correct type of weighting factors is determined by the type of noise specific to the data and hence is inherited from the method which was used to collect the data. For lifetime data acquired by gated single photon counting (MCS), which obey Poissonian noise statistics, which has the well-defined weighting factor for each data point ($\mathbf{F_k}$) of

$$w_k = {1}\Big/{\sqrt{F_k}}.$$

In this work the "Tail Fit" (Marquardt-Levenberg algorithm) routine was applied, where sample response function X(t) is identical to sample decay model R(t). This routine is only applicable for data are fitted in a region with no further sample signal generation; moreover, the "Tail Fit" procedure eliminates the statistical noise from the raw data.

Lifetimes were measured with an Edinburgh Instruments FL920 lifetime spectrometer (single photon counting) equipped with an Edinburgh Instruments μF900 flash lamp and a Hamamatsu extended red sensitivity photomultiplier tube. Data acquired in gated single photon counting (MCS) mode.

Chapter 6. *Photoluminescence Properties of Sm^{2+} in SrB_4O_7*

6.1. Experimental Details

Samarium-substituted strontium tetraborate (SrB_4O_7, SrTB) samples were synthesized by the traditional solid-state method, which is based on the interaction of boron oxide and strontium (samarium) oxide at high temperature (~900 °C). Initial materials were Sm_2O_3 (99.9% Alfa-Aesar), $SrCO_3$ (≥99.9% Aldrich) and H_3BO_3 (≥99.5% Merck). The 5 wt% excess of boric acid were added due to preferential evaporation of boron oxide. The series of $Sr_{1-x}Sm_xB_4O_7$ samples with x = 0.001, 0.005, 0.010, 0.025, 0.050 and 0.100 were prepared, corresponding to 0.1, 0.5, 1.0, 2.5, 5.0 and 10.0 % of samarium substitution, respectively. The selected amounts of raw materials were thoroughly ground in an agate mortar (acetone was used as medium) and then preheated in a furnace at 600 °C for 2 h in air. Subsequently, the reground powders were repeatedly sintered in three steps ([I], [II] and [III]) for 8 h at 900°C in air, with intermediate grinding. Body color of obtained materials ranged from pale orange (barely visible) to intense red as a function of substituted samarium concentration.

Excitation (excitation slit 0.2 nm and emission slit 2.0 nm) and emission (excitation slit 5.0 nm and emission slit 0.2 nm) spectra were recorded in the ranges of 250 – 640 and 500 – 900 nm (step 0.25 nm, dwell 0.20 s), measurements were repeated once.

6.2. Data analysis and Discussion

Figure 6.1 present the XRD patterns of 0.1 % samarium substituted strontium tetraborate phase evolution against the annealing steps. After the first heating at 900 °C for 8h in air (*Figure 6.1a*) the blend of three different strontium borates appears. The major phase is orthorhombic SrB_4O_7 (ICDD#04-006-8398) and two minor phases, orthorhombic SrB_2O_4 (ICDD#04-010-0838) and SrB_6O_{10} are indentified. For latter one there is no assigned file number and this record stands under asterisk doubtful. Nevertheless, this is only one reasonable assignment for examined pattern. After second annealing

at 900 °C for 8h (*Figure 6.1b*) the same impurity phases are still detected with substantially lower peak intensity. The third annealing under the same conditions brings the pure strontium tetraborate phase (*Figure 6.1c*). It is worth to mention that impurity phases still remain after direct annealing for 20 h at 900 °C of preheated SrTB mixture. This leads to the conclusion that intermediate grinding facilitates SrTB formation. Influence of samarium concentration on $Sr_{1-x}Sm_xB_4O_7$ phase purity is shown in *Figure 6.2*. Replacement of up to 2.5 % of Sr by Sm has no detectable influence (*Figure 6.2a*) on strontium tetraborate phase purity. However, 5.0 % substitution leads to the sample with small fraction of additional phase (*Figure 6.2b*) of monoclinic SmB_3O_6 (ICDD#04-010-0838). Consequently, the increase of samarium concentration to 10.0 % results in the blend (*Figure 6.2c*) of substituted SrTB and SmB_3O_6.
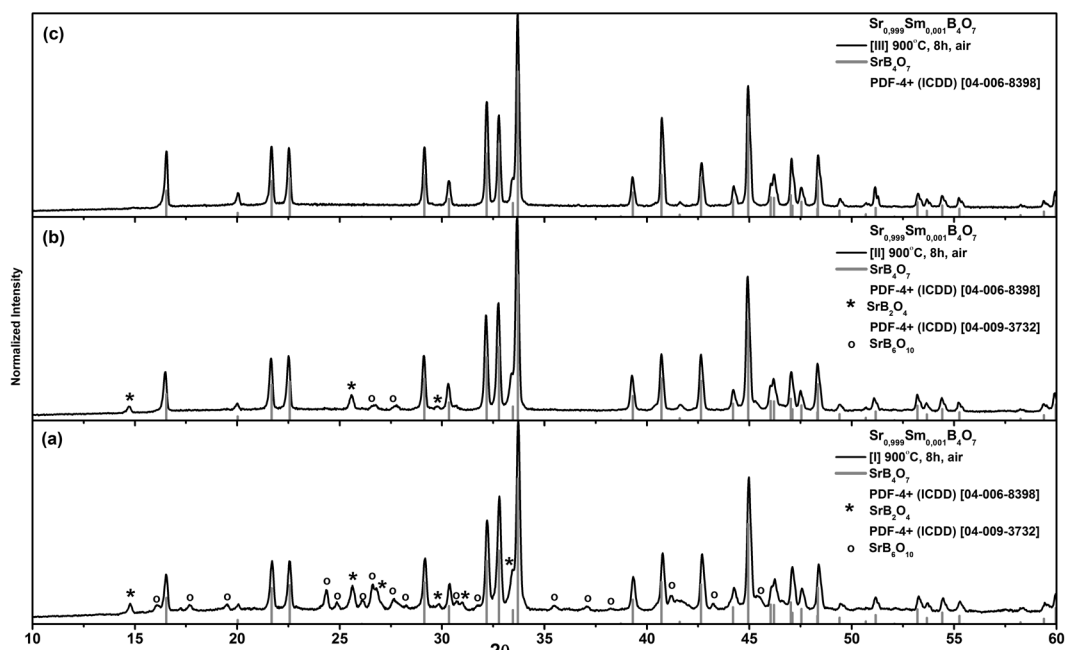

Figure 6.1 XRD patterns of $Sr_{0.999}Sm_{0.001}B_4O_7$ prepared by solid-state method and repeatedly annealed at 900 °C for 8h in air: (a) [I], (b) [II], (c) [III].
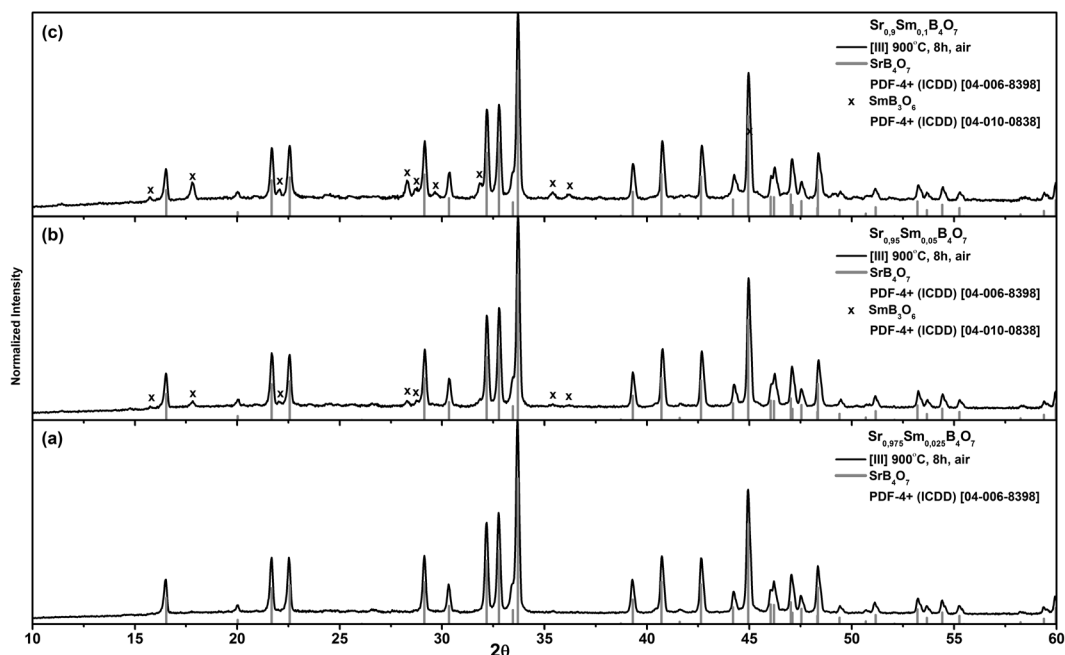
Figure 6.2 XRD patterns of the samples annealed for the third time [III] at 900 °C for 8h in air: (a) Sr$_{0.975}$Sm$_{0.025}$B$_4$O$_7$, (b) Sr$_{0.95}$Sm$_{0.05}$B$_4$O$_7$, (c) Sr$_{0.9}$Sm$_{0.1}$B$_4$O$_7$.

6.3. Influence of Samarium Concentration on Luminescence Properties

Luminescence data for Sr$_{1-x}$Sm$_x$B$_4$O$_7$ samples with x = 0.001, 0.010 and 0.100 (for clarity only emission for 0.100 is given) recorded at room temperature are shown in *Figure 6.3*. Emission spectra contain groups of intense narrow lines in the range from 680 to 830 nm, which are attributed to intraconfigurational $^5D_0 \rightarrow {}^7F_J$ transitions (*J* = 0, 1, 2, 3 and 4) arising from Sm^{2+} ion. The emission spectra are dominated by the single $^5D_0 \rightarrow {}^7F_0$ transition at 685.5 nm (14588 cm^{-1}) pointing to the single site occupation without inversion symmetry. Set of peaks situated at 695.3, 698.8, 704.8 nm (14383, 14311 and 14189 cm^{-1}) are assigned to $^5D_0 \rightarrow {}^7F_1$ transition. Three peaks demonstrate the completely lifted degeneracy of the $^7F_1$ energy meaning that the Sm^{2+} ions are located in sites with C$_{2v}$ or lower symmetry [18]. Next four peaks at 722.0, 724.0, 727.0 and 733.5 nm (13850, 13812, 13755 and 13633 cm^{-1}) belong to $^5D_0 \rightarrow {}^7F_2$ transition. To determine precisely the site symmetry, measurements at lower temperature and better resolution are necessary since there might be additional unresolved peak in vicinity of the

65

four detected peaks attributed to the $^7F_2$ state. Due to low intensity, next sets of spectral features are difficult to resolve unambiguously. Nevertheless, peaks at 761.5 and 766.5 nm (13128 and 13046 cm^{-1}) are assigned to $^5D_0 \rightarrow {}^7F_3$ transition and 802.3, 811.0, 813.8, 817.3 and 820.8 nm (12465, 12330, 12289, 12236 and 12184 cm^{-1}) to $^5D_0 \rightarrow {}^7F_4$ transition.
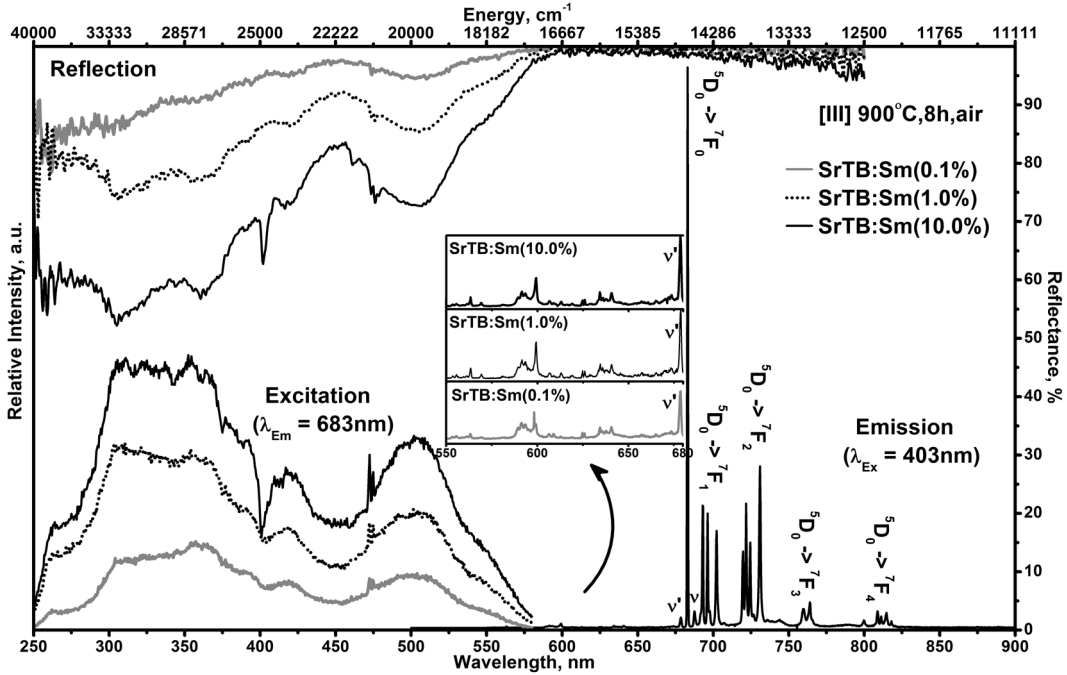

Figure 6.3 Room-temperature excitation, emission and diffuse reflection spectra of $Sr_{1-x}Sm_xB_4O_7$ (x = 0.001, 0.010 and 0.100) samples annealed at [III] 900 °C for 8 h in air (for clarity only emission for 0.100 is plotted). In inset part of enlarged emission (550 – 680 nm) spectra is given.

Measurements of samples with different Sm^{2+} concentration revealed a strictly linear dependence of the emission intensity on concentration, even up to the highest doping levels. No saturation effects could be found. Moreover, the line shape, too, did not show any dependence on the Sm^{2+} concentration. The line shape in emission spectra for all samples was narrower and more expressed at lower temperatures. An average decrease in full width at half maximum (FWHM) for all peaks were 10 – 15 cm^{-1}, except zero phonon line ($^5D_0 \rightarrow {}^7F_0$) where no broadening detected. No peak shifts were detected even at highly substituted samples probably due to insufficient measurement resolution.

The weak peaks at the sides of $^5D_0 \rightarrow {}^7F_0$ transition (*Figure 6.3*), 680.8 and 690.0 nm (14690 and 14493 cm^{-1}), are ascribed to the vibronic emission transitions, denoted as υ and υ', respectively. The energy displacement with the zero-phonon line $^5D_0 \rightarrow {}^7F_0$ is about 98 cm^{-1}. With higher temperatures intensity of those two lines increase indicating that it is a vibronic (electron-phonon coupled) transition (*Inset (II)* in *Figure 6.5*). The vibration involved is probably coupled from low energy Sm-O vibration [114]. The reflection spectra mimic excitation data showing absorption of two broad bands in the range of 550 – 450 and 440 – 350 nm. In the spectrum with the highest substitution level, the Sm^{3+} absorption line at 403 nm is clearly visible. Reflection represents linear relationship between Sm^{2+} concentration and increase of samples body color intensity. In the low energy part of the excitation spectra (17200 – 21700 cm^{-1}) the band with shoulder could be distinguished, the main peak is designated as the SmB band and the satellite as the SmA band [115]. The SmA band should be regarded as the first f-d transition with the weak intensity attributed to the forbidden nature of the transition. Inset in *Figure 6.3* provides zoomed part of emission spectra between 550-680 nm, where residual Sm^{3+} emission ($^4G_{5/2} \rightarrow {}^6H_{5/2}$, $^6H_{7/2}$ and $^6H_{9/2}$) is visible. Despite the best suitable excitation wavelength for trivalent samarium ($\lambda_{Ex} = 403$ nm) used; only traces of Sm^{3+} emission were detected. Ratio of Sm^{3+} emission intensity and υ' vibronic line (*Figure 6.3(inset)*) remains the same for whole series of samples. This observation suggests the efficient Sm^{3+} emission quenching, because excitation and reflection spectra clearly indicates presence of trivalent samarium in the investigated samples (absorption at 403 nm). Presence of Sm^{3+} absorption line for highly doped SrTB is also justified by phase purity (*Figure 6.2c*).

6.4. Luminescence and its Temperature Effects on Sm^{2+}

Temperature dependent excitation spectra of Sr$_{0.99}$Sm$_{0.01}$B$_4$O$_7$ are shown in *Figure 6.4*, data were collected monitoring the emission intensity of $^5D_0 \rightarrow {}^7F_0$ transition (685.0 nm). Generally, spectra of Sm^{2+} systems display broad

bands in spectral range of 250 – 550 nm corresponding to the interconfigurational $4f^6 \rightarrow 4f^5 5d^1$ transition, presenting two split components peaking at around 330 and 500 nm. To describe spectra qualitatively a superposition of the multiplet structure of the $4f^5$ core and the $5d^1$ crystal-field levels may be applied. 5d levels, in low symmetry site, can split into maximum five components which can couple with $4f^5(^6H_J)$ and $4f^5(^6F_J)$ core electron substates. More exact assignment could be overwhelming due to broad and unresolved distribution of transitions, even measured at 100 K. However, several sharp features are also present in the vicinity of the broad f-d band at lower energy part of SmB band (18957 – 19056 cm^{-1}) and at higher energy (21008 – 21108 cm^{-1}) side. Part of this structure remains clearly visible even at higher temperature indicating its f-f origin. It is derived from excited state of $^5D_2$ and $^5D_3$ levels, respectively. These levels are allowed to interact with $4f^5 5d^1$ states having the same symmetry. In case of strong interference effect, however, only the 5d levels terminating the electric dipole transitions from the ground state should be considered [37].

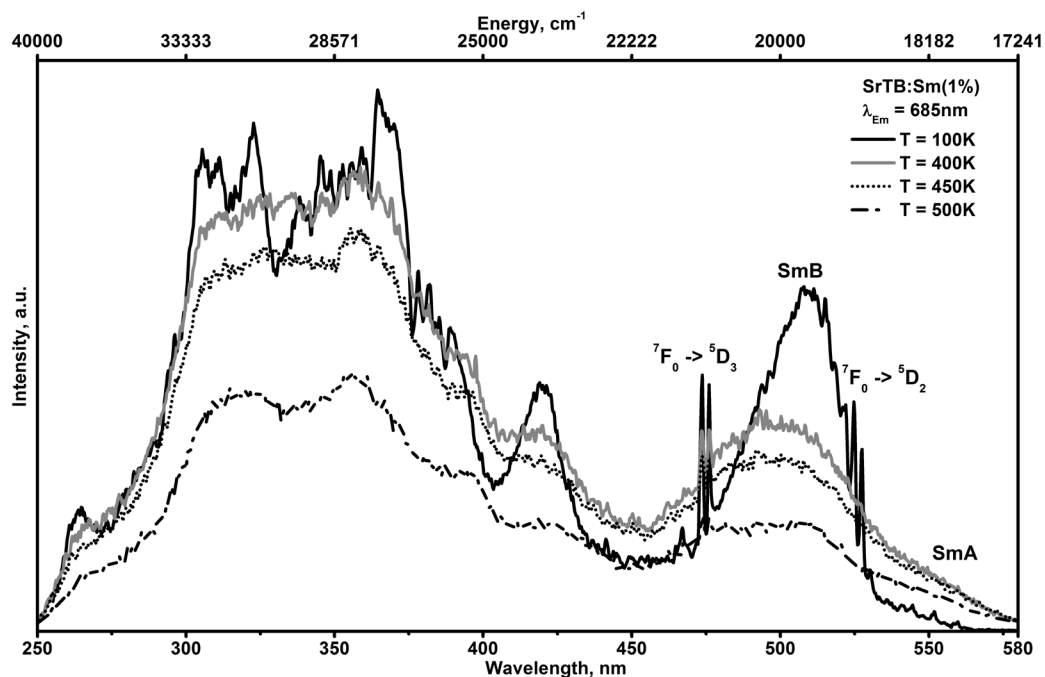

Figure 6.4 Temperature dependent excitation data for $Sr_{0.99}Sm_{0.01}B_4O_7$ sample annealed at [III] 900 °C for 8 h in air, monitored at $\lambda_{Em} = 685.0$ nm (for clarity plots for 150 – 350 K are omitted).

Temperature dependent emission spectra of $Sr_{0.99}Sm_{0.01}B_4O_7$ are shown in *Figure 6.5* (λ_{Ex} = 360 nm). It is necessary to mention that shape and peak intensity distribution is alike in all the samples. There are no trends attributed to change of samarium concentration. *Inset (I)* in *Figure 6.5* presents part of enlarged spectra which exhibit broad d-f band and narrow lines arising from $^5D_1 \rightarrow ^7F_J$ transitions in spectral range 520 – 675 nm. When measuring temperature reaches 400 K above mentioned spectral features appears and increases in intensity as function of temperature. This result is a consequence of the small energy gap between $^5D_0$ and $^5D_1$ excited states ($\Delta E \approx 1300$ cm^{-1}), which is very close to vibration mode of BO_4 (≈ 1300 cm^{-1}). ΔE between lowest d state and $^5D_0$ is approximately 2600 cm^{-1}. Thus observed emission can be explained by a thermal population of excited states from $^5D_0$ level.
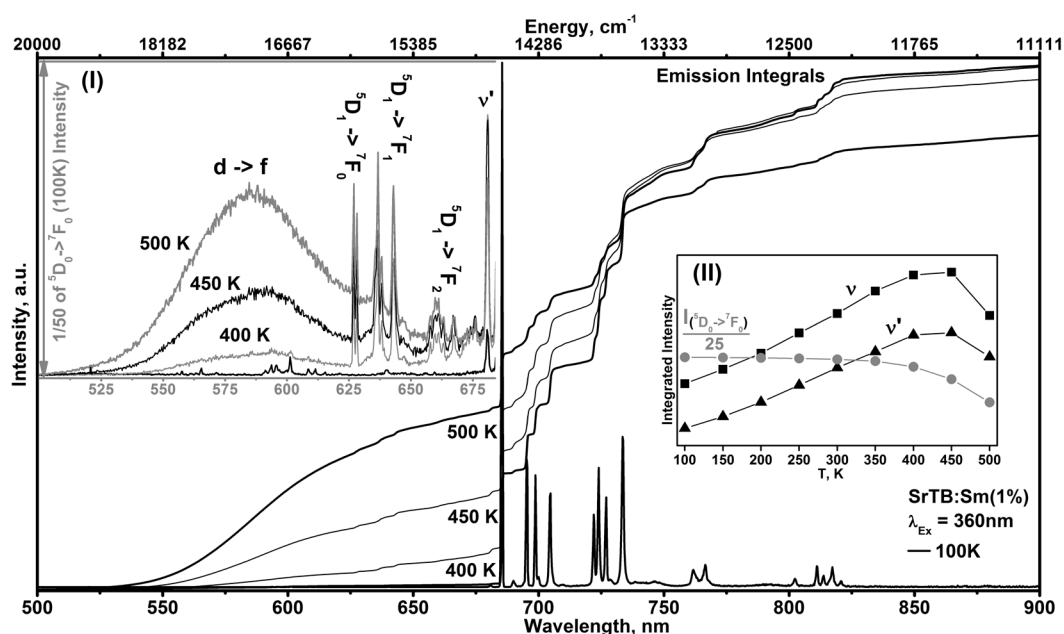
Figure 6.5 Temperature dependent emission data (λ_{Ex} = 360 nm) for $Sr_{0.99}Sm_{0.01}B_4O_7$ sample annealed at [III] 900 °C for 8 h in air (for clarity only emission at 100 K are given). Inset presents zoomed plots where intensity is selected 1/50 of the highest peak. Additionally representative integrals are also given.

Gaussian fitted emission and excitation spectra of SrTB:Sm(1.0 %) measured at 500 K were used for Stokes shift estimation. Emission data were plotted as emitted energy per constant energy interval [4], i. e. Φ_E vs E. Emitted energy was calculated using equation $\Phi_E = \Phi_\lambda \lambda^2(hc)^{-1}$, where c is velocity of light, h – Planc constant, λ is wavelength and Φ_λ is emitted energy

per constant wavelength interval. Moreover, extrapolation given by Dorenbos [116] was applied due to unresolved shape of SmA band. Above mentioned amendments resulted in Stokes shift of about 1600 cm^{-1} for Sm^{2+} emission in strontium tetraborate.
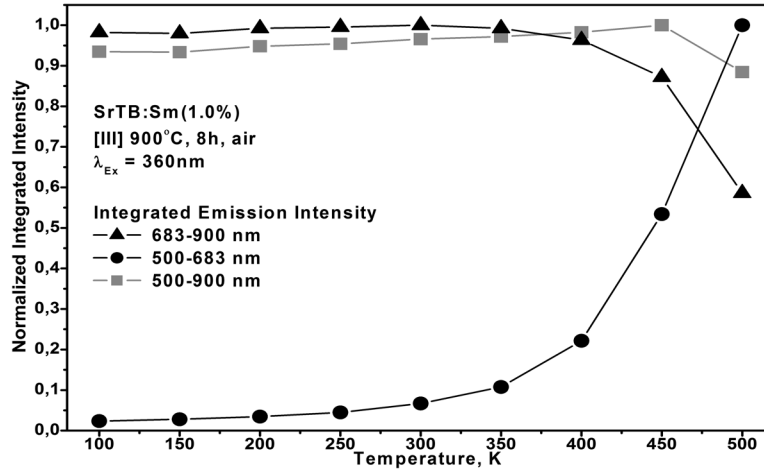
Figure 6.6 Normalized Sr$_{0.99}$Sm$_{0.01}$B$_4$O$_7$ sample emission spectra integrals plotted against temperature. 683 – 900 nm represents $^5D_0 \rightarrow {}^7F_J$; 500 – 683 nm depicts d-f and $^5D_1 \rightarrow {}^7F_J$ integrated transitions.

Figure 6.6 represents normalized integrated values of SrTB:Sm(1.0%) emission spectra, recorded in 100 – 500 K temperature range. Integrated emission interval between 500 – 683 nm depicts the rise of d-f emission with increasing temperature, whereas f-f emission (683 – 900 nm) shows opposite dependency. The f-f emission intensity starts to drop rapidly at 350 K while total emission integral (500 – 900 nm) values are increasing up to 450 K due to thermal population of 4f^{5}5d^1 and ^{5}D$_1$ levels. The temperature dependent emission data for all series of samples are similar and no trends depending on samarium concentration were observed. Boltzmann fit for emission integrals plotted against temperature can be used as rough estimation of thermal quenching temperature. Values obtained in such manner for f-f transitions (683 – 900 nm) for all series of samples fall into 500 – 530 K range, supporting absence of Sm^{2+} concentration influence on emission intensity.

6.5. Time Resolved Spectroscopy of Sm^{2+}

Luminescence decay data of Sm^{2+} substituted strontium tetraborate were recorded monitoring emission of $^5D_0 \rightarrow {}^7F_0$ transition (685.5 nm) and excitation at 360 nm. All these measurements showed a strictly mono-exponential decay of the intensity indicating only one radiative deactivation channel of the emitting $^5D_0$ level. *Figure 6.7* depicts emission decay time dependence of Sm^{2+} concentration against sample temperature (100 – 500 K). Temperature increase up to 500 K results in sharp decay time constant drop, e.g. 4065 → 2082 μs for SrTB(0.1 %) or 3679 → 2001 μs for SrTB(10.0 %). Linear relationship between emission intensity (*Figure 6.6*) leads to conclusion that thermal population of the $4f^5 5d^1$ and $^5D_1$ levels has considerable effect on decay time. However, Sm^{2+} concentration influence is not so straightforward. Decay values reach saturation above 2.5 % strontium substitution. The absence of efficient cross relaxation of Sm^{2+} in SrTB system could be reasonable explanation of observed saturation effect.

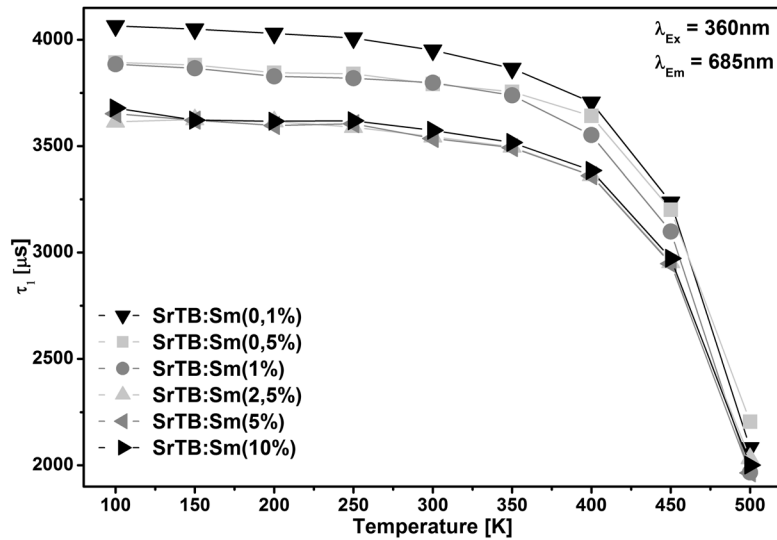*Figure 6.7 Temperature dependent emission decay values of $Sr_{1-x}Sm_xB_4O_7$ samples where x = 0.001, 0.005, 0.010, 0.025, 0.050 and 0.100, monitored at λ_{Em} = 685.0 nm under 360 nm excitation.*

6.6. Review of the Main Results

Samarium substituted $Sr_{1-x}Sm_xB_4O_7$ samples were prepared by solid state synthesis route. The preparation gives Sm^{3+} reduction to divalent state even

after annealing in air at high temperature. Substitution of strontium up to 10 % have no substantial influence on the residual Sm^{3+} emission despite significant amount of SmB_3O_6 phase formation. Moreover, no peak shifts were detected neither against Sm^{2+} concentration or measuring temperature. Due to the thermal population, the $^5D_1 \rightarrow {}^7F_J$ transitions are observed at temperatures higher than 350 K even though the vibration of borate is a high-frequency one. The intensity of $^5D_1 \rightarrow {}^7F_J$ transitions increased with the increasing temperature while the intensity of $^5D_0 \rightarrow {}^7F_J$ transitions decreased. The d-f transitions of Sm^{2+} in SrB_4O_7 appear at high temperature due to the low enough energy position of the $4f^5 5d^1$ level and the small energy difference between $4f^5 5d^1$ and $^5D_0$ levels. The study on the temperature dependence of samarium luminescence in strontium tetraborate shows that the variation of Sm^{2+} fluorescence is most probably governed by the lowest lying $4f^5 5d^1$ states. Obtained Stokes shift for Sm^{2+} d-f emission is ≈ 1600 cm^{-1}. $^5D_0 \rightarrow {}^7F_1$ and $^5D_0 \rightarrow {}^7F_2$ transitions are split into three and four substates, respectively, thus suggesting that Sm^{2+} occupies a site with C_{2v} or lower symmetry (*Figure 3.3*). The vibronic transitions with energy difference about 98 cm^{-1} were found even at 100 K for the zero phonon line ($^5D_0 \rightarrow {}^7F_0$) of Sm^{2+} derived from the coupling of the excited 4f electrons with local phonons. The decay time of Sm^{2+} in SrB_4O_7 is temperature dependent. Nevertheless, all the decay curves are single exponential. The observed saturation of decay time values for higher than 2.5 % samarium substitution indicate absence of Sm^{2+} concentration quenching, due to negligible interaction between optically active ions.

Chapter 7. Photoluminescence Properties of Sm^{3+} in $LaMgB_5O_{10}$

7.1. Experimental Details

The samples of $La_{0.99}Sm_{0.01}MgB_5O_{10}$ and $Gd_{0.99}Sm_{0.01}MgB_5O_{10}$ were prepared by conventional solid-state reaction method. The starting materials were Sm_2O_3, La_2O_3, Gd_2O_3, MgO and H_3BO_3. 5 wt% of H_3BO_3 was used in excess to compensate its evaporation at high temperature. The stoichiometric amounts of raw materials were thoroughly ground in an agate mortar and then heated in a furnace at 500 °C for 1 h. Subsequent annealing procedure consisted mostly of one heating step [I] at 1020 °C for 8 h in air, CO or $H_2(10\%)/N_2(90\%)$ atmosphere. For some samples annealing with intermediate grinding were repeated once [II] or twice [III] at the same conditions, as indicated in the text.

Excitation (excitation slit 0.3 nm and emission slit 4.0 nm) and emission (excitation slit 4.0 nm and emission slit 0.3 nm) spectra were recorded in the ranges of 250 – 540 and 460 – 800 nm, respectively.

7.2. Data Analysis and Discussion

Figure 7.1 shows the XRD patterns of $La_{0.99}Sm_{0.01}MgB_5O_{10}$ and $Gd_{0.99}Sm_{0.01}MgB_5O_{10}$ samples annealed at 1020 °C for 8 h under air. For the gadolinium-containing sample the background is subtracted because of specimen fluorescence. Peak positions for both compounds match very well the standard XRD data of ICDD#04-010-0668 ($LaMgB_5O_{10}$) for $La_{0.99}Sm_{0.01}MgB_5O_{10}$ and ICDD#04-010-0674 ($GdMgB_5O_{10}$) for $Gd_{0.99}Sm_{0.01}MgB_5O_{10}$. For lanthanum-samarium magnesium borate traces of monoclinic LaB_3O_6 phase (ICDD#04-009-4235) were detected (denoted with asterisk in *Figure 7.1a*). It is interesting to note, that this impurity phase still remained after subsequent annealing steps. Extra peaks, however, are absent in the case of gadolinium compound, neglecting high noise to signal ratio attributed to Gd fluorescence during XRD measurements. Gadolinium magnesium borate peaks are slightly shifted towards higher 2θ values indicating the smaller unit cell, as was stated above. Comparing the XRD

73

results of all synthesized samples no other phase specific changes were observed, except few variations in the peak intensities.
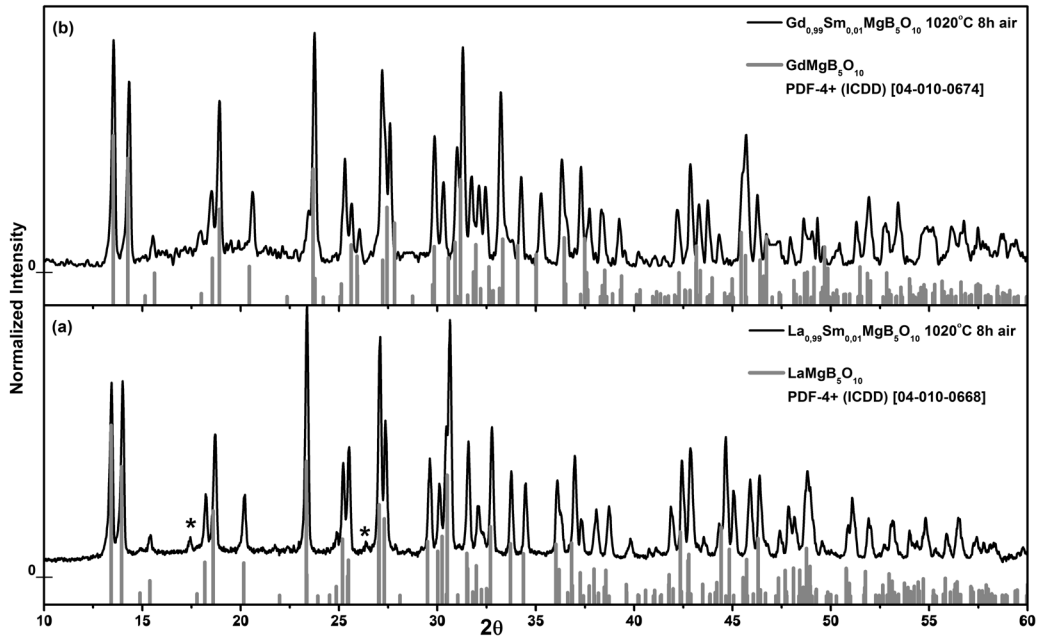
Figure 7.1 XRD patterns of LaMgB$_5$O$_{10}$:Sm^{3+} (a) and GdMgB$_5$O$_{10}$:Sm^{3+} (b) samples annealed at 1020 °C for 8 h in air.

A schematic energy level diagram of transitions in Sm^{3+} is presented in *Figure 7.2*. In general the 4f electrons of rare-earth ions in solids are quite similar to free ions and are rather insensitive to the effects of the surrounding crystal-field, due to outer shell shielding. However, fine structures of photoluminescence emission spectra are still governed by the Stark effect caused by the crystal field effective at the luminescent ion. 4f orbitals of the Sm^{3+} ion are partially filled with five electrons (4f^5) and these unpaired electrons give twice Kramers degeneration in any crystal field lower than cubic. The maximum number of Stark sublevels for Sm^{3+} ion with $^{2S+1}L_J$ multiplets is (2J + 1)/2 due to the Kramers degeneracy of its odd 4f^5 electron configuration. The detailed analysis of the energy levels of Sm^{3+} in several hosts have been reported elsewhere [51, 117]. Under the assumption that samarium replaces lanthanum or gadolinium in LnMgB$_5$O$_{10}$ with C$_1$ symmetry it can be expected to observe 3, 4, 5 and 6 spectral lines for J = 5/2, 7/2, 9/2 and 11/2, respectively, in the orange-red spectral range. The additional lines

2*, 4*, 6* and 8* (*Figure 7.2b*) may be due to several causes including non-equivalent crystallographic sites for the samarium ions, emission from higher excited metastable states and vibronic (hot band) transitions [118]. Some peaks (1*, 3*, 5* and 7*) involving the transition $^4F_{3/2} \rightarrow \, ^6H_j$ are also detected indicating that the $^4F_{3/2}$ level of Sm^{3+} is also populated to some extent [119].
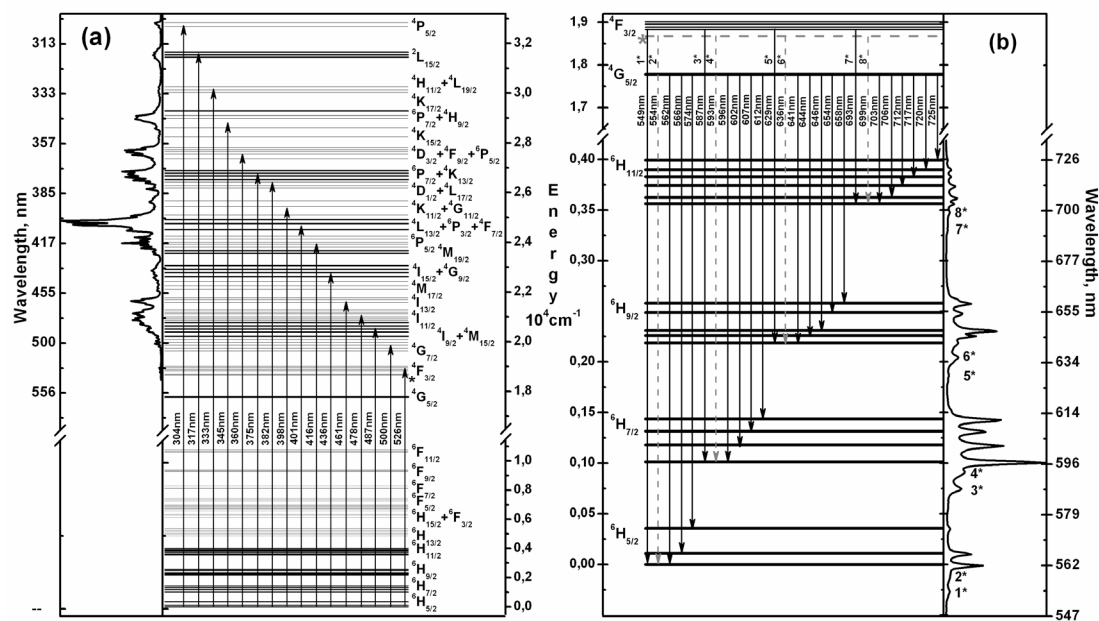
Figure 7.2 Schematic energy level diagram of transitions in Sm^{3+}: for excitation (a), for emission (b). At the sides corresponding spectra of $LaMgB_5O_{10}$:Sm^{3+} are plotted.

Figure 7.3 represents the photoluminescence excitation, emission and diffuse reflection spectra of $La_{0.99}Sm_{0.01}MgB_5O_{10}$ and $Gd_{0.99}Sm_{0.01}MgB_5O_{10}$ powders. The excitation spectra of the specimens were measured by monitoring the emission at 597 nm. In the case of lanthanum magnesium borate all observed peaks are due to the excitation from ground state $^6H_{5/2}$ to higher energy levels of Sm^{3+} ion. It is worth to mention that due to the vast number of excited levels and small energy difference it is difficult to assign unambiguously the correct 4f-4f transitions in Sm^{3+} ion. In excitation spectrum of gadolinium-based compound several additional peak groups at around 253, 274 and 312 nm appears which are assigned to Gd^{3+} ion $^8S_{7/2} \rightarrow \, ^6D_{9/2}$, $^6I_{J/2}$ (where J = 7; 9; 11; 13; 15; 17) and $^6P_{7/2;5/2;3/2}$ transitions, respectively [120]. It is common to observe a ligand-to-metal charge-transfer absorption due to the Sm^{3+}-O^{2-} interaction at the UV region in Sm activated phosphors. However,

there is no obvious charge-transfer absorption of Sm^{3+}-O^{2-} interaction or host absorption band that could be detected in the excitation spectrum (250 – 460 nm). Only direct excitation of Sm^{3+} and Gd^{3+} ions is measured. Therefore, the charge transfer state of the Sm^{3+}-O^{2-} interaction must be below 250 nm (above 5.0 eV). The very broad absorption band (250 – 400 nm) does not result in luminescence and is assigned to defects (urbach-tailing).
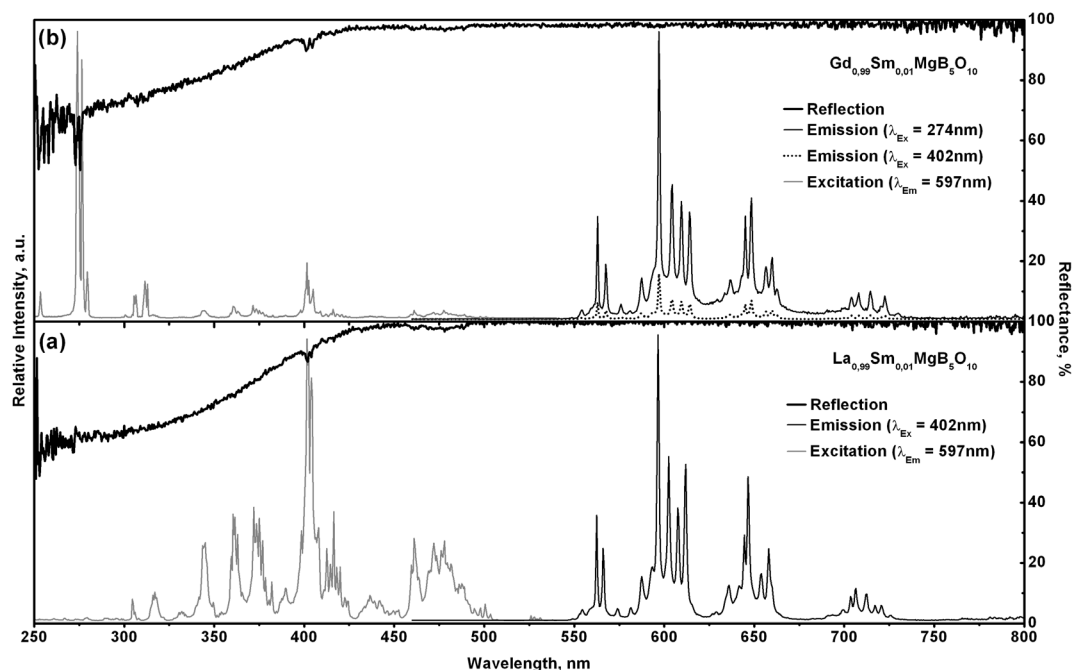
Figure 7.3 Excitation, emission and diffuse reflection spectra of $La_{0.99}Sm_{0.01}MgB_5O_{10}$ (a) and $Gd_{0.99}Sm_{0.01}MgB_5O_{10}$ (b) powders after first annealing step at 1020 °C for 8 h in air.

However $Gd_{0.99}Sm_{0.01}MgB_5O_{10}$ emission spectra clearly show efficient energy transfer between Gd^{3+} and Sm^{3+} ions. Rough estimation of energy transfer efficiency would be division of excitation peaks (274 and 402 nm) integral ratio with emission spectra integral ratio, which gives a value of approximately 60 %. The strongest excitation peak for Sm^{3+} is located at 402 nm assigned to the $^6H_{5/2} \rightarrow {}^4L_{13/2} + {}^6P_{3/2} + {}^4F_{7/2}$ transition and the strongest Gd^{3+} $^8S_{7/2} \rightarrow {}^6I_J$ transition peaking at 274 nm has been selected for the measurement of emission spectrum of samarium doped lanthanide magnesium borate. The dense excited state level structure of Sm^{3+} facilitates rapid non-radiative relaxation and subsequent population of $^4G_{5/2}$ state. This state is separated from the next lower lying $^6F_{11/2}$ by about 7000 cm^{-1}, thus multi-phonon relaxation is

negligible. *Figure 7.3* displays the emission spectra of samarium doped lanthanide magnesium borate powders in the wavelength range of 460 – 800 nm upon 402 nm excitation and additionally at 274 nm in gadolinium based compound. There are four main groups of sharp emission peaks around 560, 600, 650 and 710 nm assigned to the intraconfigurational-4f transitions from the excited state level $^4G_{5/2}$ to ground levels $^6H_{5/2}$, $^6H_{7/2}$, $^6H_{9/2}$ and $^6H_{11/2}$, respectively. Well resolved and sharp peaks indicate strong crystal field (Stark splitting) effect on Sm^{3+} ion [117]. The exact assignment of transitions is given in *Figure 7.2*.

The photoluminescence kinetics of the Sm^{3+} centers in the $La_{0.99}Sm_{0.01}MgB_5O_{10}$ and $Gd_{0.99}Sm_{0.01}MgB_5O_{10}$ powders were characterized by single exponential decay. The example of fitted decay curve of the $^4G_{5/2} \rightarrow$ $^6H_{7/2}$ luminescence in the $LaMgB_5O_{10}:Sm^{3+}$ sample is presented in *Figure 7.4*. The powder was excited at 402 nm wavelength and emission was monitored at 597 nm. The fitted single exponential curve gives experimental lifetime values in the range of 2.2 – 2.4 ms (*Figure 7.4*). Decay time slightly decreases with repeating the annealing step. This can be interpreted by changes in powder crystallinity or defect formation by loss of some boron oxide. Similar behaviour is determined for the samples annealed in different atmospheres. With increasing reducing potential decay time are shortened most likely due to favoured defect formation. As mentioned earlier, due to the difference in the energy gap the multiphonon relaxation rate from $^4G_{5/2}$ level to the $^6F_{11/2}$ level is negligible small for Sm^{3+} ion. According to the literature reports [48, 121], the concentration quenching ($Sm^{3+} \leftrightarrow Sm^{3+}$ interaction) can occur by cross-relaxation processes. Taking into account a relatively small concentration (~1 mol%) of Sm^{3+} ions and single exponential profile of the $^4G_{5/2}$ decay curve one can suppose that concentration quenching in studied samples can be neglected. In case of $Gd_{0.99}Sm_{0.01}MgB_5O_{10}$ compound Sm^{3+} emission decay time is considerably longer for excitation at 274 nm (Gd^{3+} $^8S_{7/2} \rightarrow$ ^6I_J transition) compared to excitation at 402 or 478 nm which nicely confirms the energy transfer assumption.
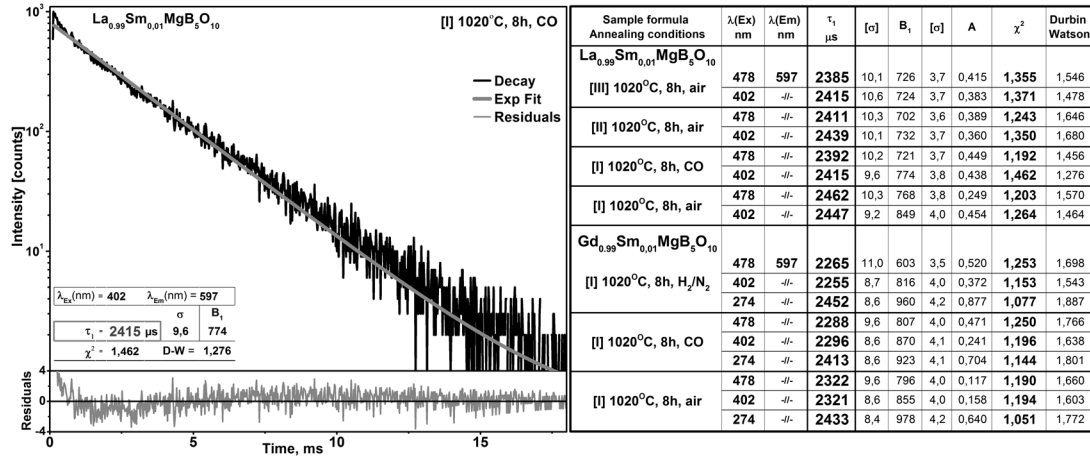
Figure 7.4 Emission decay curve of La₀.₉₉Sm₀.₀₁MgB₅O₁₀ and data for La₀.₉₉Sm₀.₀₁MgB₅O₁₀ and Gd₀.₉₉Sm₀.₀₁MgB₅O₁₀.

Sample formula / Annealing conditions	λ(Ex) nm	λ(Em) nm	τ₁ µs	[σ]	B₁	[σ]	A	χ²	Durbin Watson
La₀.₉₉Sm₀.₀₁MgB₅O₁₀									
[III] 1020°C, 8h, air	478	597	2385	10,1	726	3,7	0,415	1,355	1,546
	402	-//-	2415	10,6	724	3,7	0,383	1,371	1,478
[II] 1020°C, 8h, air	478	-//-	2411	10,3	702	3,6	0,389	1,243	1,646
	402	-//-	2439	10,1	732	3,7	0,360	1,350	1,680
[I] 1020°C, 8h, CO	478	-//-	2392	10,2	721	3,7	0,449	1,192	1,456
	402	-//-	2415	9,6	774	3,8	0,438	1,462	1,276
[I] 1020°C, 8h, air	478	-//-	2462	10,3	768	3,8	0,249	1,203	1,570
	402	-//-	2447	9,2	849	4,0	0,454	1,264	1,464
Gd₀.₉₉Sm₀.₀₁MgB₅O₁₀									
[I] 1020°C, 8h, H₂/N₂	478	597	2265	11,0	603	3,5	0,520	1,253	1,698
	402	-//-	2255	8,7	816	4,0	0,372	1,153	1,543
	274	-//-	2452	8,6	960	4,2	0,877	1,077	1,887
[I] 1020°C, 8h, CO	478	-//-	2288	9,6	807	4,0	0,471	1,250	1,766
	402	-//-	2296	8,6	870	4,1	0,241	1,196	1,638
	274	-//-	2413	8,6	923	4,1	0,704	1,144	1,801
[I] 1020°C, 8h, air	478	-//-	2322	9,6	796	4,0	0,117	1,190	1,660
	402	-//-	2321	8,6	855	4,0	0,158	1,194	1,603
	274	-//-	2433	8,4	978	4,2	0,640	1,051	1,772

7.3. Review of Main Results

Orange-red emitting La$_{0.99}$Sm$_{0.01}$MgB$_5$O$_{10}$ and Gd$_{0.99}$Sm$_{0.01}$MgB$_5$O$_{10}$ photoluminescent materials were synthesized by a solid state reaction method at 1020 °C for 8 h. Four emission bands corresponding to the $^4G_{5/2} \rightarrow {}^6H_{5/2}$, $^6H_{7/2}$, $^6H_{9/2}$ and $^6H_{11/2}$ transitions peaking at 560, 600, 650 and 710 nm, respectively, upon excitation at $^6H_{5/2} \rightarrow {}^4L_{13/2} + {}^6P_{3/2} + {}^4F_{7/2}$ (402 nm) have been observed. $^4F_{3/2} \rightarrow {}^6H_j$ transitions are also detected indicating that the $^4F_{3/2}$ level of Sm^{3+} is also populated to some extent. No obvious charge-transfer absorption of Sm^{3+}-O^{2-} interaction or host absorption band was detected in the excitation spectrum (250 – 460 nm). By direct excitation of Gd^{3+} at 274 nm intense Sm^{3+} emission was measured indicating an efficient energy transfer from Gd^{3+} to Sm^{3+}. The luminescent kinetics data are fitted by single exponential curve giving experimental lifetime values in the range of 2.2 – 2.4 ms. The decay lifetimes for Sm^{3+} emission upon direct excitation of Gd^{3+} is around 0.1 ms longer, confirming the energy transfer phenomena.

Chapter 8. Luminescence of Sm^{3+} in SrAl$_{12}$O$_{19}$ and LaMgAl$_{11}$O$_{19}$

8.1. Experimental Details

For samarium-substituted SrAl$_{11}$O$_{19}$ and LaMgAl$_{11}$O$_{19}$ samples, two main approaches were selected: conventional solid-state reaction and sol–gel combustion method. For solid-state synthesis starting materials were Sm$_2$O$_3$, La$_2$O$_3$, SrCO$_3$ and nano-scale Al$_2$O$_3$. The stoichiometric amounts of raw materials were thoroughly ground in an agate mortar (acetone was used as medium) and, as the first step [I], preheated in a furnace at 1000 °C for 4 h in air. For combustion synthesis the gels were prepared using Sm(NO$_3$)$_3$·6H$_2$O, Sr(NO$_3$)$_2$ and Al(NO$_3$)$_3$·9H$_2$O. Before synthesis La$_2$O$_3$ was dissolved in diluted HNO$_3$ and evaporated to dryness, obtained lanthanum salt solution in water, was used in synthesis. Tris(hydroxymethyl)-aminomethane (tris-amine) or ethylenediaminetetraacetic acid (EDTA) were used as complexing agent and fuel. Metal salts were dissolved in distilled water and heated to 65 – 75 °C; additionally HNO$_3$ was added to prevent hydrolysis of metals. Then, under continuous stirring, tris(hydroxymethyl)-aminomethane (or EDTA) was added with the molar ratio of 1:0.5 or 1:1 (to all metal ions) and solutions were stirred for an additional 1 h at the same temperature. Subsequently, after concentrating the mixtures by slow evaporation, sols turned into transparent gels. Then the temperature was raised to 250 °C and the self-maintaining gel combustion process started and was accompanied with evolution of huge amount of gases. The resulting products were dried in the oven for several hours at 120 °C and ground to fine powders, which were preheated for 4 h at 1000 °C in air (the first step [I]) to remove the residual carbon after the combustion process. In both cases obtained white powders were further sintered (the second step [II]) for 4 – 12 h at 1400 – 1700 °C under air or H$_2$(20%)/N$_2$(80%) atmosphere.

Excitation (excitation slit 0.5 nm and emission slit 5.0 nm) and emission (excitation slit 5.0 nm and emission slit 0.5 nm) spectra were recorded in the ranges of 250 – 500 and 500 – 800 nm, respectively.

8.2. Synthesis Route and Annealing Temperature Influence on Phase Formation

Figure 8.1 shows the XRD patterns of the $Sr_{0.99}Sm_{0.01}Al_{12}O_{19+\delta}$ precursor with trisamine to cations ratio 0.5 (a – b) or 1.0 (c) calcined in static air at 1500 – 1700 °C for 8h. After heating the precursor at 1000 °C for 4 h, the powder is still amorphous, e.g. few very broad bands are detected. Heating the precursor at 1500 °C for 8 h produces a mixture of $SrAl_2O_4$ (ICDD#04-010-5403), Al_2O_3 (ICDD#04-013-1687) and $SrAl_{12}O_{19}$ (ICDD#04-009-5514) as the major phase. Increasing calcination temperature to 1700 °C, the peaks of $SrAl_2O_4$ and Al_2O_3 reduces in size, but still remain with considerable intensity. However, change of fuel ratio influences significantly the magnetoplumbite phase formation. Sample annealed at 1700 °C for 8 h result in $SrAl_{12}O_{19}$ as a major phase with residual traces of Al_2O_3, while no $SrAl_2O_4$ phase is detected. The main function of trisamine or EDTA is to provide a polymeric network to hinder cations mobility, which maintains local stoichiometry and minimizes precipitation of unwanted phase. An added feature of having an organic resin as a carrier is the potential heat of combustion produced during firing. Increasing fuel/M ratio results in more carboxylic groups and polymer gel. The former improves the uniformity of metal element in the solution and gel, the later increases the potential heat of combustion produced during calcinations. Hence, increasing the molar ratio of trisamine to total metal cations concentration enhanced the formation of $SrAl_{12}O_{19}$. The discussed XRD results clearly indicate that combustion method using trisamine as a fuel is not suitable for proper $SrAl_{12}O_{19}$ synthesis.

Figure 8.1 XRD patterns of Sr$_{0.99}$Sm$_{0.01}$Al$_{12}$O$_{19+\delta}$ samples prepared by combustion and annealed at: (a) [II] 1500 °C for 8h (Trisamine 1:0.5), (b) [II] 1700 °C for 8h (Trisamine 1:0.5), (c) [II] 1700 °C for 8h (Trisamine 1:1).

Figure 8.2 shows the XRD patterns of the Sr$_{0.99}$Sm$_{0.01}$Al$_{12}$O$_{19-\delta}$ precursor prepared via combustion with EDTA as fuel. EDTA to cations ratio was selected 1:0.5. The results are completely different as in previous case. Pure SrAl$_{12}$O$_{19}$ phase is obtained even at 1500 °C for 4 h whereas longer annealing time or higher temperature has no influence on phase purity. There is only increase in crystallinity of material, because relative peak intensity increases. Possible explanation for such different influence of synthesis conditions to phase formation could be differences in initial precursor after combustion. Samples prepared with trisamine after annealing at high temperature keep the same volume, while for samples with EDTA decrease in sample volume observed.
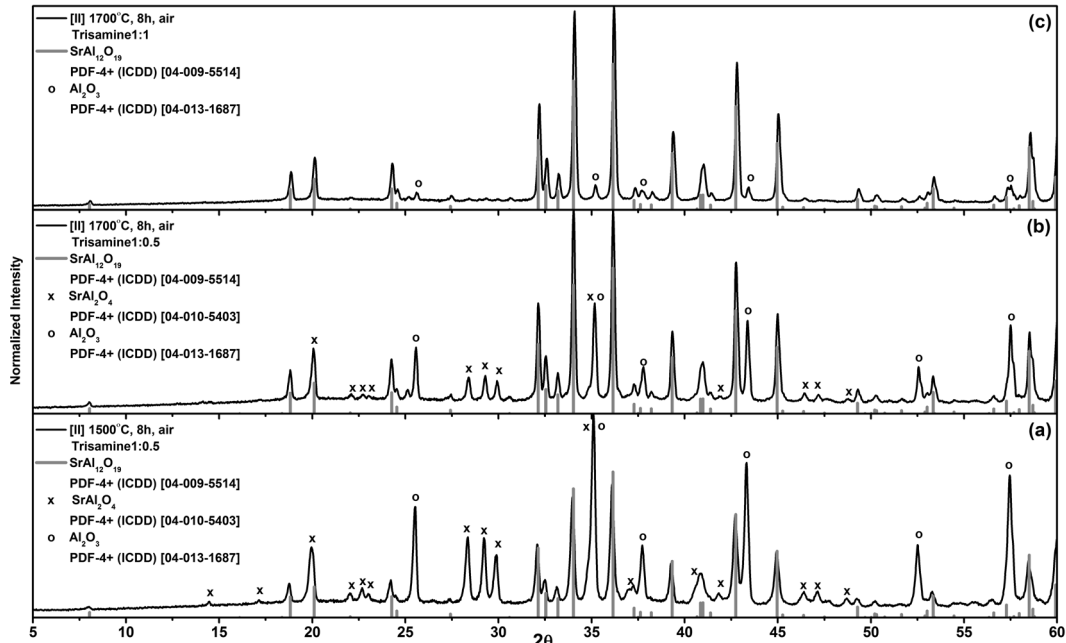
Figure 8.2 XRD patterns of $Sr_{0.99}Sm_{0.01}Al_{12}O_{19+\delta}$ samples prepared by combustion and annealed at: (a) [II] 1500 °C for 4h (EDTA 1:0.5), (b) [II] 1500 °C for 8h (EDTA 1:0.5), (c) [II] 1700 °C for 8h (EDTA 1:0.5).

XRD patterns of samples prepared employing conventional solid-state technique are depicted in *Figure 8.3*. Pattern of sample annealed at [II] 1500 °C (*Figure 8.3a*) reveals main $SrAl_{12}O_{19}$ phase with small peaks of side phases, e.g. $SrAl_2O_4$ and $SrAl_4O_7$ (ICDD#04-007-5368). Increase in annealing temperature ([II] 1700 °C) results in complete decomposition of $SrAl_2O_4$ (*Figure 8.3b*), however, $SrAl_4O_7$ remains with same peaks intensity. Prolonged heating time (8 h) brings no influence for phase purity (*Figure 8.3c*); traces of $SrAl_4O_7$ still remain in samples.
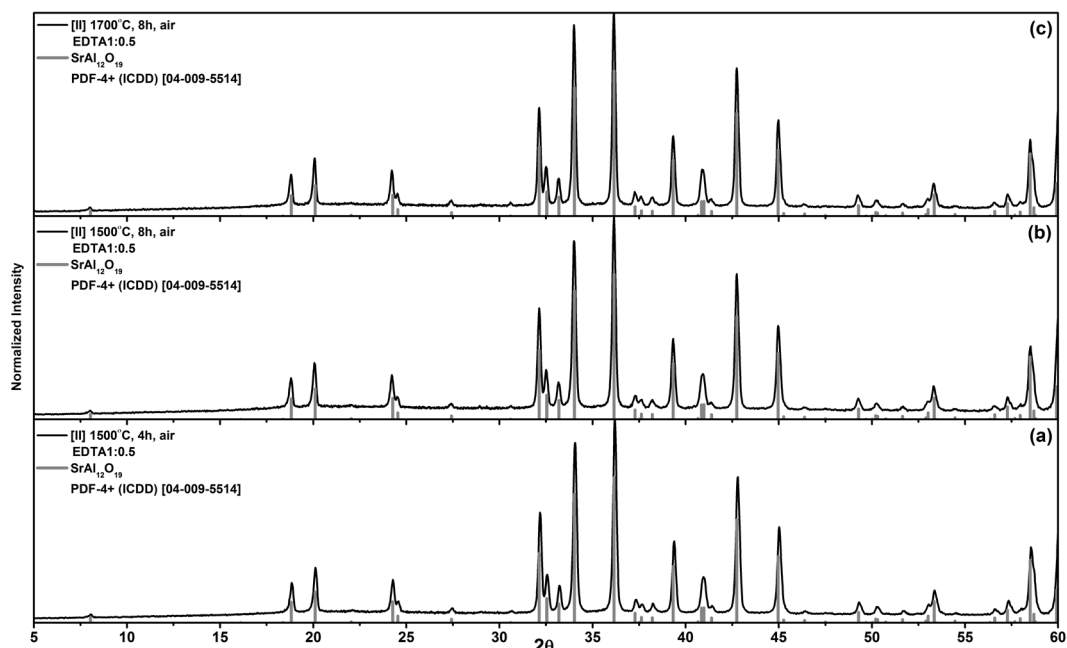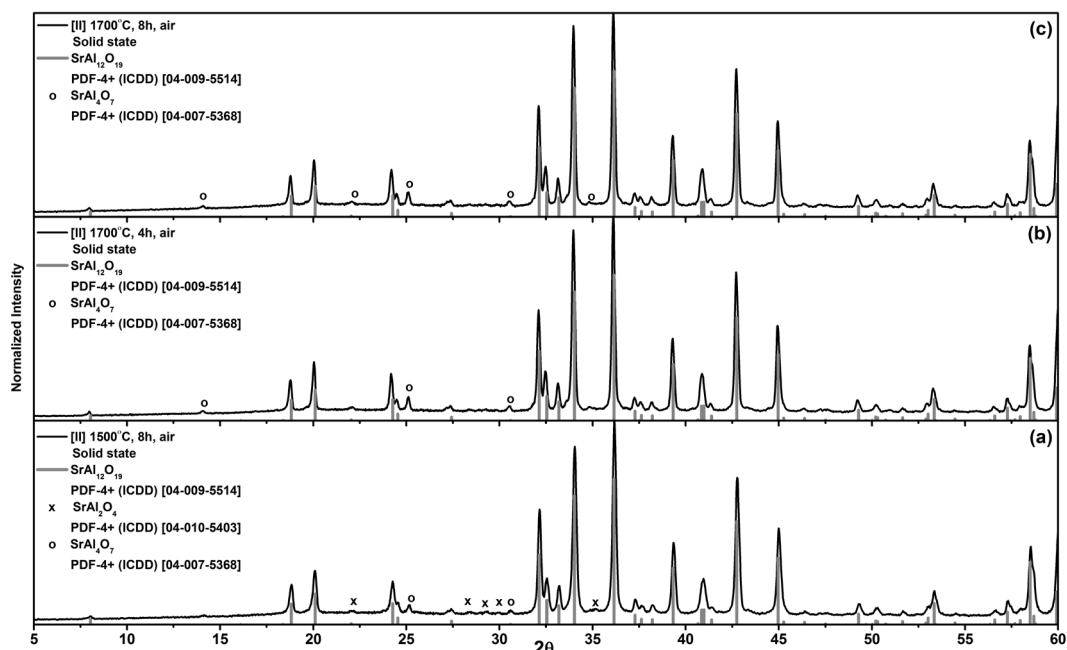
Figure 8.3 XRD patterns of $Sr_{0.99}Sm_{0.01}Al_{12}O_{19+\delta}$ samples prepared by solid-state and annealed at: (a) [II] 1500 °C for 8h, (b) [II] 1700 °C for 4h, (c) [II] 1700 °C for 8h.

In *Figure 8.4* is presented XRD data for $LaMgAl_{11}O_{19}$ prepared via combustion route. The results are different as compared to $SrAl_{12}O_{19}$, the change in fuel nature have no influence on phase formation. Single magnetolumbite structure phase (ICDD#04-006-2251) is obtained after annealing preheated powder at [II] 1400 °C for 4 h (*Figure 8.4a*). There is no evidence of side phase formation and the same behaviour is observed for samples annealed at higher temperature ([II] 1700 °C) (*Figure 8.4b-c*).
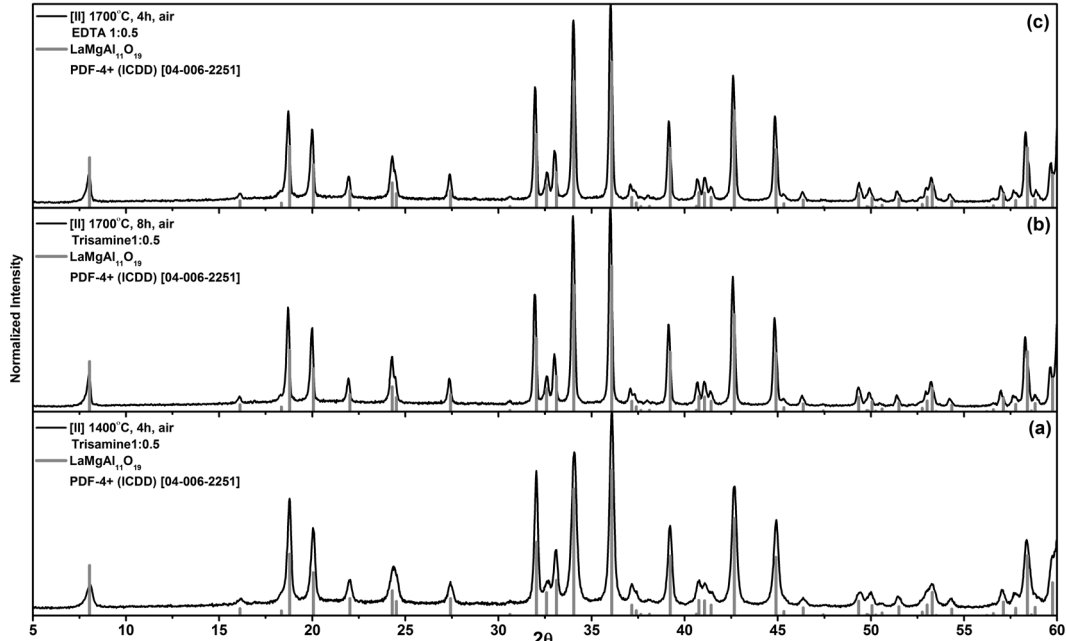
Figure 8.4 XRD patterns of La$_{0.99}$Sm$_{0.01}$MgAl$_{11}$O$_{19}$ samples prepared by combustion and annealed at: (a) [II] 1400 °C for 4h (Trisamine 1:0.5), (b) [II] 1700 °C for 8h (Trisamine 1:0.5), (c) [II] 1700 °C for 4h (EDTA 1:0.5).

8.3. Luminescence Properties of Samarium Doped Magnetoplumbite

The emission spectrum of trivalent samarium (Sm^{3+}) is dominated by transitions from the ^{4}G$_{5/2}$ excited state located at about 17 500 cm^{-1} [15]. With 404 nm (24752 cm^{-1}) excitation the ^{4}G$_{5/2}$ state is the only luminescent level; small energy gaps between all above-lying levels assure their efficient non-radiative relaxation leading to the population of the ^{4}G$_{5/2}$ state. This state is separated from the next lower lying ^{6}F$_{11/2}$ by about 7000 cm^{-1}. It makes the multiphonon relaxation negligible: 10 host's phonons with the highest energy of 650 cm^{-1} are needed to cover this energy gap. Thus, it seems that radiative transitions and relaxation by non-radiative energy transfer are the main processes, which can depopulate the ^{4}G$_{5/2}$ state. The strongest emission is observed in the red part of the spectrum. *Figure 8.5* shows the 1.0 % samarium substituted SrAl$_{12}$O$_{19}$ (a) and LaMgAl$_{11}$O$_{19}$ (b) sample luminescence data acquired in 250-800 nm spectral range at room temperature. All observed emission bands correspond to transitions from the ^{4}G$_{5/2}$ fluorescent state to the ^{6}H$_{7/2-13/2}$ excited levels and to the ^{6}H$_{5/2}$ ground state. The ^{4}G$_{5/2}$→^{6}H$_{7/2}$ emission

with the most intense line at 16920 cm^{-1} as well as the $^4G_{5/2} \rightarrow {}^6H_{9/2}$ band at 15649 cm^{-1} and $^4G_{5/2} \rightarrow {}^6H_{5/2}$ (17857 cm^{-1}) are dominant in spectrum. The band's assignment, presented in *Figure 8.5*, was based on energy multiplet calculations made for Sm^{3+} in Y$_3$Al$_5$O$_{12}$ [51]. Several transitions have been included into one complex of a broad band because the crystal-field (CF) splitting of the neighboring multiplets is frequently larger than their energy separations.
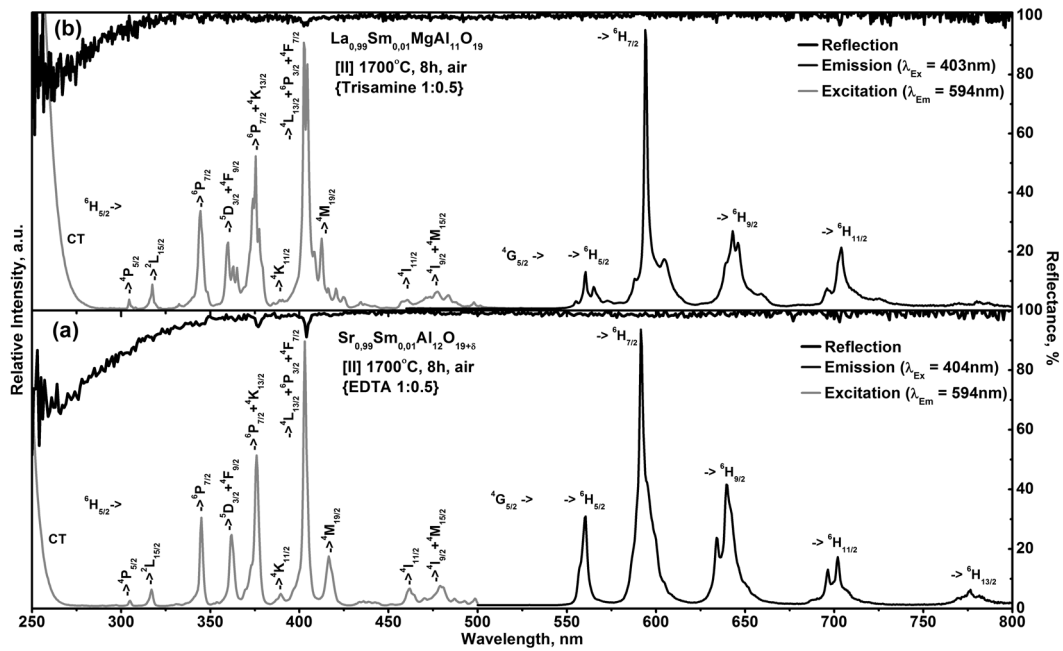
Figure 8.5 Excitation, emission and diffuse reflection spectra of samples annealed at [II] 1700 °C for 8h under air: (a) Sr$_{0.99}$Sm$_{0.01}$Al$_{12}$O$_{19-\delta}$, (b) La$_{0.99}$Sm$_{0.01}$MgAl$_{11}$O$_{19}$.

Excitation spectrum of SrAl$_{12}$O$_{12}$:Sm^{3+} (*Figure 8.5a*) for the 594 nm emission consists of a series of sharp peaks in the 300–500 nm range with the strongest peak at 404 nm and some peaks at 305 ($^6H_{5/2} \rightarrow {}^4P_{5/2}$), 317 ($^6H_{5/2} \rightarrow {}^2L_{15/2}$), 345 ($^6H_{5/2} \rightarrow {}^6P_{7/2}$), 362 ($^6H_{5/2} \rightarrow {}^5D_{3/2}$; $^4F_{9/2}$; $^6P_{5/2}$), 376 ($^6H_{5/2} \rightarrow {}^6P_{7/2}$; $^4K_{13/2}$), 389 ($^6H_{5/2} \rightarrow {}^4K_{11/2}$), 416 ($^6H_{5/2} \rightarrow {}^4M_{19/2}$), 469 ($^6H_{5/2} \rightarrow {}^4I_{11/2}$) and 479 nm ($^6H_{5/2} \rightarrow {}^4I_{9/2}$; $^4M_{15/2}$). These peaks are ascribed to the transitions from the ground state to the excited states of Sm^{3+}. In addition, there is a wide band in the region starting at 260–270 nm. This band is attributed to the electron transition in O$^{2-} \rightarrow$ Sm^{3+} couple (charge transfer [CT]). The strongest excitation induced by the $^6H_{5/2} \rightarrow {}^4L_{13/2}$; $^6P_{3/2}$; $^4F_{7/2}$ (404 nm) transition has

been selected for the measurement of emission spectrum of $SrAl_{12}O_{12}:Sm^{3+}$ phosphor. The intense peak at 404 nm indicates that this kind of phosphor can be effectively excited by near-ultraviolet light-emitting diodes.

The emission spectrum of $SrAl_{12}O_{19}:Sm^{3+}$ obtained by excitation at 404 nm is shown in *Figure 8.5a*. Under the excitation at 404 nm, five bands located at 560, 591, 639, 702 and 776 nm are observed and they are assigned to the $^4G_{5/2} \to ^6H_J$ (J = 5/2, 7/2, 9/2, 11/2, 13/2) transitions of Sm^{3+}. Among them, the transition $^4G_{5/2} \to ^6H_{7/2}$ (591 nm) has relatively higher emission intensity than the other transitions. The first one at 560 nm ($^4G_{5/2} \to ^6H_{5/2}$) is a magnetic-dipole transition, the second at 591 nm ($^4G_{5/2} \to ^6H_{7/2}$) is a partly magnetic and partly a forced electric-dipole transition and the other at 639 nm ($^4G_{5/2} \to ^6H_{9/2}$) is purely electric-dipole transition, which is sensitive to the crystal field. The intensity ratio of electric-dipole to magnetic-dipole transition can be used to measure the symmetry of the local environment of the trivalent 4f ions. In general, the electric-dipole transition will be of greater intensity for more asymmetric local environment. In the present investigation, no substantial differences were observed in the intensities of electric-dipole ($^4G_{5/2} \to ^6H_{9/2}$) and magnetic-dipole ($^4G_{5/2} \to ^6H_{5/2}$) transitions. Further, emission bands split into components. These splitting of energy levels are caused by the crystal field interaction.

For the emission of Sm^{3+} ion in $LaMgAl_{11}O_{19}$ (*Figure 8.5b*) prominent peaks are observed at 560, 594, 643 and 704 nm (excitation wavelength 403 nm). The peak positions vary little with the host lattice and are assigned to the transitions $^4G_{5/2} \to ^6H_{5/2}$, $^4G_{5/2} \to ^6H_{7/2}$, $^4G_{5/2} \to ^6H_{9/2}$ and $^4G_{5/2} \to ^6H_{11/2}$ of Sm^{3+}. Furthermore, there is associated line structure in the excitation spectrum, corresponding to the transition within the $4f^5$ configuration and accordingly assignment is the same as in $SrAl_{12}O_{19}:Sm^{3+}$ case.
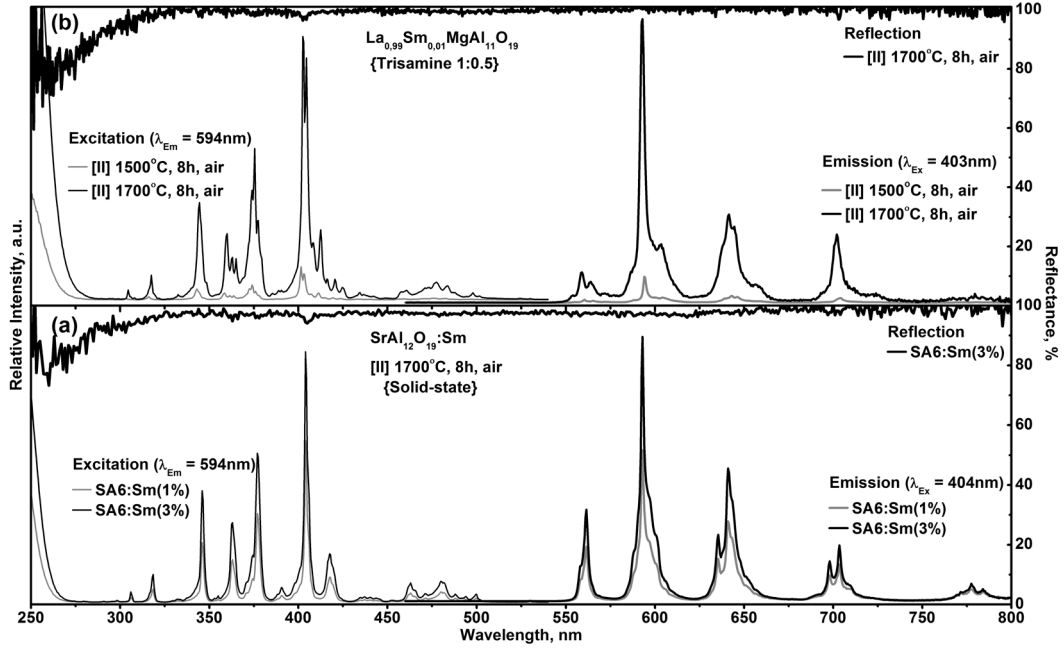
Figure 8.6 Excitation, emission and diffuse reflection spectra of samples: (a) $Sr_{0.99}Sm_{0.01}Al_{12}O_{19-\delta}$ and $Sr_{0.97}Sm_{0.03}Al_{12}O_{19-\delta}$ annealed at [II] 1700 °C for 8h under air (solid-state): (b) $La_{0.99}Sm_{0.01}MgAl_{11}O_{19}$ annealed at [II] 1500 and 1700 °C for 8h under air (Trisamine 1:0.5).

Since Sm^{3+} properties are similar in both hosts the concentration dependant data are given for $SrAl_{12}O_{19}$ (*Figure 8.6a*) and annealing temperature influence for $LaMgAl_{11}O_{19}$ (*Figure 8.6b*). As it is expected the increase in Sm^{3+} concentration give more intense luminescence spectra, however relative change in intensity is not so big as the concentration difference. One should suppose that ion–ion interactions are active in the samarium doped magnetoplumbite structure system. Such dependence suggests that cross-relaxation processes affect fluorescence of the $^4G_{5/2}$ manifold in $SrAl_{12}O_{19}:Sm^{3+}$ (or $LaMgAl_{11}O_{19}:Sm^{3+}$). Match for transitions is achieved (based on level energies resonance) whereas such cross-relaxation process as $^4G_{5/2} \rightarrow {}^6F_{9/2} \approx {}^6H_{5/2} \rightarrow {}^6F_{7/2}$ or $^4G_{5/2} \rightarrow {}^6F_{7/2} \approx {}^6H_{5/2} \rightarrow {}^6F_{9/2}$ can occur with simultaneous emission of phonons (phonon-assisted process) [50]. Additionally, the existence of several Sm^{3+} centers in these hosts can play positive role in the energetic adjustment. *Figure 8.6b* shows annealing temperature influence on 1% Sm^{3+} substituted $LaMgAl_{11}O_{19}$. Substantial

increase in intensity is detected due to higher crystallinity of samples annealed at higher temperature.
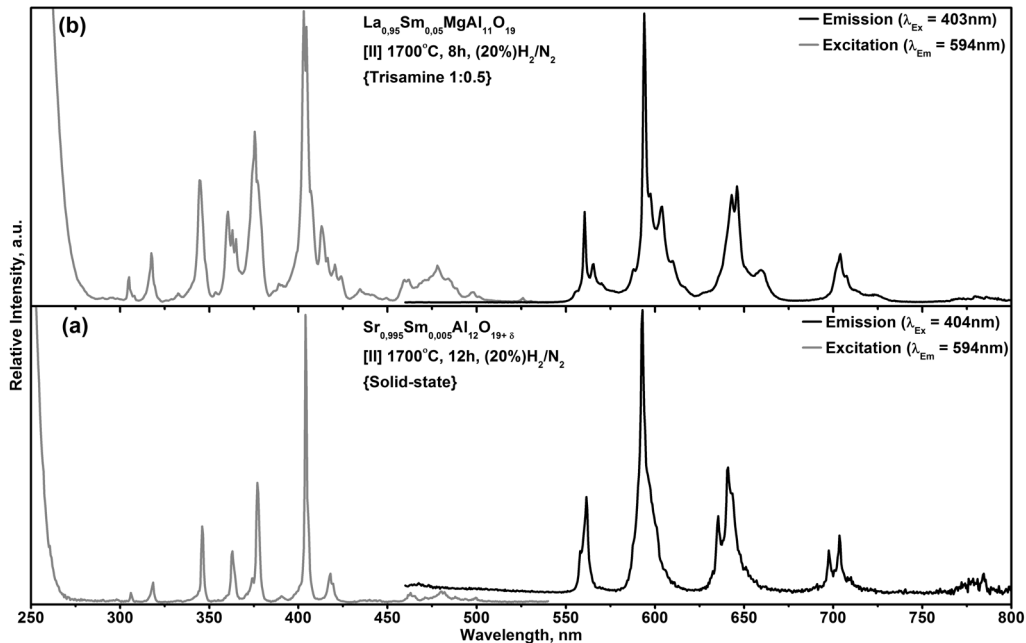
Figure 8.7 Excitation and emission spectra of samples annealed at [II] 1700 °C for 8h under $H_2(20\%)/N_2(80\%)$: (a) $Sr_{0.995}Sm_{0.005}Al_{12}O_{19-\delta}$, (b) $La_{0.995}Sm_{0.005}MgAl_{11}O_{19}$.

In *Figure 8.7* is presented data for samples annealed under highly reducing atmosphere (20% H_2/N_2) at 1700 °C. It is interesting to note that no traces of Sm^{2+} are detected. Despite the suitable twelve-coordinated divalent site in $SrAl_{12}O_{19}$ samarium still remains in trivalent state. For proper explanation of this effect additional experiments should be performed, like sample irradiation with high-energy rays in order to determine host influence on Sm^{3+} stability.

In *Table 8.1* is depicted time dependant emission data for Sm^{3+} doped $SrAl_{12}O_{19}$ and $LaMgAl_{11}O_{19}$. The decay curves of all samples were found to be single exponential. The decay data is measured for $^4G_{5/2} \rightarrow {}^6F_{7/2}$ transition at room temperature. All decay values fit into 2.1 – 3.0 ms range, which is characteristic to trivalent samarium. Decrease in decay value is detected for samples with higher samarium concentration indicating above mentioned cross-relaxation process, while reasons for decrease in higher crystallinity samples are not so obvious. This might be due to facilitated defect formation at

higher temperatures. Sm^{3+} emission decay in $LaMgAl_{11}O_{19}$ samples are around 10 % shorter as compared to strontium hexaaluminate, the measured difference may be attributed to the change in local field.

Table 8.1 Lifetime data for Sm^{3+} emission in $SrAl_{11}O_{19}:Sm$ prepared via solid-state and $La_{0.99}Sm_{0.01}MgAl_{11}O_{19}$ – via combustion (trisamine 1:0.5) routes.

	$\lambda_{(Ex)}$	$\lambda_{(Em)}$	τ, μs	σ	B_1	σ	A	χ^2	D-W
SA6:Sm(1%) [II] 1500°C, 4h, air	404	593	2922	7,85	433,7	1,32	0,762	1,351	1,630
SA6:Sm(1%) [II] 1500°C, 8h, air	-//-	-//-	3050	7,01	579,5	1,50	0,897	1,300	1,622
SA6:Sm(1%) [II] 1700°C, 4h, air	-//-	-//-	2760	4,78	913,8	1,92	-0,144	1,076	1,845
SA6:Sm(1%) [II] 1700°C, 8h, air	-//-	-//-	2753	4,66	955,3	1,96	-0,096	1,120	1,884
SA6:Sm(3%) [II] 1500°C, 4h, air	-//-	-//-	2914	6,31	659,5	1,63	1,295	1,488	1,483
SA6:Sm(3%) [II] 1500°C, 8h, air	-//-	-//-	2969	6,29	682,0	1,65	1,176	1,439	1,521
SA6:Sm(3%) [II] 1700°C, 4h, air	-//-	-//-	2551	4,22	1018	2,10	0,174	1,091	1,876
SA6:Sm(3%) [II] 1700°C, 8h, air	-//-	-//-	2531	4,22	1005	2,09	0,168	1,105	1,840
SA6:Sm(0.5%) [II] 1700°C, 12h, H_2/N_2	-//-	-//-	3079	6,54	624,8	1,52	-0,256	1,132	1,934
LaMAO:Sm(1%) [II] 1400°C, 4h, air	403	594	2607	4,62	903,2	1,96	0,420	1,146	1,843
LaMAO:Sm(1%) [II] 1400°C, 8h, air	-//-	-//-	2570	4,72	926,6	2,02	0,481	1,213	1,873
LaMAO:Sm(1%) [II] 1500°C, 4h, air	-//-	-//-	2424	4,49	927,4	2,07	0,365	1,135	1,882
LaMAO:Sm(1%) [II] 1500°C, 8h, air	-//-	-//-	2400	4,53	905,1	2,06	0,350	1,144	1,877
LaMAO:Sm(1%) [II] 1600°C, 8h, air	-//-	-//-	2243	4,46	921,5	2,16	0,118	1,111	1,941
LaMAO:Sm(1%) [II] 1700°C, 8h, air	-//-	-//-	2128	4,21	952,1	2,24	0,007	1,092	1,904
LaMAO:Sm(1%) [II] 1400°C, 8h, H_2/N_2	-//-	-//-	2286	4,67	866,8	2,08	0,184	1,145	1,859

8.4. Review of Main Results

It was found that the best suitable synthesis technique to get phase pure $SrAl_{12}O_{19}$ is combustion with EDTA as fuel. The same structure $LaMgAl_{11}O_{19}$ pure phase can be synthesized via same method regardless the fuel used. Single phase for both materials are obtained after annealing at 1400 – 1500 °C for 4 h in static air. The trivalent samarium emission spectra contained the $^4G_{5/2} \rightarrow {}^6H_J$

(J = 5/2, 7/2, 9/2, 11/2 and 13/2) transitions, which were detected in the 550 – 780 nm range. No obvious conclusion about Sm^{3+} occupied site symmetry could be made due to insufficient clarity of the shape and intensity of observed transitions. Excitation spectra in the range of 250 – 500 nm resulted in sharp $4f^5$-$4f^5$ transitions, which were labeled using reference data for Sm^{3+} transitions in $Y_3Al_5O_{12}$. Annealing under highly reducing conditions at high temperature revealed that examined magnetoplumbite hosts are not suitable for samarium reduction to divalent state. The measured emission decay values fall into the range of 2.1 – 2.7 ms for $LaMgAl_{11}O_{19}$:Sm^{3+} and 2.5 – 3.0 ms for $SrAl_{12}O_{19}$:Sm^{3+}.

Chapter 9. *Photoluminescence Properties of $Sm^{2+/3+}$ in $Sr_4Al_{14}O_{25}$*

9.1. Experimental Details

For samarium-doped $Sr_4Al_{14}O_{25}$ samples two different approaches were selected: conventional solid-state reaction and sol–gel combustion method. For solid-state synthesis starting materials were Sm_2O_3, $SrCO_3$ and nano-scale Al_2O_3. The H_3BO_3, NH_4Cl and AlF_3 were selected as fluxes. The stoichiometric amounts of raw materials were thoroughly ground in an agate mortar (acetone was used as medium) and then preheated in a furnace at 1000 °C for 4 h in air. For combustion synthesis the gels were prepared using $Sm(NO_3)_3 \cdot 6H_2O$, $Sr(NO_3)_2$ and $Al(NO_3)_3 \cdot 9H_2O$. Tris(hydroxymethyl)-aminomethane (tris-amine) or ethylenediaminetetraacetic acid (EDTA) were used as complexing agent and fuel. Metal salts were dissolved in distilled water and heated to 65 – 75 °C; additionally HNO_3 was added to prevent hydrolysis of metals. Then, under continuous stirring, tris(hydroxymethyl)-aminomethane (or EDTA) was added with the molar ratio of 1:0.5 (to all metal ions) and solutions were stirred for an additional 1h at the same temperature. Subsequently, after concentrating the mixtures by slow evaporation, sols turned into transparent gels. Then the temperature was raised to 250 °C and the self-maintaining gel combustion process started and was accompanied with evolution of huge amount of gases. The resulting products were dried in the oven for several hours at 120 °C and ground to fine powders, which were preheated for 4 h at 1000 °C in air to remove the residual carbon after the combustion process. In both cases obtained white powders were further sintered once or twice ([II] or [III] steps) for 8 h at 1300 °C (or 1400 °C) under CO or $H_2(10\%)/N_2(90\%)$ atmosphere.

Excitation (excitation slit 0.5 nm and emission slit 5.0 nm) and emission (excitation slit 5.0 nm and emission slit 0.5 nm) spectra were recorded in the ranges of 250 – 640 and 460 – 900 nm, respectively.

9.2. Influence of Flux on $Sr_4Al_{14}O_{25}$ Phase Formation

Figure 9.1 and *Figure 9.2* present the XRD patterns of strontium aluminates phase distribution after various synthesis steps. Since attempts to obtain single-phase $Sr_4Al_{14}O_{25}$ failed, it was chosen to use additives, besides addition of flux significantly reduces the formation temperature and time [122]. The influence of different flux on the formation of S4A7 phase, the boric acid (H_3BO_3, m.p. 577 °C), ammonium chloride (NH_4Cl, m.p. 340 °C) and aluminum fluoride (AlF_3, m.p. 1291 °C) were used. The XRD patterns of $Sr_{3.88}Sm_{0.12}Al_{14}O_{25}$ (S4A7:Sm) samples, synthesized via solid-state method, are shown in *Figure 9.1*. The patterns (a) and (b) are for the sample prepared with 2.5 wt% of H_3BO_3 flux. After the first heating at 1000 °C for 4 h in air (*Figure 9.1a*) the blend of three different strontium aluminates appears. The major phase is monoclinic $SrAl_4O_7$ (ICDD#04-007-5368) and two minor phases, monoclinic $SrAl_2O_4$ (ICDD#04-010-5403) and orthorhombic $Sr_4Al_{14}O_{25}$ (ICDD#01-089-8206) are indentified. After second annealing at 1300 °C for 4h in H_2/N_2 (*Figure 9.1b*) or CO (XRD not included) atmosphere single phase $Sr_4Al_{14}O_{25}$ was obtained. Therefore, synthesis of $Sr_4Al_{14}O_{25}$ involves complex reaction processes in which $SrAl_4O_7$ and $SrAl_2O_4$ are formed as intermediate phases. However, samples prepared with NH_4Cl flux show no traces of S4A7 phase formation even after twice repeated annealing at 1300 °C for 8 h (*Figure 9.1c*). NH_4Cl addition to the raw materials, after prolonged annealing, results in composition of three strontium aluminates: $SrAl_2O_4$, orthorhombic $SrAl_{12}O_{19}$ (ICDD#04-009-5514) and traces of $SrAl_4O_7$. The aluminum fluoride was also used as a flux, where 2 wt% of initial Al_2O_3 powder were replaced by AlF_3. As indicated in *Figure 9.1d*, it influences S4A7 phase formation, but probably the fluoride concentration is too low for the acceleration of initial reaction. Even twice repeated annealing at 1300 °C for 8 h gives only minor amount of S4A7 in the mixture of strontium aluminates.

92
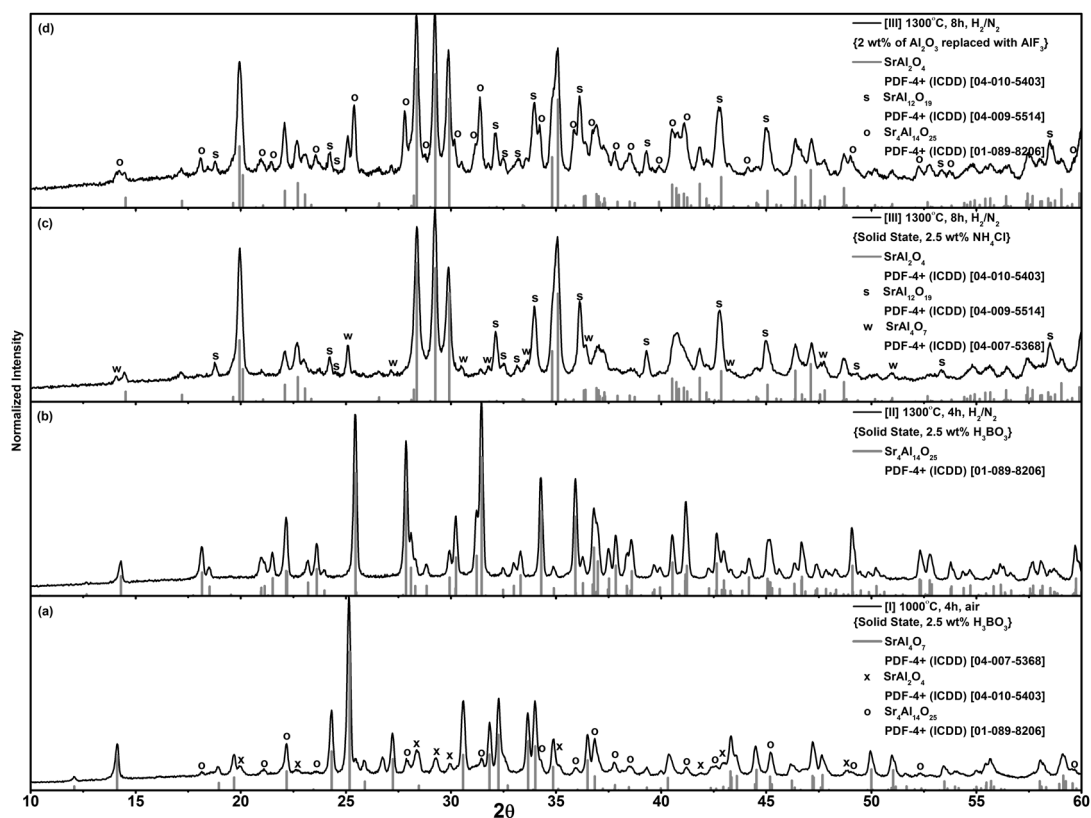
Figure 9.1 XRD patterns of S4A7:Sm samples prepared by solid-state and annealed at: (a) [I] 1000 °C for 4 h (2.5 wt% H_3BO_3), (b) [II] 1300 °C for 4 h (2.5 wt% H_3BO_3), (c) [III] 1300 °C for 8 h (2.5 wt% NH_4Cl), (d) [III] 1300 °C for 8 h (2 wt% AlF_3).

The XRD patterns of samples synthesized by combustion method are depicted in *Figure 9.2*. Two different fuels, tris-amine (*Figure 9.2a-b*) and EDTA (*Figure 9.2c-d*), were tested. To initial solutions during synthesis 2.5 wt% of H_3BO_3 were added. Change in the synthesis route brought the difference in the composition and promoted formation $Sr_3Al_2O_6$ (ICDD#04-007-5481) phase after heating at 1000 °C for 4 h (*Figure 9.2a, c*). In the case of tris-amine the $Sr_3Al_2O_6$ and $SrAl_2O_4$ phases with higher diffraction peak intensity compared to EDTA route have formed. Also additional traces of $SrAl_4O_7$ phase were also observed. However, twice repeated annealing at higher temperature (1400 °C) resulted only in small fraction of S4A7 in strontium aluminates blend (*Figure 9.2b, d*). It is worth to mention that addition of 2.5 wt% H_3BO_3 to the samples after the first [I] step (1000 °C, 4 h)

resulted in single phase S4A7 at 1300 °C. Therefore, it can be concluded that boric acid is lost during the initial combustion process.
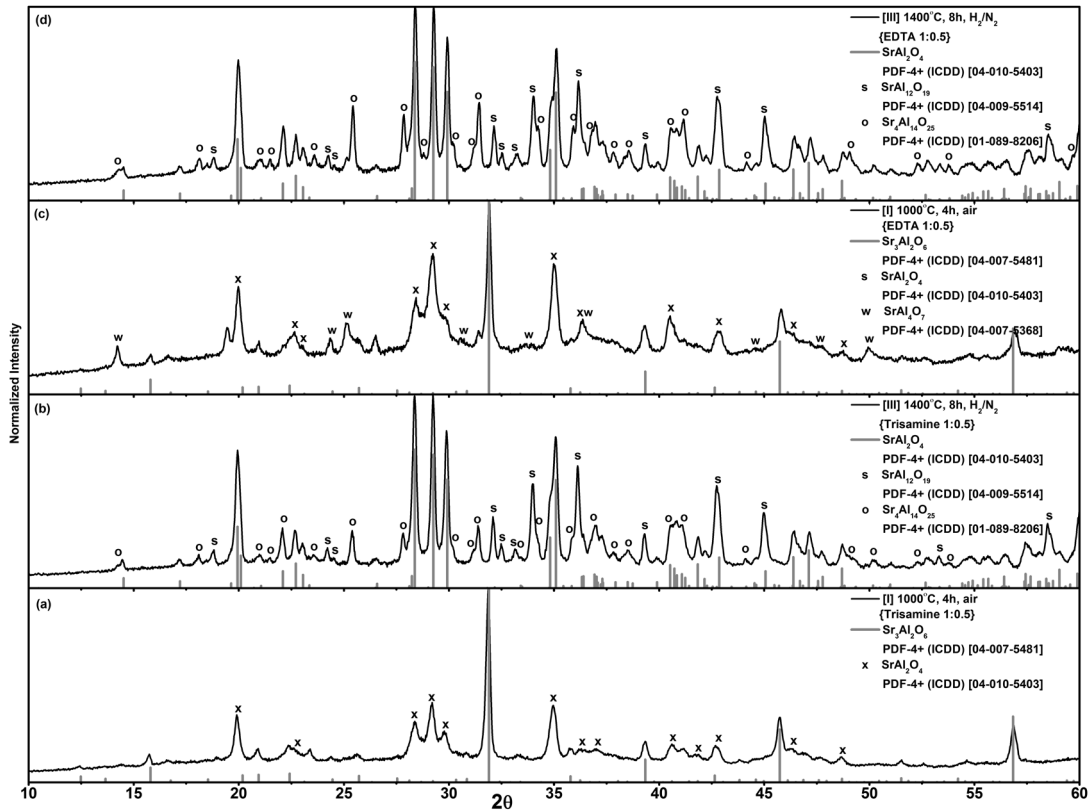
Figure 9.2 XRD patterns of S4A7:Sm samples prepared by combustion and annealed at: (a) [I] 1000 °C for 4 h (Trisamine 1:0.5), (b) [III] 1400 °C for 8 h (Trisamine 1:0.5), (c) [I] 1000 °C for 4 h (EDTA 1:0.5), (d) [III] 1400 °C for 8 h (EDTA 1:0.5).

9.3. Synthesis Conditions Influence on Samarium Oxidation State

The photoluminescence spectra of S4A7:Sm^{3+}(1 %) annealed under CO atmosphere are shown in *Figure 9.3a*. The emission spectrum of exclusively trivalent samarium (Sm^{3+}) is dominated in samples after second annealing step ([II] under CO) by transitions from the $^4G_{5/2}$ excited state located at about 18000 cm^{-1}. Due to the large energy gap of about 7000 cm^{-1} to the next lower level, the $^4G_{5/2}$ relaxation is predominantly radiative. The strongest emission is observed in the red part of the spectrum. For the emission of Sm^{3+} ion in S4A7, prominent peak sets are observed at 561, 599, 646 and 705 nm (excitation wavelength 399 nm). The peak position variation is negligible with the host lattice and is assigned to the intra-4f-shell transitions from the excited state

94

$^4G_{5/2}$ to ground levels $^6H_{5/2}$, $^6H_{7/2}$, $^6H_{9/2}$ and $^6H_{11/2}$ (*Figure 9.3a*). Fine structure of photoluminescence emission spectra are governed by the Stark effect caused by the crystal-field. 4f orbitals of the Sm^{3+} ion are partially filled with five electrons ($4f^5$) and these unpaired electrons give twice Kramer degeneration in any crystal-field lower than cubic. The maximum number of Stark sublevels for Sm^{3+} ion with $^{2S+1}L_J$ multiplets is $(2J + 1)/2$ due to the Kramer degeneracy of its odd $4f^5$ electron configuration. As expected, for low symmetry, 3, 4 and 5 spectral lines are observed for J = 5/2, 7/2 and 9/2, respectively. Extra peaks with low intensity at 551, 589 and 633 nm are assigned to the $^4F_{3/2}{\rightarrow}^6H_J$ transitions indicating that the $^4F_{3/2}$ level of Sm^{3+} is also populated to some extent.
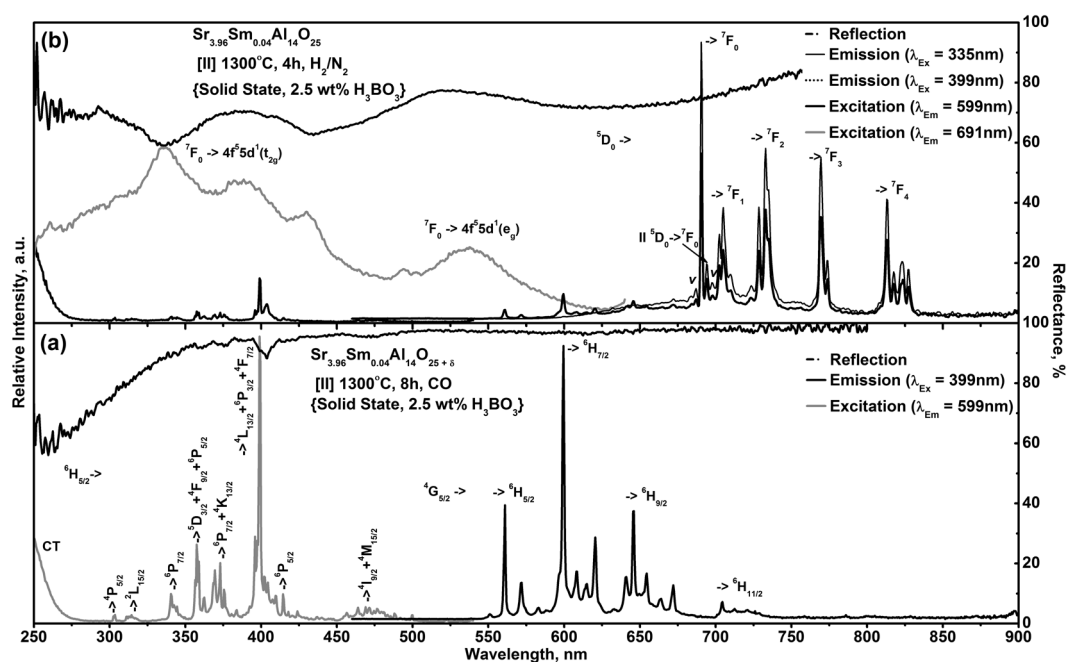
Figure 9.3 Excitation, emission and diffuse reflection spectra of S4A7:Sm annealed at different conditions: (a) [II] 1300 °C for 8 h under CO atmosphere, (b) [II] 1300 °C for 4 h under H₂/N₂ atmosphere.

The excitation spectra of the specimen were measured by monitoring the emission at 599 nm (*Figure 9.3a*). There is associated line structure in the excitation spectrum, corresponding to the transition within the $4f^5$ configuration from ground-level $^6H_{5/2}$ to higher energy levels of Sm^{3+} ion: $\approx$ 471 nm ($^4I_{9/2}+^4M_{15/2}$), 414 nm ($^6P_{5/2}$), 399 nm ($^4L_{13/2}+^6P_{3/2}+^4F_{7/2}$), 373 nm ($^6P_{7/2}+^4K_{13/2}$), 357 nm ($^5D_{3/2}+^4F_{9/2}+^6P_{5/2}$), 340 nm($^6P_{7/2}$), 315 nm ($^2L_{15/2}$), 303

nm ($^4P_{5/2}$) [51]. Part of the ligand-to-metal charge-transfer (CT) absorption band due to the Sm^{3+}-O^{2-} interaction appears at 250 nm. The broad absorption band (250 – 350 nm) in the reflection spectrum does not result in luminescence and is assigned to defects (Urbach-tailing). However, after the annealing under stronger reducing conditions (H_2/N_2) Sm^{2+} emission is dominant (*Figure 9.3b*). In S4A7:Sm^{2+}(1 %) the lowest $4f^5 5d^1$ state occurs about 18000 cm^{-1} above the ground $^7F_0$ level of $4f^6$ and strong 4f-4f luminescence from the $^5D_0$ to $^7F_{0-4}$ levels is observed upon excitation of the parity-allowed $4f^6 \rightarrow 4f^5 5d^1$ interconfigurational transitions. The most intensive peak at 691 nm (14472 cm^{-1}) is assigned to the $^5D_0 \rightarrow {}^7F_0$ transition representing weaker host influence on Sm^{2+} as in comparison to more ionic systems: fluorides or fluorohalides [60]. The position of this level depends on the iconicity of the system and additionally on the size and coordination of the dopant site. The transition, at slightly lower energy 695 nm (14409 cm^{-1}), could be assigned to (II) $^5D_0 \rightarrow {}^7F_0$ of the Sm^{2+} ions occupying different Sr^{2+} site. Substantially lower intensity of this line indicates non-equal Sr^{2+} site occupation regardless even distribution of Sr1 and Sr2 cavities [123]. The very weak lines at the both sides of the $^5D_0 \rightarrow {}^7F_0$ transition are phonon satellite lines, denoted as *v* in (*Figure 9.3b*). The phonon lines are originated from the transition in which $^5D_0$ and $^7F_0$ states have different lattice vibration levels. The groups of transitions at around 705, 733, 770 and 813 nm are assigned to $^5D_0 \rightarrow {}^7F_1$, $^5D_0 \rightarrow {}^7F_2$, $^5D_0 \rightarrow {}^7F_3$ and $^5D_0 \rightarrow {}^7F_4$, respectively. The relative intensity between $^5D_0 \rightarrow {}^7F_2$ and $^5D_0 \rightarrow {}^7F_1$ is a measure of rare earth ion site symmetry. A lower symmetry of the crystal field around Sm^{2+} will result in a lower emission intensity of $^5D_0 \rightarrow {}^7F_1$ transition [124], what is clearly visible in *Figure 9.3b*. Theoretically, the line number of $^5D_0 \rightarrow {}^7F_J$ (J = 0, 1, 2, 3, 4) transitions of Sm^{2+} in site without central symmetry should be 1, 3, 5, 7, 9 [125]. Mismatch of experimentally obtained emission spectra could be explained with insufficient equipment resolution.

The excitation spectrum with several bands corresponding to the 4f–5d transitions, is shown in *Figure 9.3b*. The lowest peak of the excitation band corresponding to the absorption from $^7F_0$ ground state to the lowest level of the

$4f^5 5d^1$ states is situated at around 530 nm (18868 cm^{-1}). *Figure 9.3b* gives the excitation spectra in the range from 250 to 640 nm by monitoring the 691 nm emission. The spectrum consists of two broad bands peaking around at 530 and 335 nm (29850 cm^{-1}). These bands arise from the $4f^6$–$4f^5 5d^1$ transitions of Sm^{2+} ions. Broad band shape is due to the strong electron-phonon interaction. As the f–d transitions are susceptible to field effects, the higher energy 5d state of Sm^{2+} is split in to an orbital doublet e_g and a triplet t_{2g} state [116]. The band at 530 nm could be assigned as $^7F_0 \rightarrow 4f^5 5d^1(e_g)$ transitions to doublet state, due to narrower shape compared to higher energy band at 335 nm, e.g. $^7F_0 \rightarrow 4f^5 5d^1(t_{2g})$ to triplet state. Parity allowed f–d transition overspread spin-forbidden f–f lines; consequently, no distinctive peaks are visible in excitation spectrum. As it can be seen in *Figure 9.3b* traces of trivalent samarium still remain in S4A7 after annealing at 1300 °C for 4 h under H$_2$/N$_2$ atmosphere.

9.4. Temperature Dependent Luminescence

Figure 9.4 depicts the emission thermal quenching data of samarium-doped S4A7 sample prepared via combustion method with tris-amine as a fuel. To obtain single phase material after the first firing step 2.5 wt% of boric acid was added. Second [II] annealing step at 1300 °C for 8 h under H$_2$/N$_2$ reveal partial Sm^{3+} reduction to Sm^{2+}, even twice longer firing time was insufficient for reduction process. The Sm^{2+} emission is completely quenched in measured sample at 300 K, while, as expected [43], no substantial temperature influence is detected for Sm^{3+} emission. For more obvious representation of quenching process in *Figure 9.4b* emission integrals against temperature are plotted for mixed valence samarium; for Sm^{3+} integrated in range 500 – 680 nm and 680 – 900 nm for Sm^{2+}. In *Figure 9.4c* fitted data are given where rough estimation of TQ$_{1/2}$ for Sm^{3+} is more than twice higher if compared to Sm^{2+}, 666 K and 269 K, respectively. This confirms the theoretical viewpoint that pure f–f transitions are less susceptible for thermal effects than transitions where d-states are involved.
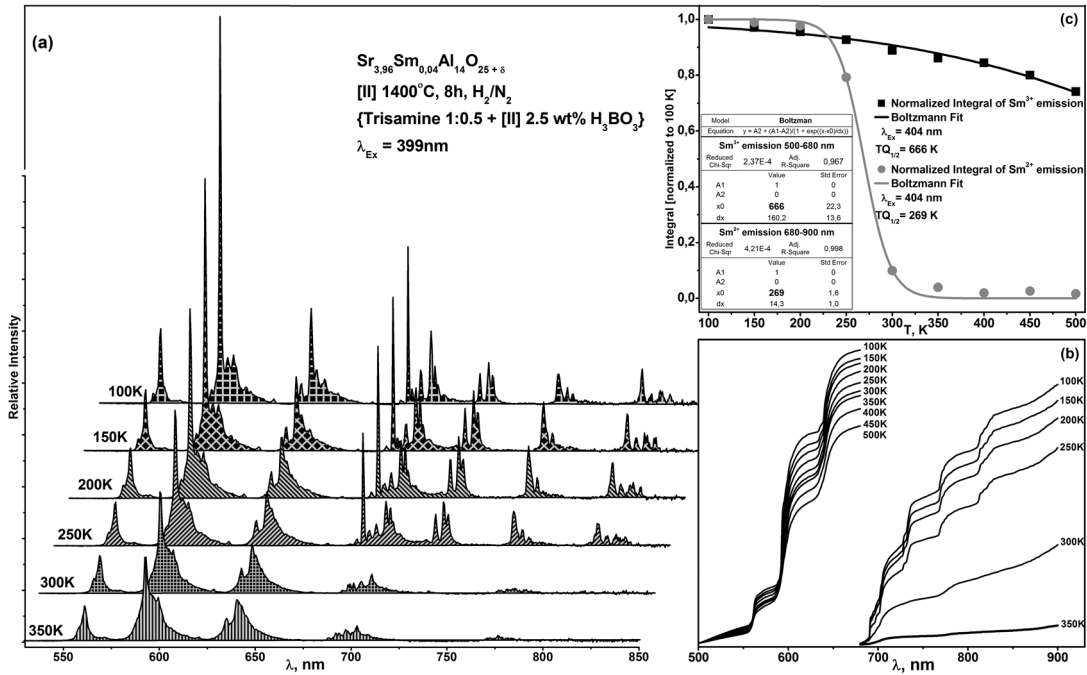
Figure 9.4 Temperature dependent emission data for mixed-valence samarium-doped S4A7 sample, prepared by combustion with trisamine: (a) emission under 399 nm excitation, (b) $Sm^{3+/2+}$ emission integrals, (c) emission $TQ_{1/2}$ value estimation for $Sm^{3+/2+}$.

In *Figure 9.5* the thermal quenching data is displayed for divalent samarium emission prepared via solid-state method. Differently than in previous case main emission is from Sm^{2+} and only traces of Sm^{3+} emission is detected. This circumstance leads to assumption that flux (H_3BO_3) has considerable effect on samarium reduction process. In *Figure 9.5c* fitted data are given for Sm^{2+} emission against the temperature. There is no significant difference between $TQ_{1/2}$ values of only divalent (275 K) and mixed-valence Sm-doped sample suggesting weak interaction between Sm^{2+} and Sm^{3+} ions. Also it is necessary to mention that no broad band emission is detected up to 500 K. Usually Sm^{2+}-doped materials exhibit band $4f^5 5d^1 \rightarrow {}^7F_J$ emission in the range of 600-800 nm due to thermal population of low lying $4f^5 5d^1$ [126]. Absence of broad emission indicates high enough energy gap between ${}^5D_0$ and the lowest $4f^5 5d^1$ levels leading to negligible thermally excited electron bridging. However in this scenario the emission lines from ${}^5D_1 \rightarrow {}^7F_J$ in the range 600 – 700 nm are expected [127]. But emission data given in *Figure 9.5a* does not show any visible lines at suggested wavelength indicating

efficient multiphonon relaxation from the higher $^5D_{1,2,3}$ to $^5D_0$ level regarding small energy difference between those states. $^5D_1 - {}^5D_0$ levels, with expected energy difference around 1300 cm^{-1}, could be bridged with two phonons with energies of about 650 cm^{-1}, typical for aluminates. Reflection spectra in *Figure 9.3* at room temperature indicate broad absorption band in the range of 500 to 750 nm probably from impurities or defects presence in the system. This band also aggravates detection of transitions from higher $^5D_J \rightarrow {}^7F_J$ levels, which usually have low intensity compared to main $^5D_0 \rightarrow {}^7F_0$ transition.
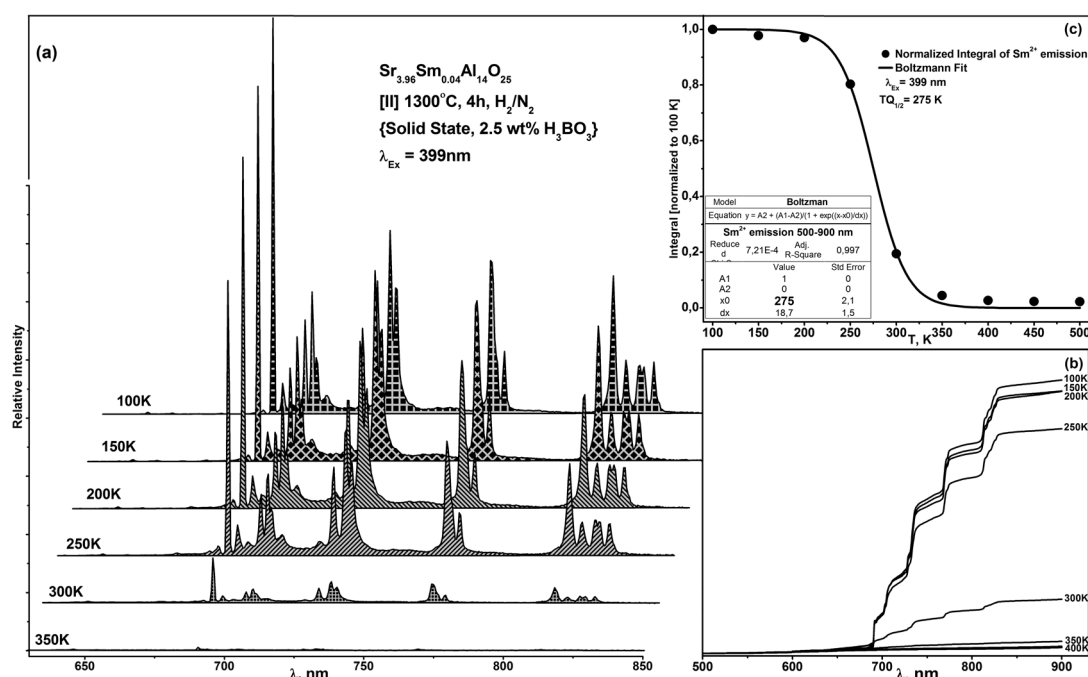
Figure 9.5 Temperature dependent emission data for divalent samarium-doped S4A7 sample, prepared by solid state with H_3BO_3 flux: (a) emission under 399 nm excitation, (b) Sm^{2+} emission integrals, (c) emission $TQ_{1/2}$ value estimation for Sm^{2+}.

9.5. Time Resolved Spectroscopy

Time dependent emission data against the temperature of S4A7:Sm samples are given in *Table 9.1*. All decay curves are bi-exponentially fitted and average lifetimes (⟨τ⟩) are calculated using formula given in table. Decay data correlate well with temperature dependent emission; for Sm^{3+} lifetime decrease gradually while for Sm^{2+} at quenching temperature τ value drops sharply. For Sm^{3+} measured average emission lifetimes falls in to the typical

2.5 – 2.8 ms range [128]. Decay for Sm^{2+} is approximately twice faster (1.4 – 1.5 ms) indicating different photoluminescence mechanism, as stated above.

Figure 9.6 Divalent and trivalent samarium emission decay values plotted against the temperature.

Deviation from single exponential decay might be caused by defects in the S4A7:Sm system what explains low relative percentage of τ_1 value. In *Figure 9.6* average decay values are plotted ($\langle\tau\rangle$) against the temperature. Slightly higher values for Sm^{2+} excited with shorter wavelength radiation present the time difference necessary for electron relaxation to lowest $^5D_0$ state from high lying $4f^55d^1$ band.

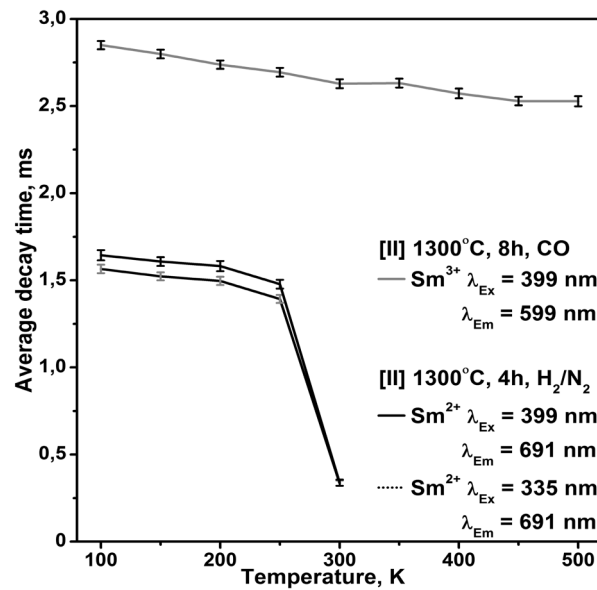*Table 9.1 Temperature dependent lifetime data for divalent and trivalent samarium emission in $Sr_4Al_{14}O_{25}$ host.*

Name	$\lambda_{(Ex)}$, nm	$\lambda_{(Em)}$, nm	T, K	τ_1, µs	σ	B_1	σ	Rel %	τ_2, µs	σ	B_2	σ	Rel %	χ^2	Durbin Watson	A	$\langle\tau\rangle$ µs
S4A7:Sm³⁺	**399**	**599**	**100**	**226**	8,6	238	6,3	6,3	**3027**	15,1	263	1,5	93,7	**1,174**	1,828	0,135	**2850**
[II] 1300°C, 8h, CO	-//-	-//-	150	240	9,2	227	5,9	6,6	2981	15,8	258	1,6	93,4	1,247	1,868	0,258	2799
Solid State, 2.5 wt% H₃BO₃	-//-	-//-	200	214	8,4	221	6,1	6,3	2908	15,7	241	1,5	93,7	1,161	1,793	0,365	2738
	-//-	-//-	250	245	9,4	219	5,8	7,1	2881	15,7	244	1,6	92,9	1,176	1,843	0,202	2694
	-//-	-//-	300	253	9,0	226	5,5	8,3	2844	16,4	221	1,6	91,7	1,225	1,796	0,223	2628
	-//-	-//-	350	216	8,1	211	5,7	7,7	2833	17,2	193	1,4	92,3	1,332	1,529	0,095	2632
	-//-	-//-	400	214	8,8	188	5,4	7,4	2761	19,1	182	1,4	92,6	1,200	1,827	0,077	2573
	-//-	-//-	450	182	7,7	198	6,1	6,7	2697	16,9	186	1,3	93,3	1,201	1,768	0,212	2529
	-//-	-//-	500	229	10,0	166	5,0	7,8	2721	18,9	167	1,4	92,3	1,152	1,849	0,166	2528
S4A7:Sm²⁺	**399**	**691**	**100**	**389**	13,6	366	7,3	13,2	**1744**	10,7	537	6,2	86,8	**1,185**	1,888	1,040	**1565**
[II] 1300°C, 4h, H₂/N₂	-//-	-//-	150	375	12,5	384	7,4	13,6	1704	10,3	535	6,1	86,4	1,168	1,878	1,201	1523
Solid State, 2.5 wt% H₃BO₃	-//-	-//-	200	397	12,5	397	7,3	15,7	1702	11,2	496	6,4	84,3	1,166	1,800	0,901	1497
	-//-	-//-	250	373	12,9	372	7,5	15,0	1573	10,2	499	6,5	85,0	1,175	1,886	0,904	1393
	-//-	-//-	300	154	4,3	718	13,2	47,1	497	10,6	250	13,3	52,9	1,122	1,820	1,789	335
Average lifetime	**335**	-//-	**100**	**428**	19,4	293	7,7	9,9	**1777**	9,7	644	7,1	90,1	**1,064**	1,947	-0,006	**1644**
	-//-	-//-	150	353	16,6	285	7,6	8,4	1723	8,6	637	5,9	91,6	1,100	1,961	0,059	1608
$\langle\tau\rangle = \dfrac{B_1\,\tau_1^2 + B_2\,\tau_2^2}{B_1\,\tau_1 + B_2\,\tau_2}$	-//-	-//-	200	418	19,2	294	7,9	10,3	1716	10,1	623	7,3	89,7	1,103	1,898	-0,015	1582
	-//-	-//-	250	360	16,7	294	7,7	9,6	1597	8,4	621	6,5	90,4	1,010	1,853	0,095	1478
	-//-	-//-	300	142	9,1	474	25,2	24,2	401	8,2	526	27,9	75,8	1,022	2,070	0,328	338

9.6. Review of Main Results

It was determined that the synthesis route has a crucial influence on the formation of $Sr_4Al_{14}O_{25}$ phase. The solid-state method with addition of H_3BO_3 flux leads to monophasic S4A7 compound at 1300 °C for 4 h. However, formation of phase pure $Sr_4Al_{14}O_{25}$ is aggravated during combustion process most likely due to fluxing additive loss. Divalent samarium-doped single phase $Sr_4Al_{14}O_{25}$ was synthesized via solid-state method, while combustion synthesis resulted only in partial reduction of doped lanthanide. The samarium emission spectra presented sharp and well resolved peaks; for Sm^{3+} $^4G_{5/2} \rightarrow {}^6H_J$ (J = 5/2, 7/2, 9/2 and 11/2) transitions were detected in the 550 – 725 nm range, for Sm^{2+} $^5D_0 \rightarrow {}^7F_{0-4}$ transitions were assigned in the 690 – 840 nm range. The spectral feature of Sm^{2+} emission spectrum indicated the low symmetry site occupation in S4A7. Excitation spectra in the range of 250 – 640 nm resulted in sharp $4f^5$-$4f^5$ transitions for Sm^{3+} and broad $^7F_0 \rightarrow 4f^55d^1$ absorption bands for Sm^{2+}. Difference of estimated emission thermal quenching ($TQ_{1/2}$) values was defined for both samarium oxidation states. Sm^{3+} loses half of its integrated emission intensity at around 650 K while for Sm^{2+} temperature influence is more pronounced ($TQ_{1/2} \approx 270$ K). Additionally temperature dependent emission lifetimes were determined: $\approx 2.5 – 2.8$ ms for Sm^{3+} and $\approx 1.45 – 1.65$ ms for Sm^{2+}. However, some of observed phenomena still require more detailed studies. The crystal-field splitting of Sm^{2+} emission rise some discrepancies, because there are fewer transitions detected as theory predicts. Besides, it is not clear broad emission band absence at higher temperature, which is typical for Sm^{2+} due to lower $4f^55d^1$ state thermal population.

Chapter 10. Conclusions

1. Samarium substituted $Sr_{1-x}Sm_xB_4O_7$ samples were prepared by solid-state synthesis route at 900 °C. The samarium reduction to divalent state was achieved under air at high temperature. The phase purity was confirmed by XRD measurements. To avoid the residual phases annealing should be repeated at least three times.

2. Minor Sm^{3+} emission were detected, despite the variation in annealing time and dopant concentration. Additionally, no influence of SmB_3O_6 side phase on Sm^{3+} emission intensity was observed.

3. The main single $^5D_0 \rightarrow {}^7F_0$ emission transition of Sm^{2+} was detected at 685.5 nm (14588 cm^{-1}) indicating single samarium crystallographic site occupation. Measured crystal field splitting of higher levels resulted in approximation of C_{2v} or lower symmetry site for Sm^{2+}. Estimated Stokes shift for Sm^{2+} d-f emission is ≈ 1600 cm^{-1} in SrB_4O_7. The vibronic transitions with energy difference about 98 cm^{-1} were found even at 100 K for the zero phonon line ($^5D_0 \rightarrow {}^7F_0$) of Sm^{2+}.

4. The temperature dependency of emission decay time of Sm^{2+} in SrB_4O_7 was evaluated. All the measured decay curves are fitted with single exponent. The observed saturation of decay time values for higher than 2.5 % samarium substitution indicate absence of Sm^{2+} concentration quenching, due to negligible interaction between optically active ions.

5. Orange-red emitting $La_{0.99}Sm_{0.01}MgB_5O_{10}$ and $Gd_{0.99}Sm_{0.01}MgB_5O_{10}$ photoluminescent materials were synthesized by a solid state reaction method at 1020 °C for 8 h. The phase purity was confirmed by XRD measurements.

6. Exclusively Sm^{3+} emission was detected containing four emission bands corresponding to the $^4G_{5/2} \rightarrow {}^6H_{5/2}$, $^6H_{7/2}$, $^6H_{9/2}$ and $^6H_{11/2}$ transitions peaking at 560, 600, 650 and 710 nm, respectively, upon excitation at $^6H_{5/2} \rightarrow {}^4L_{13/2} + {}^6P_{3/2} + {}^4F_{7/2}$ (402 nm) have been observed. Additionally, $^4F_{3/2} \rightarrow {}^6H_j$ transitions were also detected indicating that the $^4F_{3/2}$ level of Sm^{3+} is also populated to some extent.

7. By direct excitation of Gd^{3+} at 274 nm intense Sm^{3+} emission was measured indicating an efficient energy transfer from Gd^{3+} to Sm^{3+}. The luminescent kinetics data are fitted by single exponential curve giving experimental lifetime values in the range of 2.2 – 2.4 ms. The decay lifetimes for Sm^{3+} emission upon direct excitation of Gd^{3+} is around 0.1 ms longer, confirming the energy transfer phenomena.

8. It was determined that the synthesis conditions have a crucial influence on the formation of $SrAl_{12}O_{19}$ single phase. The combustion with EDTA resulted in single magnetoplumbite phase at 1500 °C, which was confirmed by the experimental data.

9. Even strong reducing conditions (H_2(20 %)/N_2(80 %)) and high temperature (1700 °C) produce trivalent samarium substituted magnetoplumbite structure ($SrAl_{12}O_{19}$:Sm^{3+} and $LaMgAl_{11}O_{19}$:Sm^{3+}) powder samples.

10. It was determined that H_3BO_3 flux greatly promotes the formation of $Sr_4Al_{14}O_{25}$ phase. The S4A7 compound is obtained at 1300 °C for 4 h with 2.5 wt% of flux in precursor mixture. The combustion synthesis route exhibited the main drawback due to loss of the flux during burning of initial gels. Divalent samarium-doped single phase $Sr_4Al_{14}O_{25}$ was synthesized via solid-state method under strong reducing atmosphere (H_2/N_2).

11. The samarium emission spectra presented sharp and well resolved peaks; for Sm^{3+} $^4G_{5/2} \rightarrow {}^6H_J$ (J = 5/2, 7/2, 9/2 and 11/2) transitions were detected in the 550 – 725 nm range, for Sm^{2+} $^5D_0 \rightarrow {}^7F_{0-4}$ transitions were assigned in the 690 – 840 nm range. The spectral feature of Sm^{2+} emission spectrum indicated the low symmetry site occupation in S4A7.

12. Difference of estimated emission thermal quenching ($TQ_{1/2}$) values was defined for both samarium oxidation states. Sm^{3+} loses half of its integrated emission intensity at around 650 K while for Sm^{2+} temperature influence is more pronounced ($TQ_{1/2} \approx 270$ K). Additionally temperature dependent emission lifetimes were determined: $\approx 2.5 – 2.8$ ms for Sm^{3+} and $\approx 1.45 – 1.65$ ms for Sm^{2+}.

Chapter 11. List of Publications and Conference Participation

11.1. List of Publications

1. S. Sakirzanovas, A. Katelnikovas, H. Bettentrup, A. Kareiva, T. Jüstel, "Synthesis and Photoluminescence Properties of Sm^{3+} doped $LaMgB_5O_{10}$ and $GdMgB_5O_{10}$", *Journal of Luminescence* **131** (2011) 1525–1529.

2. S. Sakirzanovas, A. Katelnikovas, D. Dutczak, A. Kareiva, T. Jüstel, "Synthesis and Sm^{2+}/Sm^{3+} doping effects on photoluminescence properties of $Sr_4Al_{14}O_{25}$", *Journal of Luminescence* **131** (2011) 2255–2262.

3. S. Sakirzanovas, A. Katelnikovas, D. Dutczak, A. Kareiva, T. Jüstel, "Concentration Influence on Temperature-dependent Luminescence Properties of Samarium Substituted Strontium Tetraborate", *Journal of Luminescence* (2011) accepted.

11.2. Patent

S. Sakirzanovas, T. Jüstel, H. Winkler, "SM-ACTIVATED ALUMINATE AND BORATE PHOSPHORS (Sm-aktivierte Aluminat- und Borat-Leuchtstoffe)", WO/2011/047757 A1 (DE 10 2009 050 542 A1), 2011

11.3. Published Contributions to Academic Conferences

1. S. Sakirzanovas, T. Jüstel. „Influence of Synthesis Conditions on Samarium Doped $Sr_4Al_{14}O_{25}$ Luminescence", ECSSC XII-XIIth European Conference on Solid State Chemistry, Muenster, Germany, September 20-23, 2009. p. 270

2. S. Sakirzanovas, H. Winkler, A. Kareiva, T. Jüstel. „Luminescence Properties of Divalent Samarium-Doped Strontium Tetraborate", 7th International Conference on f Elements, Cologne, Germany, August 23-27, 2009. p. P05-32-200

11.4. Publications Not Included in the Thesis

1. A. Katelnikovas, H. Bettentrup, D. Uhlich, S. Sakirzanovas, T. Juestel, A. Kareiva, Synthesis and optical properties of Ce3+-doped Y3Mg2AlSi2O12 phosphors, J. Lumin. 129 (11), 1356-1361, 2009.

2. S. Sakirzanovas, LD. Sun, CH. Yan, A. Kareiva, Sol-gel synthesis of nanosized Y3Sc2.5Ga2.5O12 garnet, Mendeleev Commun. 18 (5), 251-252, 2008.

3. A. Katelnikovas, T. Jüstel, D. Uhlich, J.-E. Jörgensen S. Sakirzanovas, A. Kareiva, Characterization of Cerium-Doped Yttrium Aluminium Garnet Nanopowders Synthesized via Sol-Gel Process, Chem. Eng. Comm. 195 (7), 758-769, 2008.

4. S. Sakirzanovas, A. Kareiva. Sol-gel Synthesis of Nanosized Lanthanide-doped Mixed-metal Garnets, Lith. J. Phys. 47 (1), 75-80, 2007.

5. E. Garskaite, S. Sakirzanovas, A. Kareiva, J. Glaser, H.J. Meyer. Synthesis and structure of europium aluminium garnet (EAG). Z. Anorg. Allg. Chem. 633 (7), 990-993, 2007.

6. A. Beganskienė S. Sakirzanovas, I. Kazadojev, A. Melnikaitis, V. Sirutkaitis, A. Kareiva, Sol-Gel Derived Antireflective Coatings with Controlled Thickness and Reflective Index, Materials Science-Poland, 25 (3), 817-824, 2007.

7. Beganskienė S. Šakirzanovas, A. Melnikaitis, V. Sirutkaitis, A. Kareiva. Sol-Gel Derived Optical Coating with Controlled Parameters. Medžiagotyra, SSN 1392-1320, 2006.

8. R. Skaudžius, A. Beganskiene, S. Sakirzanovas, D. Jasaitis, A. Kareiva, „Mixed metal garnets $Y_3Al_xM_{5-x}O_{12}$ (M-Ga, In): phase formation peculiarities". XLIV Meeting of the Serban Chemical Society, Belgrade, 6-7 February 2006.

Conferences Attended

1. S. Sakirzanovas. Sol-gel coatings with controlled parameters. 2nd Workshop on Laser-induced Damage, Hannover, Germany, July 4-5, 2007.

2. S. Sakirzanovas, T. Jüstel, A. Kareiva. Aqueous sol-gel synthesis and investigation of doped mixed-metal garnets. Advanced materials and technologies: 9th international summer school-conference, Palanga, Lithuania, 27-31 August 2007 p. 79

3. A. Beganskiene, S. Sakirzanovas, A. Melninkaitis, I. Kazadojev, V. Sirutkaitis, A. Kareiva. Sol-gel derived antireflective coating with controlled thickness and refractive index. 4th international conference on sol-gel materials, Kliczkow Castle, Poland, June 18-22, 2006 p. 51

4. S. Sakirzanovas, Ch. Yan, A. Kareiva. Sol-gel preparation and characterization of lanthanide-doped mixed-metal garnets. Advanced materials as studied by spectroscopic and diffraction techniques: specialized colloque AMPERE and Alexander von Humboldt workshop, Vilnius, Lithuania, September 16-21, 2006 p. P15

5. S. Sakirzanovas, L. Vilciauskas, A. Beganskiene, A. Kareiva. Chemically modified sol-gel derived nanosilica coatings for biotechnological applications. Fifth international conference on inorganic materials, Ljubljana, Slovenia, September 23-26, 2006 p. 173

6. R. Skaudzius, S Sakirzanovas, A. Katelnikovas, A. Beganskienė, A. Kareiva. Spectroscpic evaluation and characterization of different mixed-metal garnets. European seminar on infrared spectroscopy, Lyon, France, April 4-6, 2006 p. 57

7. R. Skaudzius, A. Beganskiene, S. Sakirzanovas, D.J. Jasaitis, A. Kareiva. Mixed metal garnets Y3AlxM5-xO12 (M-Ga, In): phase formation peculiarities. 44th meeting of the Serbian chemical society, Belgrade, February 6-7, 2006 ISBN 867132026X, p. 53

8. R. Skaudzius, S. Sakirzanovas. Sol-gel derived garnets: synthesis of YAG (Y3Al5O12) and YGG (Y3Ga5O12) at different temperatures.

Inorganic Materials: synthesis, properties and application: Vilnius University Conference for Young Scientists, Vilnius, December 16-17, 2006 p. 12

Chapter 12. REFERENCES

[1] B.J. Beaudry, J.K.A. Gschneidner, Chapter 2 Preparation and basic properties of the rare earth metals, in: Karl A. Gschneidner, Jr., E. LeRoy (Eds.) *Handbook on the Physics and Chemistry of Rare Earths*, Elsevier, 1978, pp. 173-232.

[2] B. Moine, G. Bizarri, *Mat. Sci. Eng. B-Solid*, **105** (2003) 2-7.

[3] C.M. MacRae, N.C. Wilson, *Microsc. Microanal.*, **14** (2008) 184-204.

[4] G. Blasse, B.C. Grabmaier, *Luminescent materials*, Springer-Verlag, Berlin ; New York, 1994.

[5] S. Nakamura, T. Mukai, M. Senoh, *Appl Phys Lett*, **64** (1994) 1687-1689.

[6] R.M. Macfarlane, R.M. Shelby, *Opt. Lett.*, **9** (1984) 533-535.

[7] A. Winnacker, R.M. Shelby, R.M. Macfarlane, *Opt. Lett.*, **10** (1985) 350-352.

[8] R. Jaaniso, H. Bill, *Europhys Lett*, **16** (1991) 569-574.

[9] W. Chen, M.Z. Su, *J. Phys. Chem. Solids*, **60** (1999) 371-378.

[10] T. Hayakawa, M. Nogami, *IPAP Books 2*, (2005) 193-198.

[11] M. Nogami, K. Suzuki, *Adv. Mater.*, **14** (2002) 923-926.

[12] H.W. Song, M. Nogami, *J. Non-Cryst. Solids*, **297** (2002) 113-119.

[13] J.H. Zhang, S.H. Huang, J.Q. Yu, *J. Lumin.*, **56** (1993) 51-55.

[14] J.H. Zhang, H.W. Song, Y. Zhao, M.Z. Tian, K. Dou, S.H. Huang, J.Q. Yu, *J. Lumin.*, **64** (1995) 207-211.

[15] G.H. Dieke, H.M. Crosswhite, H. Crosswhite, *Spectra and energy levels of rare earth ions in crystals*, Interscience Publishers, New York,, 1968.

[16] L.R. Morss, *Chemical Reviews*, **76** (1976) 827-841.

[17] B.M. Nikolai, et al., *Russian Chemical Reviews*, **61** (1992) 990.

[18] C. Görller-Walrand, K. Binnemans, Chapter 155 Rationalization of crystal-field parametrization, in: Karl A. Gschneidner, Jr., E. LeRoy (Eds.) *Handbook on the Physics and Chemistry of Rare Earths*, Elsevier, 1996, pp. 121-283.

[19] P. Dorenbos, *J. Alloys Compd.*, **341** (2002) 156-159.

[20] A. Lupei, V. Lupei, C. Gheoghe, L. Gheorghe, G. Aka, D. Vivien, *Opt. Mater.*, **30** (2008) 1677-1681.

[21] S. Cotton, *Lanthanide and actinide chemistry*, Wiley, Chichester, England ; Hoboken, NJ, 2006.

[22] B. Valeur, J.-C. Brochon, *New trends in fluorescence spectroscopy : applications to chemical and life science*, Springer, New York, 2001.

[23] B.M. van der Ende, L. Aarts, A. Meijerink, *Phys Chem Chem Phys*, **11** (2009) 11081-11095.

[24] J.R. Lakowicz, *Principles of fluorescence spectroscopy*, 2nd ed., Kluwer Academic/Plenum, New York, 1999.

[25] G.H. Dieke, H.M. Crosswhite, *Applied Optics*, **2** (1963) 675-686.

[26] N. Sabbatini, M. Guardigli, J.M. Lehn, *Coordin Chem Rev*, **123** (1993) 201-228.

[27] W.T. Carnall, Chapter 24 The absorption and fluorescence spectra of rare earth ions in solution, in: Karl A. Gschneidner, Jr., E. LeRoy (Eds.) *Handbook on the Physics and Chemistry of Rare Earths*, Elsevier, 1979, pp. 171-208.

[28] B.M. Walsh, *Nato Sci Ser Ii Math*, **231** (2006) 403-433.

[29] Phosphor Research Society., *Phosphor handbook*, CRC Press, Boca Raton, FL, 1999.

[30] J.C.G. Bünzli, G.R. Choppin, *Lanthanide probes in life, chemical, and earth sciences : theory and practice*, Elsevier, Amsterdam ; New York, 1989.

[31] J. Holsa, M. Lastusaari, M. Marysko, M. Tukia, *J Solid State Chem*, **178** (2005) 435-440.

[32] R.M. Macfarlane, R.M. Shelby, A. Winnacker, *Phys. Rev. B*, **33** (1986) 4207.

[33] R. Macfarlane, M., R. Shelby, M., A. Winnacker, *Journal de Physique*, **46** (1985) C7-537-C537-542.

[34] B.R. Judd, *Phys. Rev.*, **127** (1962) 750.

[35] G.S. Ofelt, *J. Chem. Phys.*, **37** (1962) 511-520.

[36] G.S. Ofelt, *J. Chem. Phys.*, **38** (1963) 2171-2180.

[37] R. Jaaniso, H. Bill, *Phys. Rev. B*, **44** (1991) 2389-2392.

[38] P. Mikhail, J. Hulliger, K. Ramseyer, *Solid State Commun.*, **112** (1999) 483-488.

[39] B. Henderson, G.F. Imbusch, *Optical spectroscopy of inorganic solids*, Clarendon Press ; Oxford University Press, Oxford Oxfordshire New York, 1989.

[40] C. Görller-Walrand, K. Binnemans, Chapter 167 Spectral intensities of f-f transitions, in: Karl A. Gschneidner, Jr., E. LeRoy (Eds.) *Handbook on the Physics and Chemistry of Rare Earths*, Elsevier, 1998, pp. 101-264.

[41] C.K. Jørgensen, B.R. Judd, *Molecular Physics*, **8** (1964) 281-290.

[42] M. Gaft, R. Reisfeld, G. Panczer, *Modern luminescence spectroscopy of minerals and materials*, Springer, Berlin ; New York, 2005.

[43] M.D. Chambers, D.R. Clarke, *Annu. Rev. Mater. Res.*, **39** (2009) 325-359.

[44] J.M.F. van Dijk, M.F.H. Schuurmans, *The Journal of Chemical Physics*, **78** (1983) 5317-5323.

[45] A. Gilbert, J.E. Baggott, *Essentials of molecular photochemistry*, Blackwell Scientific Publications, Oxford ; Boston, 1991.

[46] G. Stein, E. Wurzberg, *The Journal of Chemical Physics*, **62** (1975) 208-213.

[47] C.K. Jayasankar, V. Venkatramu, P. Babu, T. Troster, W. Sievers, G. Wortmann, W.B. Holzapfel, *J. Appl. Phys.*, **97** (2005) -.

[48] T. Suhasini, J.S. Kumar, T. Sasikala, K.W. Jang, H.S. Lee, M. Jayasimhadri, J.H. Jeong, S.S. Yi, L.R. Moorthy, *Opt. Mater.*, **31** (2009) 1167-1172.

[49] E. Cavalli, A. Belletti, R. Mahiou, P. Boutinaud, *J. Lumin.*, **130** (2010) 733-736.

[50] G. Dominiak-Dzik, *J. Alloys Compd.*, **391** (2005) 26-32.

[51] J.B. Gruber, B. Zandi, M.F. Reid, *Phys. Rev. B*, **60** (1999) 15643-15653.

[52] J.B. Gruber, B. Zandi, M. Ferry, L.D. Merkle, *J. Appl. Phys.*, **86** (1999) 4377-4382.

[53] B.C. Jamalaiah, J.S. Kumar, A.M. Babu, T. Suhasini, L.R. Moorthy, *J. Lumin.*, **129** (2009) 363-369.

[54] G. Grenet, M. Kibler, A. Gros, J.C. Souillat, J.C. Gâcon, *Phys. Rev. B*, **22** (1980) 5052.

[55] M. Karbowiak, A. Urbanowicz, M.F. Reid, *Phys. Rev. B*, **76** (2007) -.

[56] D. Nishida, E. Yamade, M. Kusaba, T. Yatsuhashi, N. Nakashima, *J. Phys. Chem. A*, **114** (2010) 5648-5654.

[57] J. Qiu, K. Hirao, *J. Mater. Sci. Lett.*, **20** (2001) 691-693.

[58] E. Malchukova, B. Boizot, G. Petite, D. Ghaleb, *J. Non-Cryst. Solids*, **353** (2007) 2397-2402.

[59] Z. Liu, T. Massil, H. Riesen, *Physics Procedia*, **3** (2010) 1539-1545.

[60] T. Penhouet, H. Hagemann, *J. Alloys Compd.*, **451** (2008) 74-76.

[61] Y.R. Shen, K.L. Bray, *Phys. Rev. B*, **58** (1998) 11944-11958.

[62] A. Meijerink, G.J. Dirksen, *J. Lumin.*, **63** (1995) 189-201.

[63] Y.R. Shen, W.B. Holzapfel, *Phys. Rev. B*, **52** (1995) 12618-12626.

[64] Y. Huang, W. Kai, Y. Cao, K. Jang, H.S. Lee, I. Kim, E. Cho, *J. Appl. Phys.*, **103** (2008) 053501-053507.

[65] Y.L. Huang, W.X. Zhao, L. Shi, H.J. Seo, *J. Alloys Compd.*, **477** (2009) 936-940.

[66] P. Mikhail, A. Sieber, T. Samtleben, B. Trusch, T. Luthi, J. Hulliger, *J Solid State Chem*, **154** (2000) 535-541.

[67] H.B. Liang, Q.H. Zeng, T.D. Hu, S.B. Wang, Q. Su, *Solid State Sci.*, **5** (2003) 465-467.

[68] Q.H. Zeng, Z.W. Pei, Q. Su, S.Z. Lu, *J. Lumin.*, **82** (1999) 241-249.

[69] P. Mikhail, J. Hulliger, *Comments Inorg. Chem.*, **21** (1999) 263-283.

[70] M.Y. Peng, Z.W. Pei, G.Y. Hong, Q. Su, *Chem. Phys. Lett.*, **371** (2003) 1-6.

[71] E.J. Nassar, L.A. Rocha, E.F. Molina, K.J. Ciuffi, P.S. Calefi, *Mater Chem Phys*, **101** (2007) 238-241.

[72] W. Szuszkiewicz, B. Keller, M. Guzik, T. Aitasalo, J. Niittykoski, J. Holsa, J. Legendziewicz, *J Alloy Compd*, **341** (2002) 297-306.

[73] R.E. Bradbury, E.Y. Wong, *Phys. Rev. B*, **4** (1971) 702.

[74] G.R. Choppin, Z.M. Wang, *Inorg Chem*, **36** (1997) 249-252.

[75] S.T. Frey, W.D. Horrocks, *Inorg Chim Acta*, **229** (1995) 383-390.

[76] M.C. Montoya, D. Megias, R. Marrero, B.M. Del Peso, M.A. Garcia, J.J. Bravo-Cordero, A. Garcia-Grande, A. Santos, *Microsc Res Techniq*, **72** (2009) 1-11.

[77] R. Nudelman, B.V. Bronk, S. Efrima, *Appl Spectrosc*, **54** (2000) 445-449.

[78] A. Perloff, S. Block, *Acta Crystallogr.*, **20** (1966) 274-279.

[79] J.W.M. Verwey, G.J. Dirksen, G. Blasse, *J. Phys. Chem. Solids*, **53** (1992) 367-375.

[80] Z.W. Pei, Q. Su, J.Y. Zhang, *J. Alloys Compd.*, **198** (1993) 51-53.

[81] K. Machida, G. Adachi, J. Shiokawa, *J. Lumin.*, **21** (1979) 101-110.

[82] G. Heller, A survey of structural types of borates and polyborates, in: *Structural Chemistry of Boron and Silicon*, Springer Berlin / Heidelberg, 1986, pp. 39-98.

[83] D.A. Keszler, *Current Opinion in Solid State and Materials Science*, **4** (1999) 155-162.

[84] J.B. Kim, K.S. Lee, I.H. Suh, J.H. Lee, J.R. Park, Y.H. Shin, *Acta Crystallogr C*, **52** (1996) 498-500.

[85] N.L. Ross, R.J. Angel, *J Solid State Chem*, **90** (1991) 27-30.

[86] Q.S. Lin, W.D. Cheng, J.T. Chen, J.S. Huang, *J Solid State Chem*, **144** (1999) 30-34.

[87] Z.F. Wei, X.L. Chen, F.M. Wang, W.C. Li, M. He, Y. Zhang, *J Alloy Compd*, **327** (2001) L10-L13.

[88] Q.H. Zeng, Z.W. Pei, S.B. Wang, Q. Su, *Spectrosc. Lett.*, **32** (1999) 895-912.

[89] X.A. Chen, Z.H. Tang, M. Li, *Solid State Sci*, **10** (2008) 894-900.

[90] A. Lapshin, E. Litovchik, I. Polyakova, Y. Shepelev, *Russian Journal of Inorganic Chemistry*, **52** (2007) 839-843.

[91] C.F. Chenot, *Journal of the American Ceramic Society*, **50** (1967) 117-118.

[92] R. Komatsu, H. Kawano, Z. Oumaru, K. Shinoda, V. Petrov, *J. Cryst. Growth*, **275** (2005) e843-e847.

[93] Q.H. Zeng, Z.W. Pei, S.B. Wang, Q.A. Su, S.Z. Lu, *J. Mater. Sci. Technol.*, **15** (1999) 449-452.

[94] B. Saubat, M. Vlasse, C. Fouassier, *J Solid State Chem*, **34** (1980) 271-277.

[95] J.M. Fan, Z.B. Lin, L.Z. Zhang, G.F. Wang, *Chinese Journal of Structural Chemistry*, **25** (2006) 709-713.

[96] J. Hölsä, M. Leskelä, *Molecular Physics: An International Journal at the Interface Between Chemistry and Physics*, **54** (1985) 657 - 667.

[97] D.W. Goodwin, A.J. Lindop, *Acta Crystallographica Section B*, **26** (1970) 1230-1235.

[98] A.J. Lindop, D.W. Goodwin, *Acta Crystallographica Section B*, **28** (1972) 2625-2626.

[99] R.X. Fischer, H. Schneider, M. Schmucker, *Am Mineral*, **79** (1994) 983-990.

[100] T.N. Nadezhina, E.A. Pobedimskaya, N.V. Belov, *Kristallografiya*, **25** (1980) 938-943.

[101] Q. Li, J.W. Zhao, F.L. Sun, *J. Rare Earths*, **28** (2010) 26-29.

[102] F. Massazza, *Chim. Ind. (Milan)*, **41** (1959) 108-115.

[103] E.M. Levin, C.R. Robbins, H.F. McMurdie, Phase diagrams for ceramists, in: United States. National Bureau of Standards., American Ceramic Society., Institute for Materials Science and Engineering (U.S.). Ceramics Division., Materials Science and Engineering Laboratory (U.S.). Ceramics Division. (Eds.), American Ceramic Society, Columbus, OH, 1964, pp. v.

[104] M.Q. Wang, W. Dong, G.L. Lu, *Mat. Sci. Eng. B-Solid*, **57** (1998) 18-23.

[105] D. Wang, M.Q. Wang, G.L. Lu, *J. Mater. Sci.*, **34** (1999) 4959-4964.

[106] T.N. Nadezhina, E.A. Pobedimskaya, N.V. Belov, *Kristallografiya*, **21** (1976) 826-828.

[107] M. Capron, F. Fayon, D. Massiot, A. Douy, *Chem. Mater.*, **15** (2003) 575-579.

[108] A. Douy, M. Capron, *J. Eur. Ceram. Soc.*, **23** (2003) 2075-2081.

[109] A. Nag, T.R.N. Kutty, *J. Alloys Compd.*, **354** (2003) 221-231.

[110] R. Shannon, *Acta Crystallographica Section A*, **32** (1976) 751-767.

[111] R. Collongues, D. Gourier, A. Kahnharari, A.M. Lejus, J. Thery, D. Vivien, *Annu. Rev. Mater. Sci.*, **20** (1990) 51-82.

[112] J.-G. Park, A.N. Cormack, *Korean Journal of Crystallography*, **11** (2000) 176-181.

[113] C.R. Ronda, *Luminescence : from theory to applications*, Wiley-VCH, Weinheim, 2008.

[114] Q.H. Zeng, Z.W. Pei, Q. Su, S.H. Huang, *Phys. Status Solidi B*, **212** (1999) 207-219.

[115] D.L. Wood, W. Kaiser, *Phys. Rev.*, **126** (1962) 2079.

[116] P. Dorenbos, *J. Phys. Condens. Matter*, **15** (2003) 575-594.

[117] X.Y. Chen, M.P. Jensen, G.K. Liu, *J. Phys. Chem. B*, **109** (2005) 13991-13999.

[118] C.A. Kodaira, R. Stefani, A.S. Maia, M.C.F.C. Felinto, H.F. Brito, *J. Lumin.*, **127** (2007) 616-622.

[119] A.K. Singh, S.K. Singh, R. Prakash, S.B. Rai, *Chem. Phys. Lett.*, **485** (2010) 309-314.

[120] E.J. Bosze, G.A. Hirata, L.E. Shea-Rohwer, J. McKittrick, *J. Lumin.*, **104** (2003) 47-54.

[121] R. Praveena, V. Venkatramu, P. Babu, C.K. Jayasankar, *Physica B-Condensed Matter*, **403** (2008) 3527-3534.

[122] Z.C. Wu, M.L. Gong, J.X. Shi, Q. Su, *J. Alloys Compd.*, **458** (2008) 134-137.

[123] T. Nakamura, K. Kaiya, N. Takahashi, T. Matsuzawa, C.C. Rowlands, V. Beltran-Lopez, G.M. Smith, P.C. Riedi, *J. Mater. Chem.*, **10** (2000) 2566-2569.

[124] J.Y. Wang, Y.D. Li, Y.L. Huang, L. Shi, H.J. Seo, *Mater. Chem. Phys.*, **120** (2010) 598-602.

[125] K. Fujita, K. Tanaka, K. Hirao, N. Soga, *J. Appl. Phys.*, **81** (1997) 924-930.

[126] C. Wickleder, *J. Lumin.*, **94** (2001) 127-132.

[127] A. Edgar, C.R. Varoy, C. Koughia, D. Tonchev, G. Belev, G. Okada, S.O. Kasap, H. von Seggern, M. Ryan, *Opt. Mater.*, **31** (2009) 1459-1466.

[128] A. Herrmann, D. Ehrt, *J. Non-Cryst. Solids*, **354** (2008) 916-926.